Fall 2022

Cyclic Response and Liquidfaction Behavior of Gravelly Soils

Pitak Ruttithivaphanich

CYCLIC RESPONSE AND LIQUIDFACTION BEHAVIOR OF GRAVELLY SOILS

by

Pitak Ruttithivaphanich

Bachelor of Engineering
Kasetsart University, 2013

Master of Engineering
Asian Institute of Technology, 2015

Submitted in Partial Fulfillment of the Requirements

For the Degree of Doctor of Philosophy in

Civil Engineering

College of Engineering and Computing

University of South Carolina

2022

Accepted by:

Inthuorn Sasanakul, Major Professor

Sarah Gassman, Committee Member

Charles Pierce, Committee Member

Scott White, Committee Member

Cheryl L. Addy, Interim Vice Provost and Dean of the Graduate School

ACKNOWLEDGEMENTS

I would like to express my sincere appreciation to Dr. Inthuorn Sasanakul for all of her support and supervision throughout my Ph.D. program. Her support to my research development and to this investigation has been invaluable.

I would also like to express my gratitude to Dr. Sarah Gassman, Dr. Charles Pierce, and Dr. Scott White for their efforts as committee members. I am extremely appreciative for suggestions and comments that will help me enhance this research.

Throughout my PhD studies, Siwadol Dejphumee, Kazi Islam, Trevor Curran, Beau Studley, Pressley Perry, Valerie Sims, and Landon Kelley provided invaluable assistance. Similarly, I would like to appreciate the contributions of Dr. Juan Caicedo, Dr. Qian Yu, Russel Inglett, Brian Hull, Rachel Dotter, Karen Ammarell, Sherry Bailey, and Carol Stork in various technical aspects.

I would also like to appreciate the unconditional support during my time of great need by my family, my girlfriend, and all the Thai students in Columbia. My Ph.D. journey cannot be achieved without the support and love of those around me. I will forever be grateful.

ABSTRACT

Cyclic response and liquefaction behavior are soil mechanisms under earthquake conditions. The study of dynamic soil response is important to evaluate soil behaviors under dynamic loading for a wide range of strains. Soil liquefaction phenomena involving a significant reduction in the strength and stiffness of saturated cohesionless soils has caused catastrophic ground failure in numerous earthquakes. Liquefaction mostly occurs in sand, but liquefaction of gravelly soil has been observed. To date, only a few studies have focused on the liquefaction of gravelly soils; hence, research data is limited. This research aims to improve the understanding of cyclic response and liquefaction behavior of gravelly soils through experimental methods including cyclic triaxial tests and dynamic centrifuge modeling tests.

In undrained cyclic triaxial (CTX) tests, the cyclic response of mine waste rock; which consists of gravel, sand, and fines; was evaluated. A total of forty-two CTX tests were performed on undisturbed and reconstituted waste rock samples that have comparable grain size distribution and normalized shear wave velocity ($V_{s,1}$) ranging from 260 to 400 m/s. Shear modulus and damping curves were also evaluated to characterize dynamic soil properties. Results from the CTX tests were analyzed for the number of cycles required to cause liquefaction (N_L) at a given cyclic stress ratio (CSR) and for the behavior of pore water pressure development leading to soil liquefaction. It was found that as CSR increases,

the N_L decreases. The relationships between the CSR and N_L were found to be relatively close to sand, and the effect of the effective confining stress on the CSR was also observed in the gravelly soil samples. For these gravelly soils, the ultimate friction angle, the phase transform friction angle, and the post-cyclic friction angle were found to be 51.5, 41.6, and 32.5 degrees, respectively. During preliminary evaluation of the shear wave velocity (V_s) of these gravelly soils, it was also found that the V_s-based liquefaction assessment developed in previous studies for sand does not apply to the materials tested in this study because the V_s of these gravelly soils are significantly higher than the V_s of sand. One of the factors contributing to the liquefaction behavior is the type of matrix soil structure that consists of gravel, sand, and fines. Different types of matrix soil structures, including Interlocked Gravel Matrix, Gravel-Sand Matrix, and Gravel-Fines Matrix, can be assessed based on the basic understanding of phase relationships. It was found that the highest potential of liquefaction is when the soil has Gravel-Sand Matrix, as gravel particles are not in contact and interlocked with each other.

The liquefaction behavior of four loose mining waste rock mixtures with variable amounts of gravel, sand, and fines has been investigated in eight geotechnical centrifuge modeling tests. Mixtures of these soils are 40-48-12, 50-38-12, 50-50-00, and 70-30-00 for gravel-sand-fines content. The $V_{s,1}$ of these materials is approximately 127, 128, 125, and 117 m/s, respectively. The relative densities, void ratios, and shear wave velocities of these samples are also comparable, but the samples containing fines had an order of magnitude lower permeability. During the shaking events, acceleration time histories and pore water pressure ratios were obtained and used to establish shear stress-strain behaviors. To evaluate the effect of soil composition, a 0.27-g sinusoidal base shaking amplitude was

applied to four centrifuge models. It was observed that soil liquefaction occurred in all models except for a model comprised of 70% gravel and 30% sand. The acceleration time histories of all models exhibited dilative behavior, which was dependent on the development of excess pore pressure and effective stress. In models without fines, pore pressure dissipation was observed during shaking. After the tests, models with fines exhibited more settlement and volumetric strain. According to the findings, an increase in the amount of sand and fines increases the liquefaction potential of mine waste rock. The impacts of fines content on the liquefaction behavior and dynamic response of gravelly soils were also evaluated. Six models of two loose saturated gravelly soil samples were investigated in the centrifuge. The first gravelly soil mixture consisted of 50% gravel, 38% sand, and 12% fines, whereas the second soil mixture consisted of 50% gravel and 50% sand. Each soil mixture was subjected to uniform sinusoidal shaking with amplitudes of 0.19 g, 0.27 g, and 0.40 g. Based on the results, the fines content had a relatively low impact on cyclic shear strain, the rate of pore pressure development during shaking, the cyclic resistance ratio, and the reduction of shear modulus. However, the fines content has a noticeable impact on soil dilatancy, the rate of pore pressure dissipation during and after shaking, damping, volumetric strains, and soil fabric after shaking.

TABLE OF CONTENTS

LIST OF TABLES

LIST OF FIGURES

LIST OF SYMBOLS

A_L, A_{loop}, or W	Area inside the hysteretic loop to calculate hysteretic damping
A_m	Membrane surface area
a_{model}	Acceleration in model scale
$a_{prototype}$	Acceleration in prototype scale
A_r	Maximum amplitude
A_T or $W_{elastic}$	Peak strain energy stored during the cycle to calculate hysteretic damping
C	Cohesion
C'	Effective cohesion
C_c	Curvature coefficient
C_r	Correction factor for estimated CRR for DSS test
C_{RM}	Membrane compliance ratio
C_u	Uniformity coefficient
C_v	Coefficient of consolidation
d	Distance in effect of consolidation time
d	Particle size diameter
D	Damping
D	Specimen diameter to represent the dimensions of specimen
D_{50}	Mean grain diameter

D_{min} Minimum damping

D_{min1} Minimum damping at mean effective normal stress of 100 kPa

Dr Relative density

e Void ratio

E Young's modulus

E_h Horizontal Young's modulus

e_{max} Maximum void ratio

e_{min} Minimum void ratio

E_v Vertical Young's modulus

f Frequency

$F(e)$ Function accounting for the void ratio

f_m Flexibility of membrane

f_n Fundamental frequency

f_r Resonant frequency

G or G_{sec} Shear modulus or secant shear modulus

g Gravity acceleration

G/G_{max} Normalized shear modulus

G_{aniso} or G_{hv} Shear modulus in anisotropy condition

G_{hv} Shear modulus in a vertical plane

G_{iso} Shear modulus in isotropy condition

G_{max} Low-strain maximum shear modulus

G_s Specific gravity

$G_{s,f}$ Specific gravity of pure fine

$G_{s,g}$ Specific gravity of pure gravel

$G_{s,s}$ Specific gravity of pure sand

G_{st} Gross specific gravity

H Specimen height to represent the dimensions of specimen

I_G Coefficient of increasing shear modulus

k Correction exponent to calculate γ_{r1} and D_{min1} in dynamic soil models

k Soil permeability in centrifuge modeling test

k_0 Coefficient of lateral earth pressure

K_{20} Soil permeability at 20 degrees Celsius

K_s Intrinsic permeability

K_s Bulk modulus of the soil for calculate effect of membrane compliance

m_v Compressibility of soil

n Exponential parameter of the effective mean stress

N Gravitational acceleration or centrifugal acceleration

N Number of cycles

N_L Number of cycles to cause liquefaction

p' Mean effective stress

p'/p'_c Normalized mean effective stress

P_a or P_{at} Referent stress at 100 kPa or atmospheric pressure

q or τ Shear stress

R^2 Coefficient of determination

r_u Excess pore pressure ratio

$r_{u,max}$ Maximum excess pore pressure ratio

S	Degree of saturation
t	Dynamic time
T_v	Diffusion time
$\ddot{u}$ or a	Acceleration
$\dot{u}$ or v	Velocity
u	Displacement in the equation to define acceleration
U_L	Pore pressure at initial liquefaction
u_e or ΔU	Excess pore water pressure
V_s	Shear wave velocity
$V_{s,1}$	Normalized shear wave velocity
$V_{s,f}$	Volume of pure fine
$V_{s,g}$	Volume of pure gravel
$V_{s,s}$	Volume of pure sand
$V_{s,t}$	Total volume of solid
$V_{v,gs}$	Volume of void created by gravel skeleton
$V_{v,ss}$	Volume of void created by sand skeleton
$W_{s,f}$	Mass of pure fines
$W_{s,g}$	Mass of pure gravel
$W_{s,s}$	Mass of pure sand
$W_{s,t}$	Total solid mass of a soil mixture
α	Horizontal static shear stress
γ_d	Dry unit weight
$\gamma_{d,g}$	Dry unit weight of gravel

$\gamma_{d,max}$ Maximum dry density

$\gamma_{d,min}$ Minimum dry density

$\gamma_{d,s}$ Dry unit weight of sand

γ_w Unit weight of water

γ Shear strain

γ_r Reference threshold strain

γ_{sa} Single amplitude strain

ΔB_m Unit membrane compliance

$\Delta u_{compliance}$ Excess pore water pressure during the cyclic test in a compliant system.

Δu_L Excess pore water pressure at initial liquefaction

$\Delta u_{non\text{-}compliance}$ Exceed pore water pressure without the effect of membrane compliance

ΔV Volume change

ΔV_m Membrane penetration

ΔV_S True soil skeletal volume change

ΔV_T Total soil skeletal volume change

$\Delta\sigma$ Deviator stress

$\Delta\sigma/\sigma'_c$ Normalized deviator stress

$\Delta\varepsilon_{v,s}$ Skeletal volumetric strain

$\Delta\varepsilon_a$ Differential axial strain

ε or ε_a Axial strain

ε_r Radial strain

μ Viscosity of fluid in centrifuge modeling test

μ Poisson's ratio

μ_{hh}	Poisson's ratio in a horizontal plane
μ_{vh}	Poisson's ratio in a vertical plane
ρ	Density of soil
ρ_f	Density of pore fluid
σ	Total stress
σ_v	Total vertical stress
σ'_c	Effective confining stress
σ'_m	Mean effective normal stress
σ'_v	Effective vertical stress
τ	Shear stress
ω or W_n	Water content or natural water content
ω_f	Final water content
ω_i	Initial water content
ϕ	Friction angle
ϕ'	Effective Friction angle
ϕ'_{pt}	Phase transform effective Friction angle
ϕ'_{ult}	Ultimate effective friction angle

LIST OF ABBREVIATIONS

ACC ..... Accelerometer

ASTM ..... American Society for Testing and Materials

CH ..... High Plasticity Clay

CIDTX or CDTX ..... Isotropic Consolidated Drained Triaxial

CIUTX or CUTX ..... Isotropic Consolidated Undrained Triaxial

CL ..... Low Plasticity Clay

CO_2 ..... Carbon Dioxide

CRR ..... Cyclic Resistance Ratio

$CRR_{M=7.5}$ ..... Cyclic Resistance Ratio at an Earthquake Magnitude of 7.5

CSR ..... Cyclic Stress Ratio

CTX ..... Cyclic Triaxial

DA ..... Double Amplitude

DSS ..... Direct Simple Shear

EOP ..... End of Primary (Consolidation)

ES ..... Effective Stress

EVS ..... Effective Vertical Stress

FFT ..... Fast Fourier Transform

GC ..... Clayey gravel

GM ..... Silty gravel

GP ..... Poorly Graded Gravel

GW ..... Well Graded Gravel

HPMC ..... Hydroxypropyl Methylcellulose

LEAP ..... Liquefaction Experiments and Analysis Project

LL ..... Liquid Limit

LVDT ..... Linear Variable Differential Transformer

MH ..... High Plasticity Silt

ML ..... Low Plasticity Silt

MLIT ..... Ministry of Land, Infrastructure, Transport and Tourism

NC ..... Normal-Consolidation

NI-DAQ ..... National Instrument Data Acquisition

PI ..... Plasticity Index

PL ..... Plastic Limit

PT ..... Phase Transform

PWP ..... Pore Water Pressure

RC ..... Resonant Column

RC/TS ..... Resonant Column and Torsional Shear

RO ..... Research Objective

RPI ..... Rensselaer Polytechnic Institute

RQ ..... Research Question

SA ..... Single Amplitude

SC ..... South Carolina

SC ..... Clayey sand

SM ..... Silty sand

SP ..... Poorly Graded Sand

SPT ..... Standard Penetration Test

SW..... Well Graded Sand

TS..... Torsional Shear

UC-Davis .....University of California, Davis

ULT or UT .....Ultimate

USCS..... Unified Soil Classification System

1-D ..... One Dimension

CHAPTER 1

INTRODUCTION

1.1 Research Motivation

In the past few decades, many research studies have focused on the cyclic response and liquefaction behavior of sand and clay. The process of liquefaction occurs in sand under intense earthquake shaking, resulting in a complete loss of soil stiffness and strength. Although clay generally behaves differently than sand under the same earthquake shaking conditions, some clays may exhibit strength softening behaviors. The behaviors of sand and clay under cyclic loading have been well documented allowing geotechnical engineers to make more accurate assessments for engineering design and applications. In recent years, geotechnical engineers have faced challenges in seismic design of gravelly soils and mine waste rock materials. Due to the limited data available for such materials, cyclic response and liquefaction behavior are assessed on a case-by-case basis often with a high level of uncertainty. The purpose of this research is to address these challenges by performing a liquefaction study of gravel-sand-fines mixtures with varying amounts of each soil composition.

This study focuses on the cyclic response and liquefaction behavior of soils comprised of gravel, sand, and fine particles. It is well known that saturated, loose sand liquefies during earthquake shaking, and the effects of fines content in sand have been extensively studied in prior research. Case histories show that sand containing some

amount of gravel may also experience liquefaction. However, research studies that systematically investigate the influence of gravel on liquefaction phenomena are limited. According to the unified soil classification system, gravelly soils are soils composed primarily of gravel. Pure gravels or gravel-sand mixtures containing mostly gravel can be classified as poorly or well graded gravels (GP or GW), depending on the particle size distribution of the soil. When the fines content is larger than 12 percent, gravel-fines mixtures can be classified as silty or clayey gravel (GM or GC). Gravelly soils are generally found in natural alluvial soil deposits and man-made structures, including mine waste storage. These materials typically consist of gravel, sand, and fine particles. In the mining industry, mixtures of gravel, sand, and fines are commonly found as a result of the mineral extraction process. An increased understanding of mine waste behavior is one of the primary priorities of geotechnical engineering research as a vast amount of these materials have been accumulated in storage facilities in a relatively short span of time. Waste rock materials are dumped or reused as rockfill dams in mining facilities as shown in Figure 1.1. Several major failures of mine tailings dams have occurred in the past few decades leaving a significant impact on humans and the environment.

1.2 Research Overview

Numerous case histories demonstrate that soil liquefaction and strength softening can cause catastrophic ground failure and foundation collapse (e.g., Andrus 1994, Harder and Stewart 1996, Yan and Lum 2003, Rico et al. 2008, Blight 2009, Cao et al. 2011, Rinehart et al. 2016). Liquefaction is a failure phenomenon that occurs in cohesionless soils (e.g., sands and silts), whereas strength softening occurs in clays. Over the past few decades, many catastrophic failures have occurred in gravelly soils consisting of gravel,

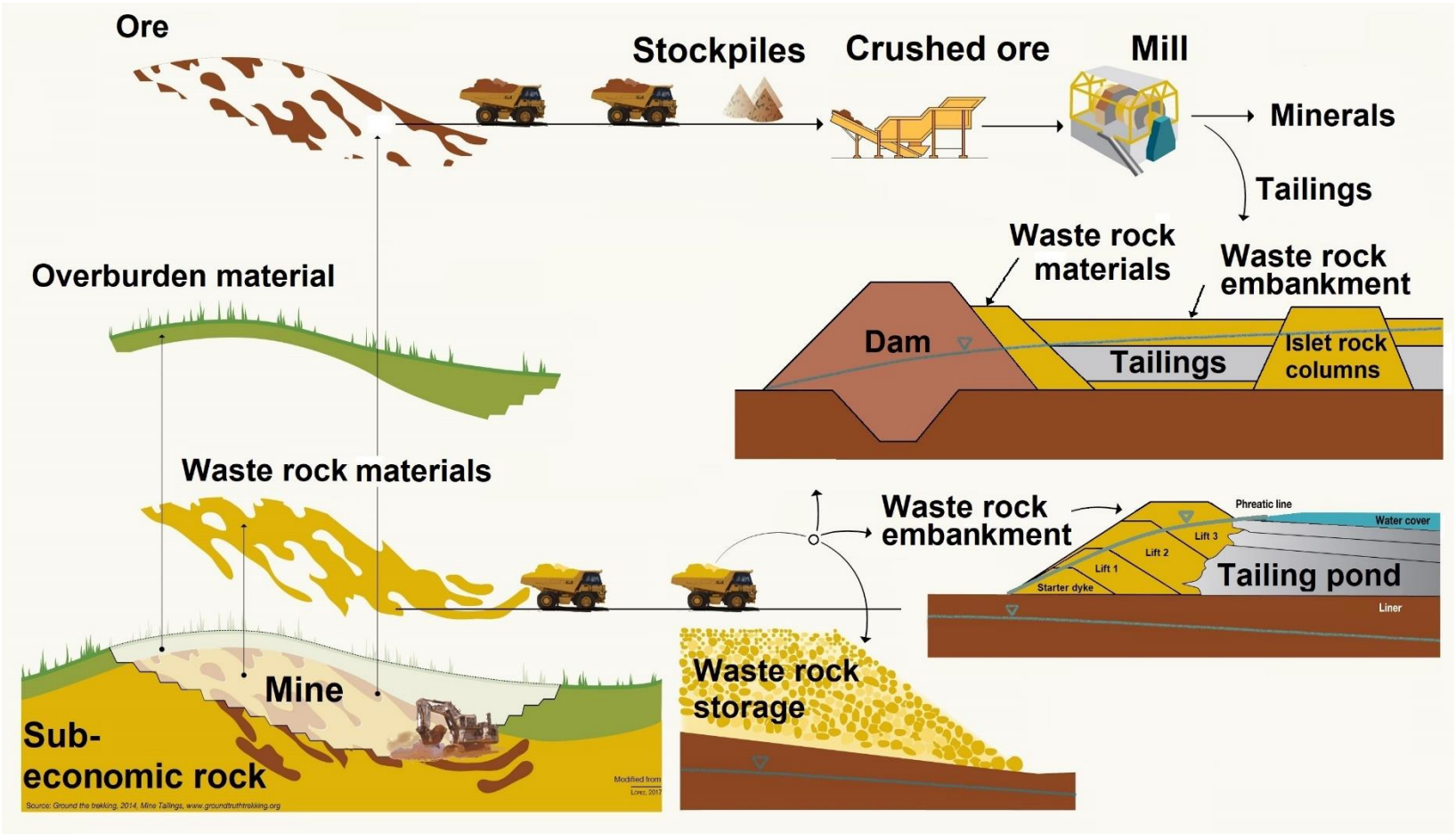

Figure 1.1 Tailings and waste rock materials produced from mining process (modified from Thygesen 2017 and Bussière 2004).

sand, and fine particles (such as waste rock materials, and alluvial soil deposits). Recently, tailings dam failures have been reported throughout the world (Owen et al. 2020) as a consequence of liquefaction. These failures include the Nandan Tin mine in China in 2000, San Marcelino mine in Philippines in 2002, Pinchi Lake mine in Canada in 2004, Tashan mine in China in 2008, Kingston fossil plant in USA in 2008, Huancavelica mine in Peru in 2010, Kolontár mine in Hungary in 2010, Padcal mine in Philippine in 2012, Herculano mine in Brazil in 2014, Germano mine in Brazil in 2015, San Kat Kuu and Lamaungkone mines in Burma in 2015, Kokoya Gold mine in Liberia in 2017, Huancapatí mine in Peru in 2018, Córrego de Feijão mine in Brazil in 2019, Hpakant mine in Burma in 2020, San Antonio de María mine in Peru in 2021, and the Banjhiberana village mine in India in 2022. Due to the liquefaction potential of alluvial materials, many water-retention dams constructed prior to the 1960s are in critical condition because of the lack of design criteria for removing alluvial materials (containing gravel) that support the foundation of dams (Abbaszaden and Wu 2018).

Cyclic response and liquefaction behavior of composite soils comprised of gravel, sand, and fines (silt and clay) are investigated in this study to develop liquefaction susceptibility criteria for gravelly soils. It is due to the lack of liquefaction susceptibility criteria available for these gravelly soils. Several researchers evaluated the effects of soil composition on cyclic response such as the relationships between gravel and sand contents (Holtz and Gibbs 1956), gravel and fines contents (Holtz and Ellis 1961), and sand and fines contents (Vallejo and Mawby 2000). However, the liquefaction behaviors of gravelly soils consisting of gravel, sand, and fine particles are not well understood.

The cyclic response and liquefaction behavior of soils containing various amounts of gravel are examined in this study using cyclic triaxial testing and centrifuge modeling testing. The scope of this study is divided into two topics (see Figure 1.2): Topic 1) cyclic response of undisturbed and reconstituted gravelly soils under triaxial testing conditions, and Topic 2) centrifuge modeling of liquefaction behavior of gravelly soils. Detailed background and methodology for each research topic are provided in the following sections.

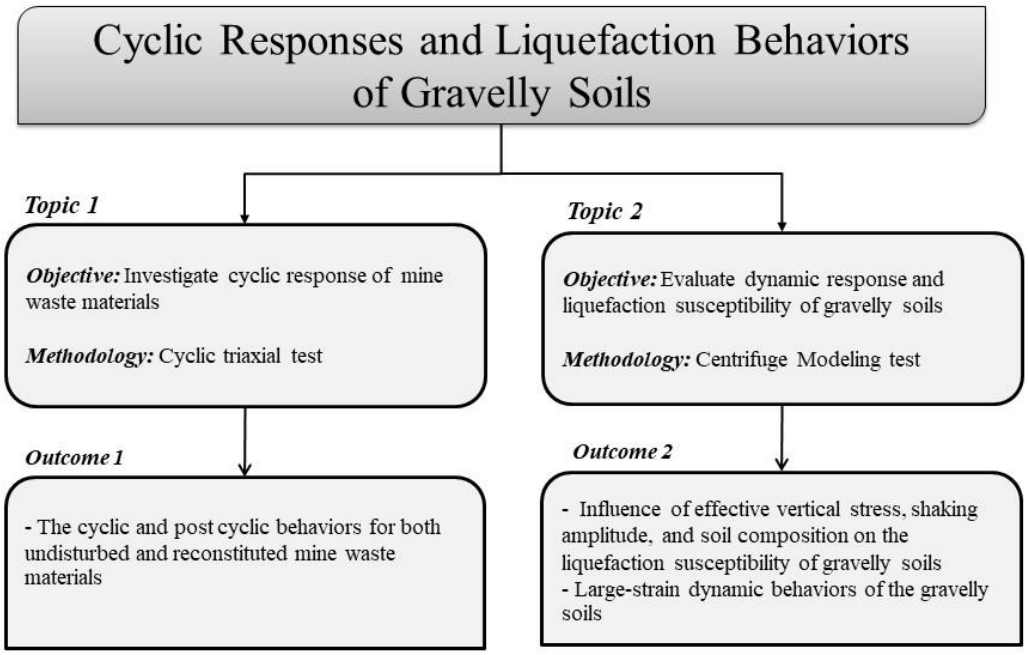

Figure 1.2 Summary of the study.

1.2.1 Background and Methodology for Research Topic 1: Cyclic Response of Undisturbed and Reconstituted Gravelly Soils under Triaxial Testing Conditions

Waste rock is the material left over from mineral extraction for economic interest and is typically comprised of gravel, sand, and fine particles. It was typically found that the change in the soil gradation of waste rock materials is accelerated as a result of the

chemical weathering process caused by industrial chemicals contaminating the soil. As a result of the decomposition of soil particle size, the behaviors of waste rock materials change with the time taken to deposit. Moreover, due to limitations related to their large particle size, large sample size, and high-stress requirement, waste rock materials have not been widely studied. Cyclic triaxial (CTX) testing on gravelly soils is generally preferred over direct simple shear (DSS) testing since the CTX testing is relatively more simple and can accommodate larger sample sizes than DSS tesing. However, the disadvantage of the CTX testing is in its unrealistic loading conditions that do not replicate realistic earthquakes. The compression and extension loading direction in the CTX testing causes the principal stress reversal and overestimates the cyclic resistance ratio of the soil. Despite these issues, the CTX tests are more widely used than the DSS tests but the interpretation of the CTX results should be done with caution.

In this study, the stress-controlled CTX testing is performed on reconstituted and undisturbed gravelly soil samples to investigate the cyclic response and liquefaction behavior under a range of cyclic loading tests, while the resonant column (RC) is performed on undisturbed gravelly soil samples to investigate their low-strain dynamic behaviors. Based on the maximum particle size, the sample is prepared with a diameter of 100 mm to accommodate the particle size to specimen diameter (1:6) ratio suggested in ASTM D5311M-13. The effects of various soil compositions and effective stresses on the cyclic resistance ratio at a given earthquake magnitude of 7.5 ($CRR_{M=7.5}$) are evaluated. Dynamic properties are also characterized based on the shear modulus and damping obtained for the CTX test results at high-strain levels, and results are merged with the low-strain shear modulus and damping obtained from the RC test. In addition, the post-cyclic behavior of

the gravelly soils is evaluated using the isotopically consolidated undrain (CIU) triaxial testing in terms of compression strength and results are compared with the strength prior to and at the onset of liquefaction. The effect of soil composition on soil liquefaction is thoroughly assessed based on the matrix soil structure of composite soils containing gravel, sand, and fines.

1.2.2 Background and Methodology for Research Topic 2: Centrifuge Modeling of Liquefaction Behavior of Gravelly Soils

Centrifuge modeling has several advantages over CTX and DSS tests providing simulations of field geostatic stress condition, pore pressure development profile, and realistic loading conditions such as an earthquake. However, the disadvantage of centrifuge modeling is the limited depth of the soil profile which may not be able to replicate deep soil profiles. To date, only a few centrifuge modeling studies of liquefaction of gravelly soils are available. For example, Antonaki et al. (2018) performed centrifuge testing on mine waste material consisting of various mixtures of gravel and fine-grained tailings.

Previous research studies have mainly focused on gravelly soils comprised of either 100% gravel particles, a mixture of gravel and sand, or gravel and clay. (e.g., Athanasopoulos-Zekkos 2020, Xu et al. 2019, Antonaki et al. 2017, Wu 2018, Chang and Phantachan 2016, Ghalesari and Rasouli 2014, Kokusho et al. 2004, Lin et al. 2000, Evans and Seed 1987). However, the composite soils comprised of gravel, sand and fines have not been widely studied, and the cyclic response and liquefaction behavior of the composite soils are limited.

In this study, liquefaction behavior of various gravelly soil mixtures under different cyclic loadings are evaluated using centrifuge modeling. The effects of two variables are

investigated: shaking amplitude and soil composition. Concurrently with the shaking event, acceleration and pore pressure behaviors along the soil profile depth are recorded to analyze the stress-strain-pore pressure behaviors. The number of cycles to cause liquefaction of each soil layer are measured at each shaking amplitude. In addition, the post-test investigation for each soil layer is presented to aid in evaluating the post-liquefaction behavior of gravelly soil subjected to different base shaking events in terms of lateral strain, volumetric strain, and particle rearrangement.

1.3 Research Questions

Findings from this study will address the research questions listed below. The contents relevant to each research question (RQ) are indicated in a conceptual research map presented in Figure 1.3. This conceptual map describes the methodologies and outcomes required to evaluate the liquefaction behaviors and dynamic responses of gravelly soils regarding several variables (e.g., shaking intensity, effective stress, soil composition, relative density, and permeability). The literature to support the contents in the research map are illustrated in Chapter 2. Based on a review of the relevant literature, this study focuses on two primary areas. First, the research will utilize the CTX to evaluate cyclic response of mine waste rock materials. Second, the research will provide centrifuge modeling data to evaluate liquefaction behavior of gravelly soil mixtures, comprised of gravel, sand, and fines.

Research Question for Topic 1: Is it possible for a gravelly soil with a certain ratio of gravel, sand, and fines to liquefy under CTX conditions? How do the liquefaction behaviors of gravelly soils compare with sand?

Hypothesis for Topic 1: Under CTX conditions, a gravelly soil comprised of gravel, sand, and fines may liquefy if the percentage of finer particles (sand and fines) exceeded a certain threshold value. The material may behave like sand under liquefaction; however, gravelly soils may have the ability to regain strength due to dilation during post-cyclic loading test.

Research Question for Topic 2: What are the effects of various soil compositions and shaking amplitude on the liquefaction behaviors of gravelly soils simulated in centrifuge modeling tests?

Hypothesis for Topic 2: In the centrifuge modeling tests, gravelly soil is more susceptible to liquefaction when containing more sand. It is possible that fine particles help to prevent significant loss of shear strength during liquefaction.

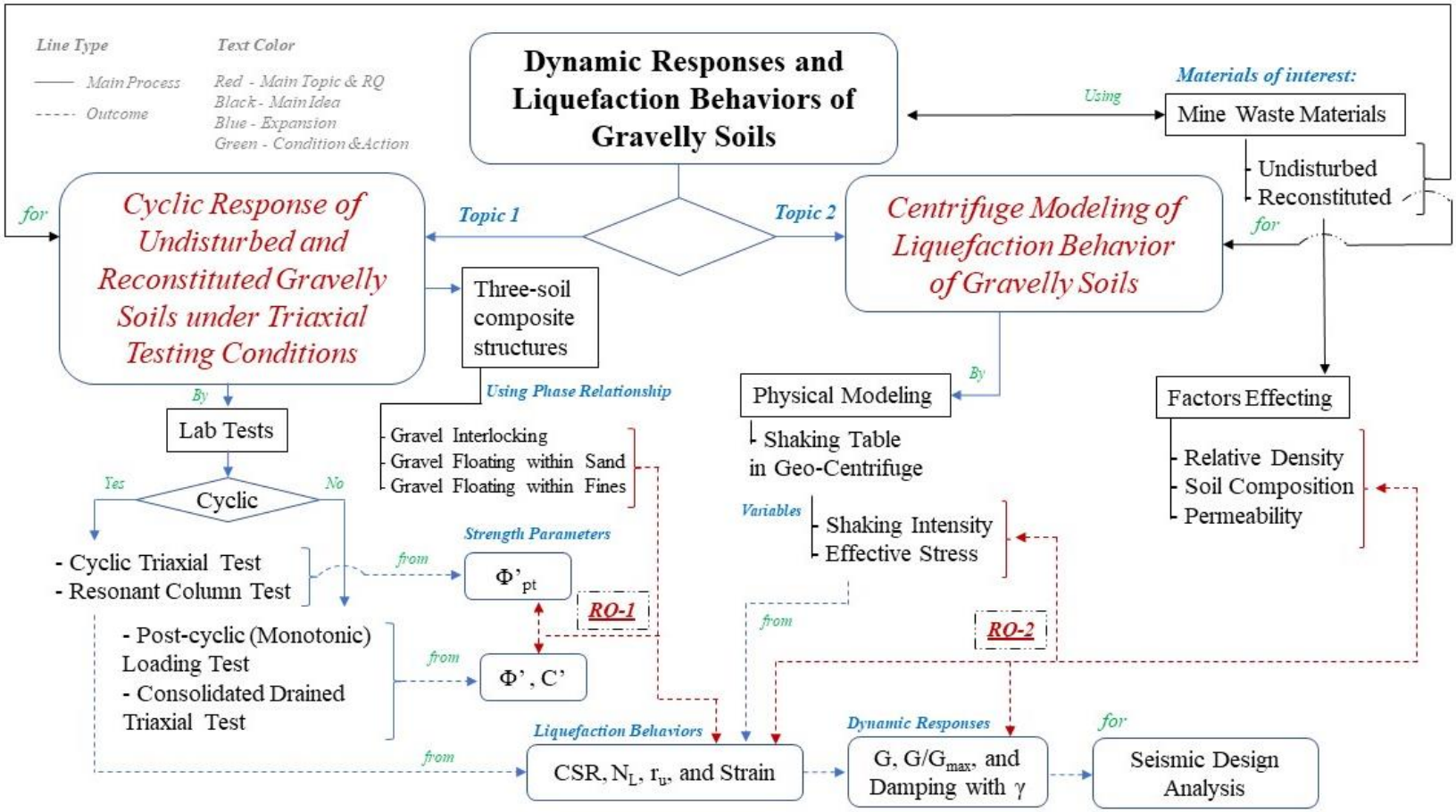

Figure 1.3 Conceptual map for this study.

1.4 Research Objectives

Two research objectives have been developed to answers the research questions:

Research Objective for Topic 1: Evaluate the cyclic and post-cyclic behaviors of undisturbed and reconstituted gravelly soils in undrained triaxial testing by measuring the change in stress-strain-pore pressure behavior.

Research Objective for Topic 2: Evaluate the effects of various soil compositions and shaking amplitude on liquefaction behaviors of gravelly soil mixtures using the centrifuge modeling for assessing liquefaction susceptibility.

1.5 List of Papers and Structure of Dissertation

This dissertation includes results that have been published previously and results that are currently undergoing peer review for publication in conferences and journals. Separate chapters of this dissertation include three conference papers and three journal papers. Two conference papers have been published, while two journal papers are under revision. Also, two more papers are being prepared for special publication at a conference and in a journal.

Special Publications from Conference Papers:

1. Sasanakul, I., Gassman, S., Ruttithivaphanich, P., and Dejphumee, S. (2019). "Characterization of shear wave velocity profiles for South Carolina Coastal Plain." *AIMS Geosciences, 5*(2), 303.

2. Ruttithivaphanich, P., and Sasanakul, I. (2019). "Frequency Effects on Low-Strain Shear Modulus and Damping for Natural Clays and Silts." In *Geo-Congress 2019:*

Geotechnical Materials, Modeling, and Testing (pp. 590-598). Reston, VA: American Society of Civil Engineers.

3. Ruttithivaphanich, P., and Sasanakul, I. (2019). "Normalized Shear Modulus and Damping of Tertiary and Cretaceous Soils from South Carolina Coastal Plain." *Poster Presentation for Geo-Carolinas 2019.*

4. Sasanakul, I, Ruttithivaphanich, P., and Dejphumee, S. (2022). "Dynamic Characterization of Mine Waste Rock in Centrifuge Testing." *In 10th International Conference on Physical Modelling in Geotechnics, KAIST, Daejeon, Korea*

5. Ruttithivaphanich, P., and Sasanakul, I. (2022). "Liquefaction Evaluation of a Gravel-Sand Mixture Using Centrifuge Tests." *In Geo-Congress 2022,* 288-296.

Peer-Reviewed Journal Papers:

6. Ruttithivaphanich, P., and Sasanakul, I. (2022). "Centrifuge modeling studies on effects of composition on liquefaction of mine waste rock" *Soil Dynamic and Earthquake Engineering.*

7. Ruttithivaphanich, P., and Sasanakul, I. (2022). "Centrifuge Modeling of Fines Content Influence on Liquefaction Behaviors of Loose Gravelly Soils." *Journal of Geotechnical and Geoenvironmental Engineering, ASCE* (Under review)

The dissertation is structured as follows: Chapter 1 provides an introductory outline of the motivation and methodology with an objective for each research topic. Chapter 2 presents a summary of background and previous research studies that provide the context necessary to comprehend the concept and behavior of dynamic response prior to and post-liquefaction. Chapters 3 through 4 present the investigation conducted for each research

topic, including some details from the research papers mentioned previously. The conclusions and suggestions for future study are presented in Chapter 5.

CHAPTER 2

BACKGROUND AND LITERATURE REVIEW

2.1 Introduction

The dynamic behaviors of gravelly soils comprised of gravel, sand, and fine particles are limited, especially mine waste materials disposed of by the mining industry. The main products of the industry are mine wastes and tailings (Gajić et al. 2018). Those materials are dumped freely into separate storage areas located near mine sites as shown in Figure 1.1 (Blight, 2009). In the last few decades, the storage failures have had a huge impact on people and the environment in the area, such as the failure of Fundão tailings dam at Samarco iron mine in Brazil in November 2015. It resulted in toxic metal contamination of more than 650 km of the Carmo and Doce river (Hatje et al. 2017). The tailings dam failure may occur under either static or dynamic conditions (Psarropoulos and Tsompanakis 2008, Lyu et al. 2019), such as rainfall induced excess pore pressure, or ground shaking induced liquefaction or strength softening.

In general, liquefaction is a phenomenon that occurs in cohesionless soils (e.g., sands, and silts), whereas strength softening occurs in clays. Numerous case histories revealed that liquefaction can occur in gravelly soils (e.g., Coulter and Migliaccio 1966, Stokoe et al. 1988, Evan and Harder 1993, Kokusho et al. 1995), and catastrophic damages due to liquefaction of gravelly soils have been documented in several case histories (e.g., Andrus 1994, Harder and Stewart 1996, Yan and Lum 2003, Rico et al. 2008, Blight 2009,

Cao et al. 2011, Rinehart et al. 2016). However, the liquefaction behaviors of natural gravelly soils are not well understood. Although several researchers studied the cyclic behaviors of mine tailings (e.g., Antonaki et al. 2018, Geremew and Yanful 2013, Jame et al. 2011, Zhang et al. 2005), the cyclic behaviors relating of mine waste composed of gravels is limited.

This research study consists of two main topics: cyclic response of undisturbed and reconstituted gravelly soils under triaxial testing conditions (Topic 1), and centrifuge modeling of liquefaction behaviors of gravelly soils (Topic 2). The theoretical development, experimental design and procedure, experimental plan, analysis and discussion of results, and evaluation of research objectives are addressed for each research topic in Chapter 3 and 4. This chapter presents the literature review relevant to both topics. The chapter organization begins with failure criteria under the cyclic loading conditions, effect of soil composition, laboratory tests, effect of membrane compliance, monotonic and post-cyclic behaviors, and dynamic centrifuge modeling.

2.2 Failure Criteria of Cyclic Loading Tests

In general, the liquefaction failure of cohesionless soils may transform soil from solid to liquid state, whereas cohesive soils fail due to strength softening under the cyclic loading. However, the failure mechanism under the cyclic loading of the composite materials comprised of gravel, sand, and fine particles is still not well understood due to the influence of various soil compositions. Wu et al. (2004) provided a summary of the typical triggering criteria for liquefaction based on the cyclic response of the liquefiable

soils. The failure criteria can be categorized into three main groups: pore water pressure stress and strain-based criteria.

2.2.1 Pore Water Pressure-Based Criteria

For the pore water pressure-based criteria, the excess pore water pressure (r_u) of 1.0 is ideally selected as a concept of zero effective stress when the liquefaction failure occurred; however, the soil sample can liquefy when the r_u is less than 1.0. Wu et al. (2004) conducted cyclic loading tests on 81 liquefiable soil samples (see in Figure 2.1) and found that approximately 80% of them liquefied with r_u was higher than 0.95. Figure 2.2 also presents the variation of liquefaction triggering at different relative densities. It was found that liquefaction should be considered when the r_u is higher than 0.85. The liquefaction is triggered at a lower r_u for samples with lower relative density. Therefore, the r_u required to trigger initial liquefaction varied with the densities of the soil sample and loading conditions applied to the soil specimens. Ishihara (1993) also observed that the r_u of samples with fine particles did not reach 1.0 when the failure occurred. In addition, pore water pressure would stop developing at r_u of approximately 0.90 to 0.95 since the rate of pore water pressure equalized across the specimen is relatively slow in comparison to the rate of cyclic loading, due to the effect of fine particles (Wu et al. 2004). It should be noted that the pore pressure development is soil behaviors under cyclic loading, and the pore water pressure-based liquefaction criteria are applied to other testing methods.

2.2.2 Strength-Based Criteria

For the strength-based criteria, significant loss in strength occurs predominantly under a stress-controlled cyclic loading condition. When the r_u higher than 0.8, the

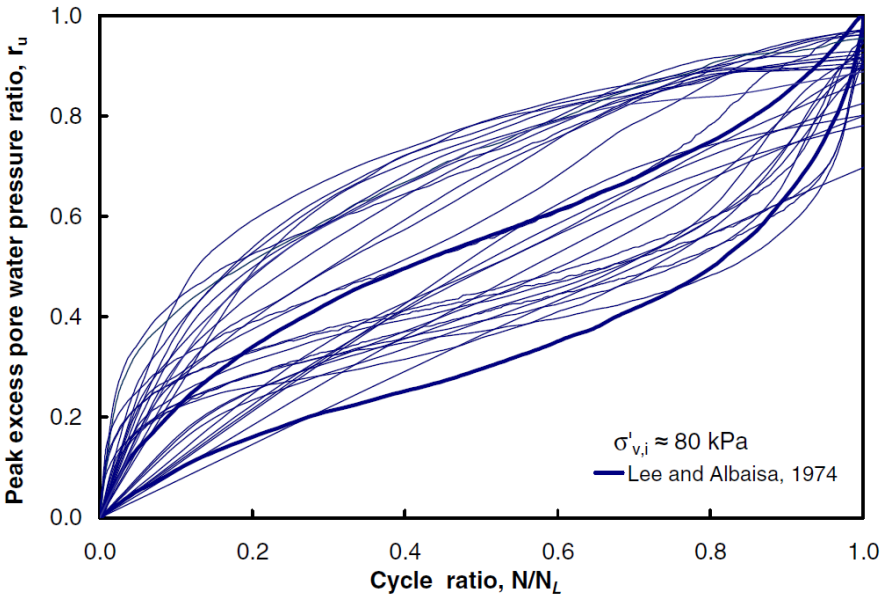

Figure 2.1 Pore water pressure developing in cyclic simple shear tests (Wu et al. 2004).

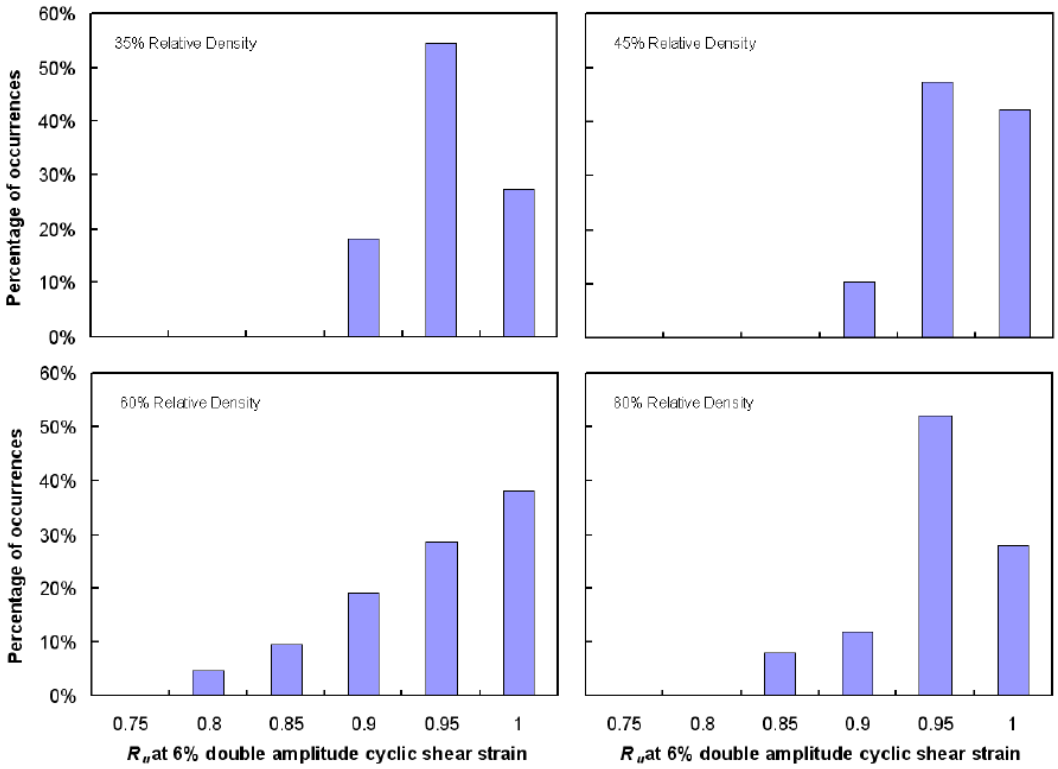

Figure 2.2 Distribution of pore water pressure ratio at liquefaction triggering (Wu et al. 2004).

reduction in strength is higher as pore pressure increases. The decrease in strength can indicate the loss in stiffness of the specimen. This behavior was typically found when the liquefaction is triggered in cohesionless soils, which behave similarly to a viscous fluid (Wu et al. 2004). For some cohesive materials, there was no significant loss of stiffness while the cyclic softening behavior remained dominant during failure. Therefore, there is no clear strength-based liquefaction criteria for clayey soils.

2.2.3 Strain-Based Criteria

For strain/deformation-based criteria, the liquefaction failure can be captured when there is no resistance to deformation, causing excessive deformation (Seed and Lee, 1966). Wu et al. (2004) studied the failure criteria of the liquefiable materials and captured flow stain behavior at the double amplitude (DA) of stain higher than 6% (see in Figure 2.3). The relationship between flow strain and maximum shear strain is shown in Figure 2.4. Ishihara (1993) recommended 5% DA and 3% single amplitude (SA) of the axial strain as the failure criteria to determine the appearance of liquefaction and cyclic softening based on laboratory and field studies, respectively. Hubler et al. (2017) suggested the SA shear strain of 3.57% as liquefaction criteria for gravelly soils as an agreement with Vaid and Sivathayalan (1996), and Sivathayalan (2000). Based on these literature reviews, the strain criteria are extremely sensitive because it is a challenge to precisely evaluate the strain level at the onset of liquefaction.

2.3 Effect of Soil Composition

Numerous researchers have studied the cyclic response to soil mixtures (e.g., Holtz and Ellis 1961, Evans and Zhou 1995, Vallejo and Mawby 2000, Hubler 2017, Xu

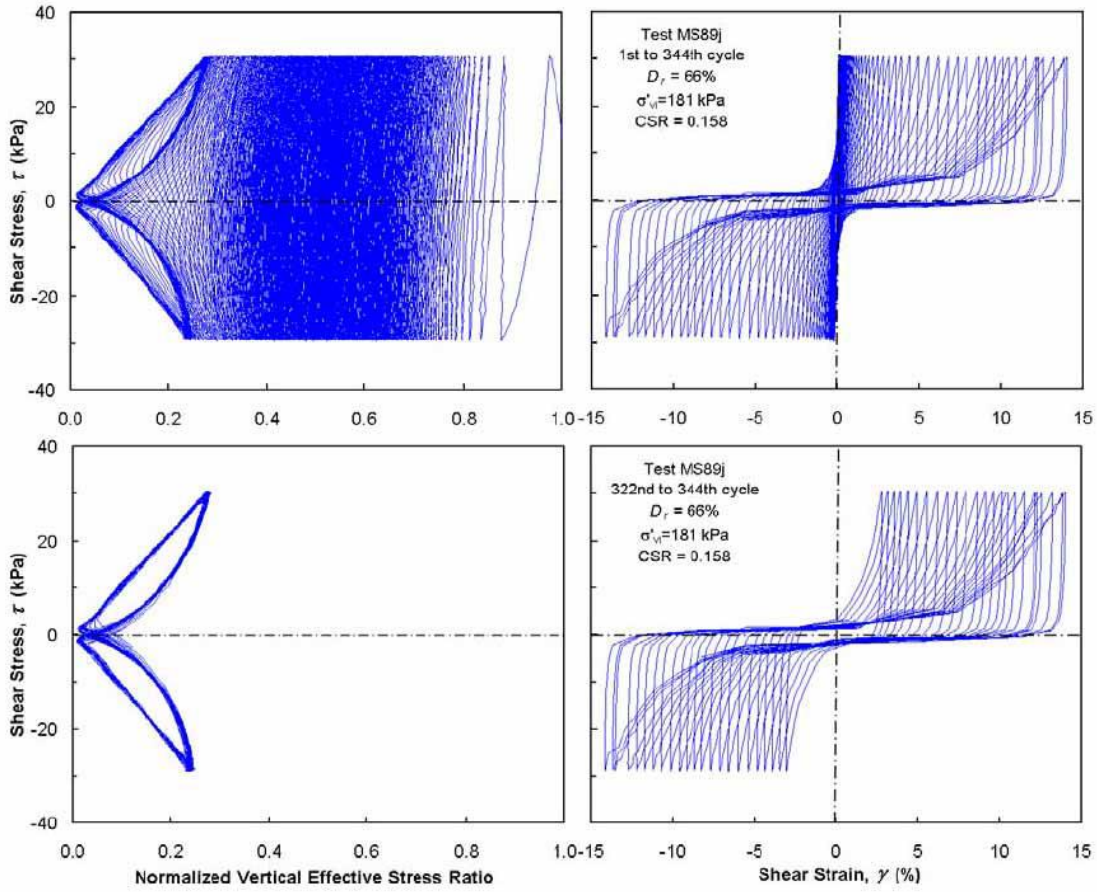

Figure 2.3 Cyclic behavior and post-liquefaction behavior of Monterey sand (Wu et al. 2004).

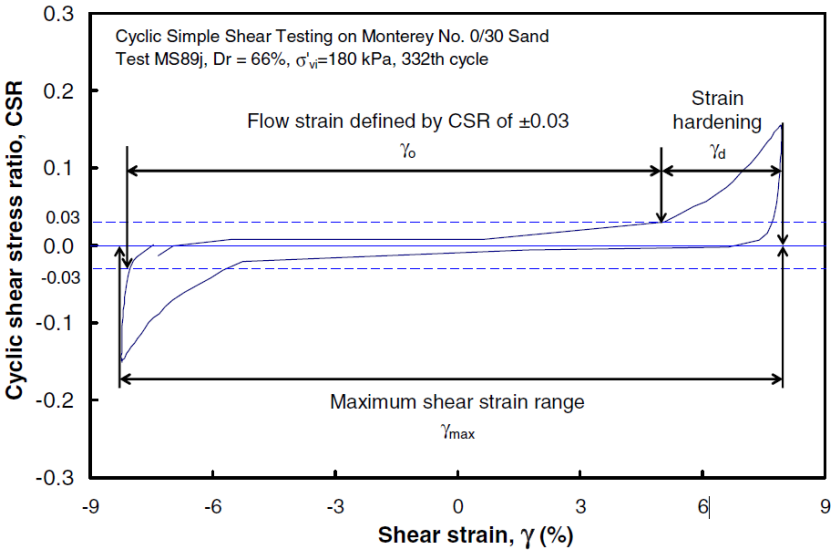

Figure 2.4 Behavior of shear strain of post failure mechanism (Wu et al. 2004).

et al. 2019). Almost all of them focused on artificial soil samples containing two soil compositions such as gravel-sand, gravel-fines, and sand-fines particles. However, natural or man-made soils consist of various soil particle sizes. A mixture of gravel, sand, and fine particles are found in alluvial and fluvial soil deposits and/or used as construction material for an embankment dam, and often found as mine waste rock in mining facility. Based on numerous case histories, it was found that gravelly soil mixtures are liquefiable (e.g., Coulter and Migliaccio 1966, Stokoe et al. 1988, Evan and Harder 1993, Kokusho et al. 1995).

Holtz and Gibbs (1956) investigated the shear strength behavior of sandy gravels using unconsolidated undrained triaxial tests and found two distinct categories of results: the gravel content less than 20% and higher than 20%. Friction angle increases as the gravel content increases for the sample with a gravel content of less than 20%. However, friction angle significantly increases with the increasing gravel content for the sample with a gravel content of higher than 20%. Holtz and Ellis (1961) also studied the strength behavior of clayey gravels and found that the influence of gravel particles is dominant when gravel content higher than 35%; friction angle significantly increases while cohesion decreases as gravel content increases. However, a clayey gravel with gravel content less than 35%, the soil behaves similarly to clayey soils. Vallejo and Mawby (2000) performed a series of direct shear tests to examine the shear strength behavior on gravel-clay mixtures. Three dominant ranges were evaluated including gravel content over 75%, gravel content below 40%, and gravel content between 40% and 75%. A mixture composed of gravel content higher than 75% and less than 40% behaves similarly to pure gravelly soil and pure clayey

soil, respectively. For the mixture composed of gravel content between 40% and 75%, the shear strength was partially influenced by the granular phase.

Additionally, the particle shape is a factor affecting the shear strength of clay-gravel mixtures because the peak friction angle is related to the volumetric dilation (Li et al. 2013). Holtz and Gibbs (1956) also found that sub-rounded particles have less shear strength than angular particles although there is no available standard method for determining the particle shape of the specimens (Corriveau et al. 2005). It was also found that particle angularity and particle size have some impacts on the post-peak behavior of gravelly soils due to the effect of particle interlocking. Either more angular or larger particles are more difficult to rearrange (Hubler et al. 2014, Hubler et al. 2017). In summary, the key factors affecting the shear behavior of gravelly soil mixtures are gravel content, particle size gradation, particle shape, particle breakage, void ratios, and water content (Holtz 1961, Charles and Watts 1980, Seed et al. 1986, Sun et al. 2014).

The effect of soil composition on cyclic behaviors has been investigated in laboratory using direct simple shear (DSS) and cyclic triaxial (CTX) tests by numerous researchers. Chang and Phantachan (2016) studied gravel-sand mixtures using DSS testing. The gravel content of sand-like gravelly soil was found to have a small impact on the normalized stress-strain curve. The shear resistance decreases as the gravel content increases in the well-graded sand mixtures, and the shear resistance has little effect on the gravel content for loose gravelly soils. However, Evans and Seed (1987) stated that no difference in cyclic behaviors was found in gravelly soils with varying particle sizes. Xu et al. (2019) also studied sand-gravel mixtures using DSS testing and found that the number of cycles required to cause liquefaction (N_L) increases as the gravel content increases. The

shear modulus (G) and N_L decrease as gravel content increases in the transitional state specimen due to a change in void ratio during the particle rearrangement process, resulting in sample stiffening during liquefaction. It was found that the material damping of the sand-gravel mixtures decreases as the cyclic stress increases. The shear strain experienced at first few hysteresis loops in cyclic loading tests was partially dependent on the loading frequency, and this effect of frequency was less at a loading frequency of higher than 0.05 Hz. (Xu et al. 2019).

Abbaszadeh and Wu (2018) performed CTX testing on the clay-gravel mixtures and found that the stress induced during the cyclic loading was higher than the shear strength. Haeri et al. (2018) found that the cyclic resistance increases with increasing static shear stress under low confining pressure leading to the less pore water pressure development. The effect of water dissipating time through the void space of gravelly soils with less fines shown that dense, well-graded materials are less prone to liquefaction than loose, poorly graded materials. Large flow-deformations may be found in the loose materials; however, the gravelly soil may not be susceptible to liquefaction during the cyclic loading tests (Hubler et al. 2017). Basham and Athanasopoulos-Zekkos (2020) studied on the gravelly slope soils by using both CTX and DSS devices. The cyclic resistance ratio (CRR) was found to be impacted by horizontal static shear stress (α) since the specimen was subjected to a few loading cycles prior to liquefaction. The α increases as the excess pore water pressure at initial liquefaction (Δu_L) decreases. The Δu_L decreases while the N_L increases as the shear strength increases, resulting CRR increases. These behaviors of the gravelly materials were similarly observed in both CTX and DSS tests (Basham and Athanasopoulos-Zekkos 2020).

Additionally, the shear modulus of the gravelly cobble specimens tested in both CTX and resonant column (RC) tests was found to be highly related to the particle size and confining pressure (Lin et al. 2000). However, Kokusho et al. (2004) found that the relative density was more influent to the undrained cyclic strength of gravelly soils than particle gradation (similar as Hubler et al. 2017). While contractive behavior was dominant in the loose gravelly soils over the wide range of gravel content (Rashidan et al. 1995, Towhata et al. 1988), the dilative behavior was significant in the medium dense to dense granular soils (Antonaki et al. 2018, Zeghal et al. 1996, Zeghal and Elgama 1994).

2.4 Laboratory Tests for Determining Cyclic Response

2.4.1 Cyclic Loading Tests

Cyclic loading tests are commonly performed in the laboratory using direct simple shear (DSS) and cyclic triaxial (CTX) devices to measure the large-strain cyclic resistance of soil samples. The loading direction in the DSS testing is more representative of the earthquake excitation than that in the CTX testing (Basham and Athanasopoulos-Zekkos 2020).

Lewis et al. (2013) found that the effect of maximum particle size on cycle strength was low to negligible. In contrast, Ghafouri (2018), and Haei et al. (2018) suggested that the effect of the specimen size should be considered especially in the gravel soils. In addition, the ASTM D4767 recommends that the suitable specimen diameter (D) should be higher than six times maximum particle size (d) or $D \geq 6\ d$. As a result, the conventional DSS testing devices are challenging to implement for gravelly soil samples. To overcome the limitation of the DSS testing device, a large cyclic direct simple shear (DSS) device

was developed by Zekkos et al. (2016), especially for testing gravelly soils containing over-size particles. However, the large DSS testing device is not typically available in most Geotechnical laboratories. Based on the suggested dimension ratio mentioned previous, the conventional cyclic triaxial testing device may be applicable for some gravelly soils, having a maximum particle size smaller than 1/6 times of specimen diameter.

The cyclic loading tests mentioned previously can be performed both stress- and strain-controlled modes in accordance with ASTM D5311 and Vucetic and Dobry (1988), respectively. Due to the mechanical limitations of the devices, it should be noted that all of the tests described previously typically use sinusoidal loading at a loading frequency less than 10 Hz. The stress-controlled mode is appropriate for soils which have partial flow-failure due to the specimen's ability to sustain any load during the failure. If the sample exhibits flow failure, the excessive strain would be dominant due to a complete loss of strength. Therefore, the strain-controlled mode is considered for liquefiable materials having flow failure since the soil strength changes rapidly during the cyclic loading.

2.4.2 Determination of Shear Stress-Strain Modulus from Cyclic Triaxial Results

The results obtained from the direct simple shear (DSS) and cyclic triaxial (CTX) testing methods can be compared to describe strength parameters during cyclic and post cyclic behavior, although the deformation and stress conditions in both type of tests are different, leading to strain (ε) differences in the overall state of stress (Pyke, 1979). In CTX tests, the stress-strain loop was observed as symmetrical and unsymmetrical. These were called isotropic and anisotropic loop behavior, respectively (Pyke, 1978). Anisotropy is often found in cohesionless materials because the soil has less ability to maintain tensile

loads during the extension loading. This type of loading leads to the excessive strain that occurred in the CTX tests (see in Figure 2.5). Pyke (1978, 1979) proposed that unsymmetrical loops of stress-strain relationship in CTX test should be assessed as the anisotropic behavior in order to convert elastic modulus and axial strain to become shear modulus and shear strain, respectively.

For the isotropic loop behavior, shear modulus (G) can be estimated based on Young's modulus (E) and Poisson's ratio (μ) as:

$$G = E \,/\, [\, 2 \cdot (\, 1 + \mu \,)] \qquad \text{Eqn. 2.5}$$

The shear strain (γ) relevant to the G can be defined as:

$$\gamma = \varepsilon_a - \varepsilon_r = \varepsilon_a \cdot (\, 1 + \mu \,) \qquad \text{Eqn. 2.6}$$

where ε_r and ε_a are the radial and axial strains, respectively.

For the anisotropic loop behavior, different levels of strain occurred due to the extension and compression loading led to the difference in shear modulus in a single cycle. To analyze this behavior, vertical and horizontal Young's modulus (E_v and E_h), Poisson's ratio, for horizontal and vertical plane (μ_{hh} and μ_{vh}), and shear modulus in vertical plane (G_{hv}) are required as suggested by Love (1892). The G_{hv} can be determined as (Barden 1963):

$$G_{hv} = E_v \,/\, (1 + 1/n + 2\mu_{vh}) \qquad \text{Eqn. 2.7}$$

$$n = E_h \,/\, E_v \qquad \text{Eqn. 2.8}$$

Gerrard et al. (1972) recommended the n value ranging from 0.3 to 0.6 for sand and that of 3.0 for the OC-clay. Moreover, the μ_{hh} is reasonably assumed to be equal to μ_{vh}, and the ratio of ε_a over ε_r can be carried out by the following equation (Gerrard et al., 1972).

$$\varepsilon_a/\varepsilon_r = n \cdot [\,(1 - 2\,\mu_{vh})/(1 - \mu_{vh} + n\,\mu_{vh})\,] \qquad \text{Eqn. 2.9}$$

Since the effective confining stress in CTX tests is higher than the vertical stress (σ_v) in the DSS tests, a correction method for adjusting the vertical stress to mean stress (σ_m) in DSS tests is suggested by Park and Silver (1975) as:

$$G_{CTX,aniso} = G_{DSS} \cdot (\,\sigma_v/\sigma_m\,)^{1/2} \qquad \text{Eqn. 2.10}$$

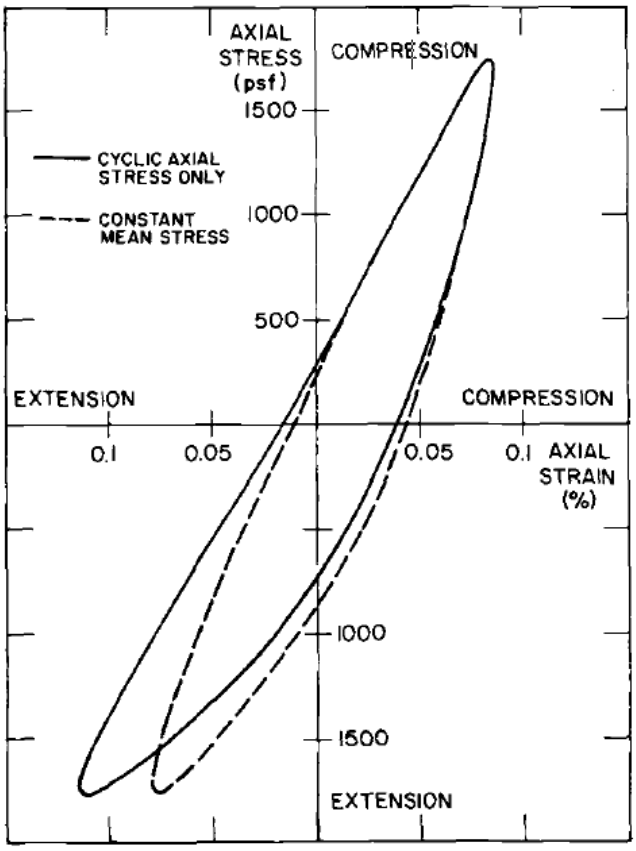

Figure 2.5 Stress-strain relationships obtained in stress controlled cyclic triaxial test at effective stress of 48 kPa (Pyke 1978).

The comparison of shear modulus in both CTX and DSS tests are presented in Figure 2.6. It was found that the correction method works well compared with the data from DSS test. Hence, the coefficient of lateral earth pressure (k_0) of 0.3 was proposed by Park and Silver (1975) to correct the CTX data to DSS data as:

$$G_{aniso} = G_{iso} \cdot (1 - k_0) \qquad \text{Eqn. 2.11}$$

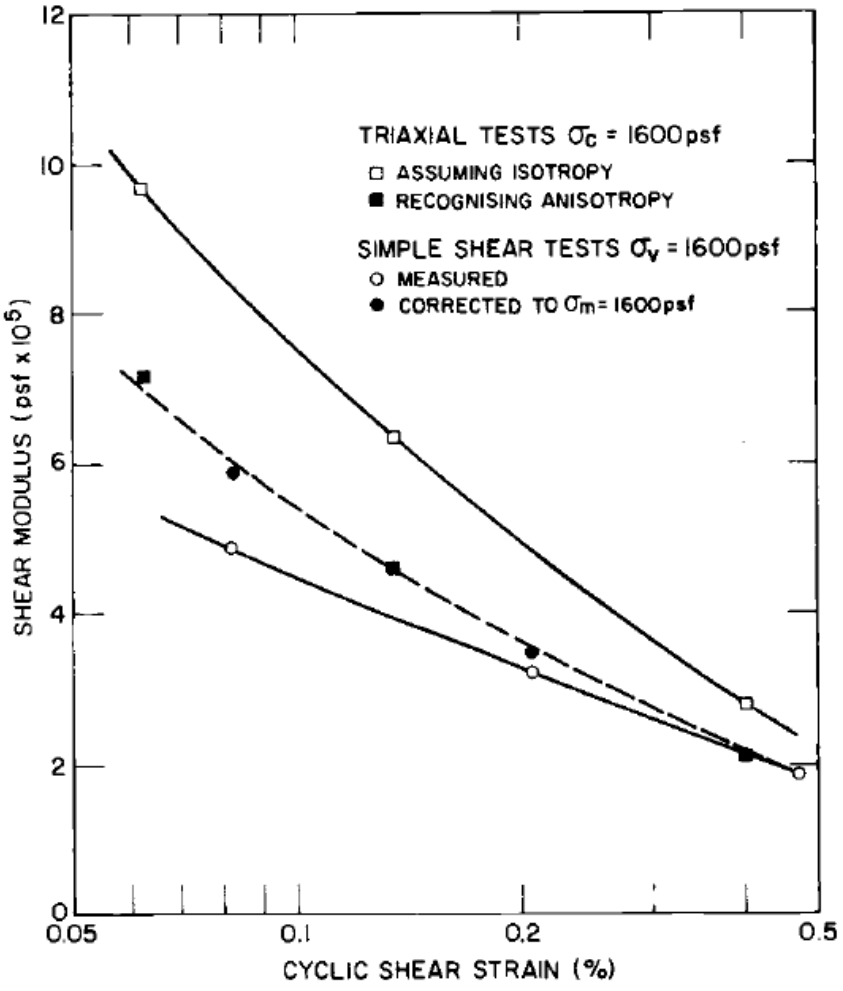

Figure 2.6 Shear modulus behavior obtained from CTX and DSS tests (Pyke 1978).

2.5 Effect of Membrane Compliance

Membrane compliance during triaxial testing may have a significant impact on the development of pore water pressure in granular materials (i.e., pure gravels and coarse sands). Evans and Seed (1987) stated that membrane penetration and rebound lead to the development of pore pressure as a result of water diffusion into inhabited zones through the soil sample and consolidate the grain structure surrounding. Figure 2.7 illustrates the effect of membrane compliance on excess pore water pressure during cyclic loading and unloading. The pore water pressure increases and decreases while the sample is under compression and extension loading, respectively, as presented in Table 2.1.

Table 2.1 Effect of membrane compliance on the soil specimen (Evans et al. 1992).

Item	Compressive Soil	Expansive Soil
Porewater pressure	Increase	Decrease
Confining pressure	Decrease	Increase
Strength of soil	Decrease	Increase

Within the last several decades, numerous researchers have investigated the impacts of membrane compliance and the solutions to minimize the issue. (e.g., Newland and Allely 1957, Lade and Hernandez 1977, Martin et al. 1978, Ramana and Raju 1982, Evan and Seed 1987, Tokimatsu 1990, Nicholson et al. 1993a, Haeri and Shakeri 2010). Two main techniques have been used. For the first technique, the granular specimen is coated by finer and lower stiffness materials to prevent the void at the interface between soil particles and the membrane. Furthermore, the use of low frequency cyclic loading may help minimize the issues, since it allows sufficient time to dissipate additional pore water

pressure developed due to the membrane compliance. Alhani et al. (2018) summarized the physical methods to minimize the impact in Table 2.2.

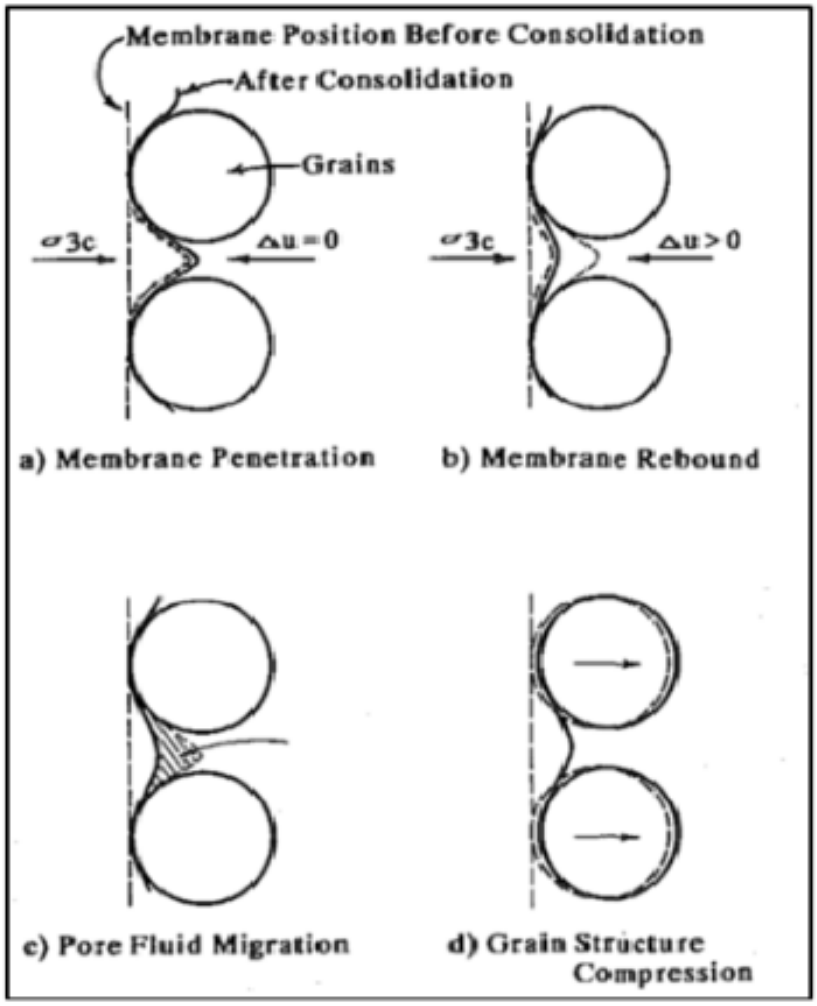

Figure 2.7 Effect of membrane compliance
on cyclic loading test (Evans et al. 1992).

For the second technique using empirical equations, the correction method was applied to the post-testing data. The following equation requires a drained isotropic compression and extension test to determine the unit membrane compliance (ΔB_m):

$$\Delta V_m = \Delta V_T - \Delta V_S = \Delta B_m \cdot A_m \qquad \text{Eqn. 2.1}$$

Table 2.2 Previous studies to minimize the effect of membrane compliance (Alhani et al. 2018).

Researchers	Minimizing methods	Limitations
Wong et al. and Martin et al. (1975, 1978)	Used sample diameter of 300 mm for testing sand specimen in triaxial test.	The use of this diameter for sand samples cannot decrease the effect of membrane compliance (1993)
Chan(1972) and Raju (1980)	Coated side surface of the specimen with polyethylene sheets.	Utilizing this method may contribute to the reduction of membrane compliance but will increase lateral resistances of the sample (1993)
Lade and Hernandez (1977)	Utilized copper sheet for enclosing specimen	Utilizing this method may contribute to the reduction of membrane compliance but will increase lateral resistances of the sample (1993)
Evans and Seed (1987)	Used slurry and fine material for the elimination of coarse grains membrane compliance.	This technique causes deviations of shear strength measurements (1988)
Haeri et al. (2016)	Used sand to surround gravel specimen in triaxial test.	Caused increasing of sample density.

where ΔV_m is membrane penetration, ΔV_T and ΔV_S are total and true soil skeletal volume change and A_m is membrane surface area. As presented in Figure 2.8, ΔB_m was plotted with the effective confining pressure to determine membrane flexibility (f_m). Following that, the skeletal volumetric strain ($\Delta\varepsilon_{v,s}$) was calculated using the equation provided by Newland and Allely (1957) as:

$$\Delta\varepsilon_{v,s} = 3 \cdot \Delta\varepsilon_a \qquad \text{Eqn. 2.2}$$

where $\Delta\varepsilon_a$ is axial strain. Figure 2.9 shows the change of $\Delta\varepsilon_{v,s}$ under varying confining pressures to determine the bulk modulus of the soil (K_s). After obtaining f_m and K_s, the membrane compliance ratio (C_{RM}) was computed as follows:

$$C_{RM} = \frac{A_m}{V_T} \cdot K_s \cdot f_m \qquad \text{Eqn. 2.3}$$

Based on the theoretical equation $\Delta V_{water} = \Delta V_{soil} + \Delta V_m$ from the undrain triaxial test, the excess pore water pressure without the influence of membrane compliance ($\Delta u_{non\text{-}compliance}$) was determined using the following equation provided by (Baldi and Nova 1984).

$$\Delta u_{non\text{-}compliance} = (1 + C_{RM}) \cdot \Delta u_{compliance} \qquad \text{Eqn. 2.4}$$

where $\Delta u_{compliance}$ is the excess pore water pressure during the cyclic loading test under the impact of membrane compliance.

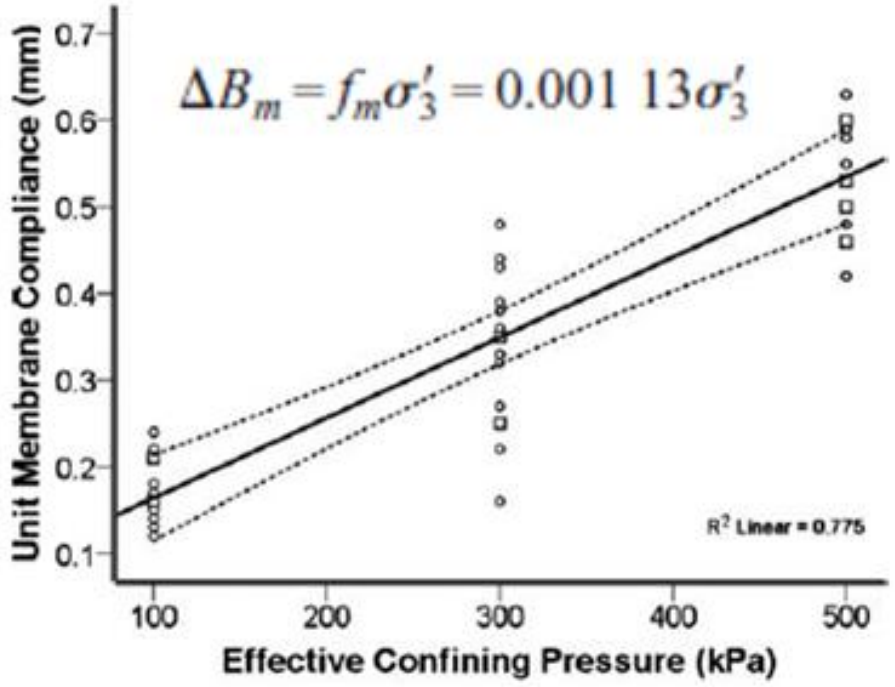

Figure 2.8 Effect of unit membrane compliance on effective confining pressure (Haeri and Shakeri 2010).

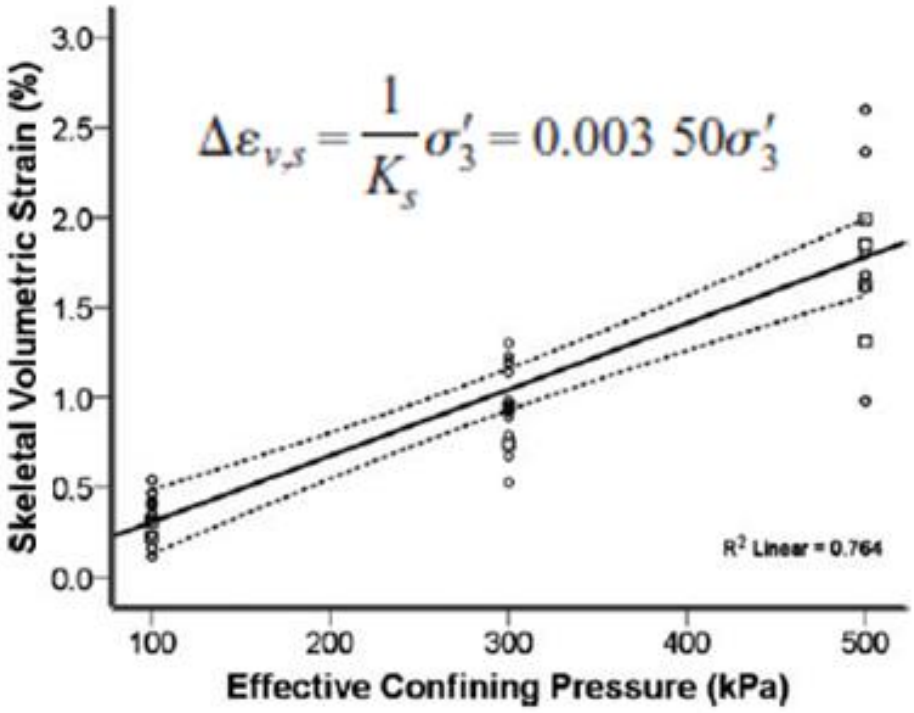

Figure 2.9 Effect of skeletal volumetric strain on effective confining pressure (Haeri and Shakeri 2010).

Haeri and Shakeri (2010) investigated the cyclic behaviors of granular material by comparing both methods for minimizing the membrane compliant effect. The comparison of the r_u between the samples with and without effect of membrane compliant is presented in Figure 2.10. It was found that the sample with the membrane compliant effect requires more cycles to cause liquefaction. In comparison with the normalized number of circles (N/N_L) as seen in Figure 2.11, the effect of membrane compliant causes a significant change in the pore pressure development. However, both the correction and coating techniques can minimize the effect of membrane compliance, as the r_u values obtained from the samples used for both techniques followed the same trend.

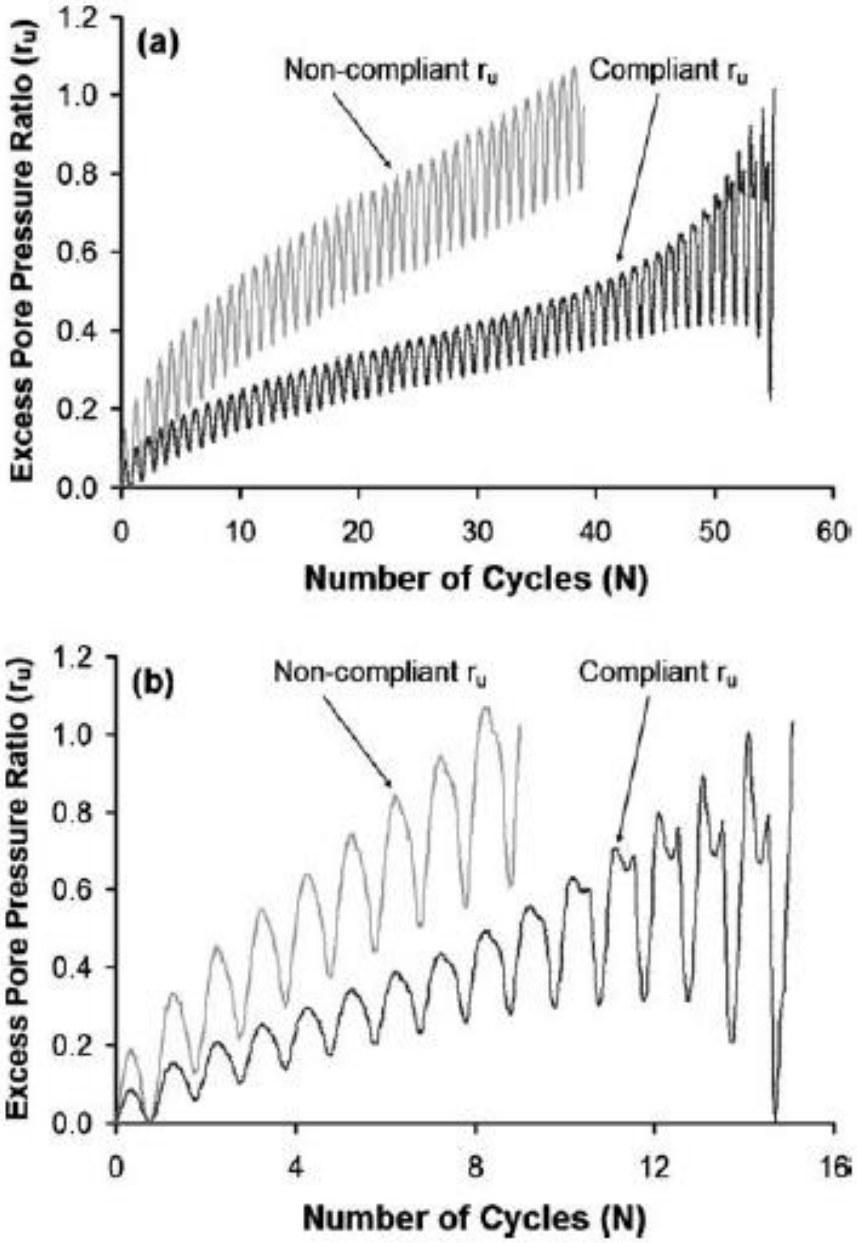

Figure 2.10 The effect of membrane compliance on the excess pore water pressure ratio at effective confining stress of 300 kPa and cyclic loading stress of (a) 125 kPa and (b) 150 kPa (Haeri and Shakeri 2010).

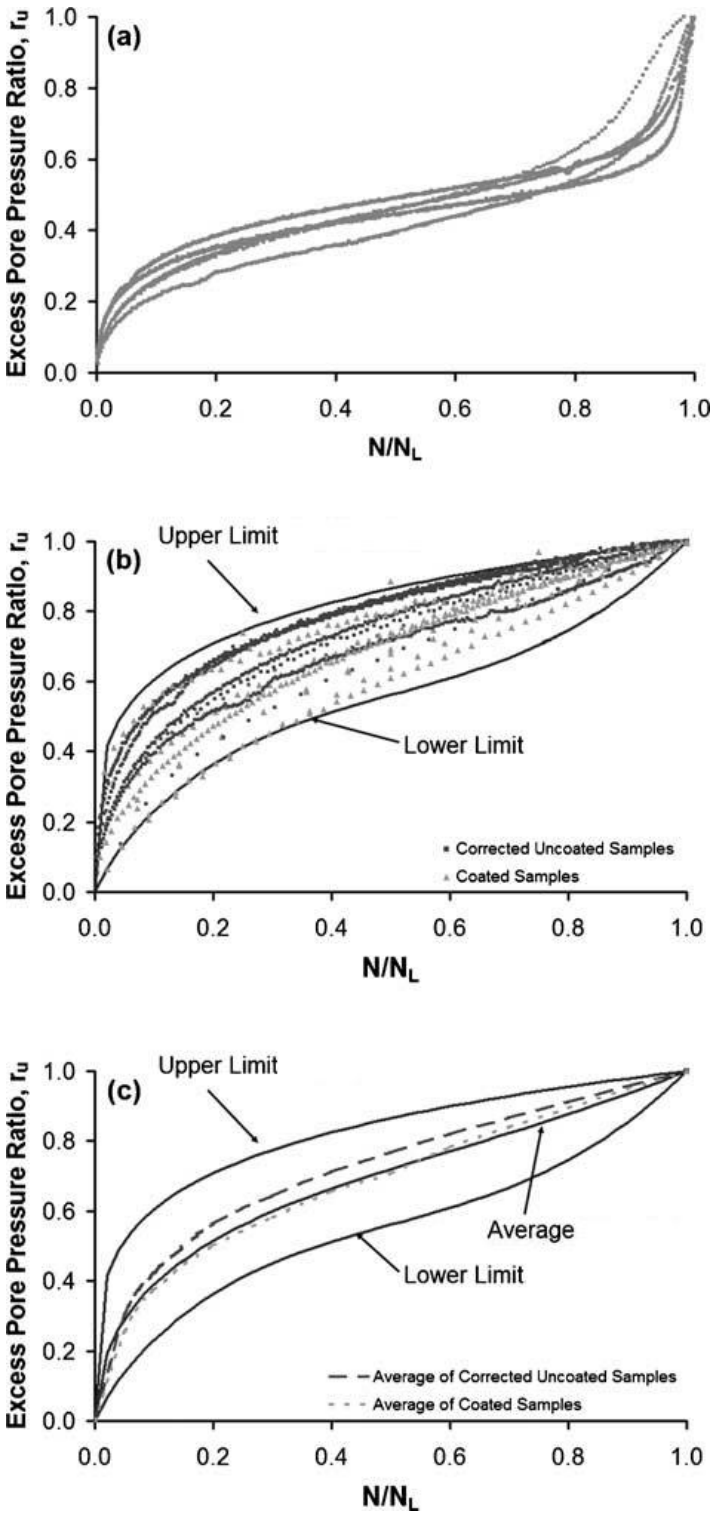

Figure 2.11 Excess pore water pressure ratio with the normalized number of circles for: (a) uncoated specimen, (b) membrane corrected system, and (c) comparison (Haeri and Shakeri 2010).

2.6 Monotonic and Post-Cyclic Behavior

Yasuda and Matsumoto (1994) investigated the relationship between monotonic and post-cyclic loading condition using the CIU triaxial tests of rockfill materials at the same initial condition and found that monotonic loading tests exhibit a greater reduction in shear modulus with an increase in shear strain. Holtz and Ellis (1961) studied the monotonic loading behavior of gravelly soils and found that the Mohr-Coulomb failure envelop of sandy gravels is nonlinear because of the particle interlocking, however no such impact was observed for clayey gravels, which behaved more like clayey soils. Hubler et al. (2017) found that the post-cyclic shear strength increases as either particle size, angularity, or relative density increases. Moreover, the monotonic and post-cyclic strength characteristics are equivalent when soil has similar relative densities. (See in Figure 2.12).

The stress behavior can be described as three phases for monotonic and post-cyclic behavior, as presented in Figure 2.13. For the first phase, the shear strength rapidly increases at the beginning of the monotonic loading test, while the specimen has nearly zero strength for the post-cyclic loading test. For the second phase, the specimen's shear modulus increases until it reaches a constant modulus in the third stage. For the second and third stage, shear modulus is identical for both monotonic and post-cyclic loading tests. In addition, the comparison of the cyclic stress path with peak, phase transform, and ultimate shear strength is presented in Figure 2.14 (b). These types of shear strength are defined in Figure 2.14 (a). Once the phase transition line was crossed, it was observed that the soil behavior switches from contractive behavior to dilative behavior under cyclic loading condition However, the ultimate friction angle represents the angle of failure line under static loading condition. As a result, the stress path under the cyclic loading could not cross

the ultimate strength line, but the stress reversal might appear once the stress path reached this line.

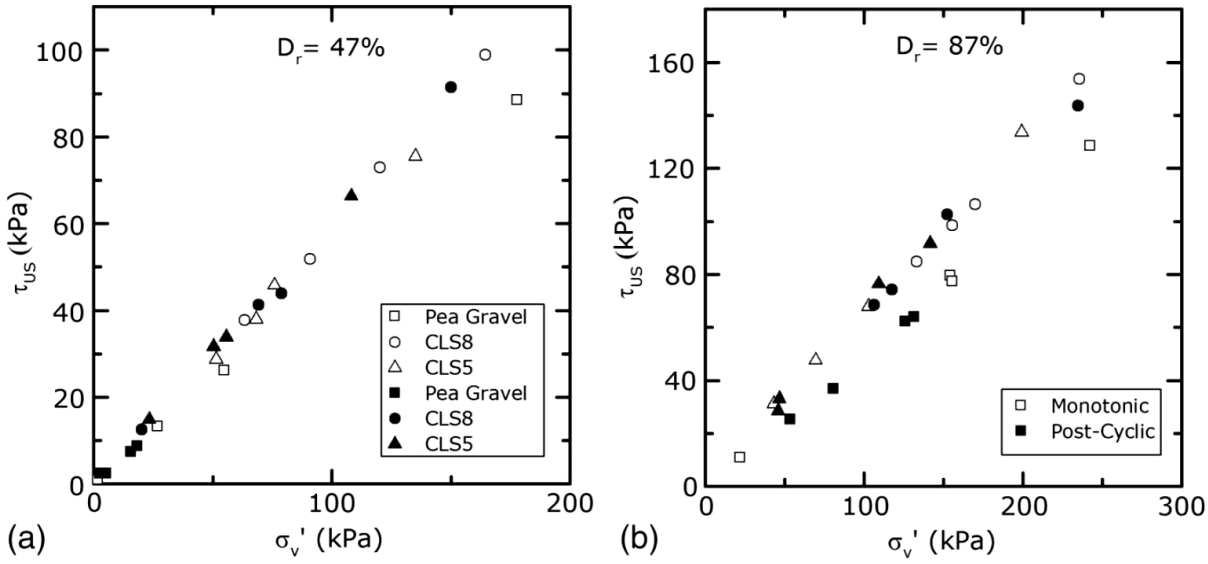

Figure 2.12 The ultimate shear strength for monotonic and post-cyclic loading tests of uniform gravels at: (a) relative density of 47%, and (b) relative density of 87% (Hubler et al. 2017).

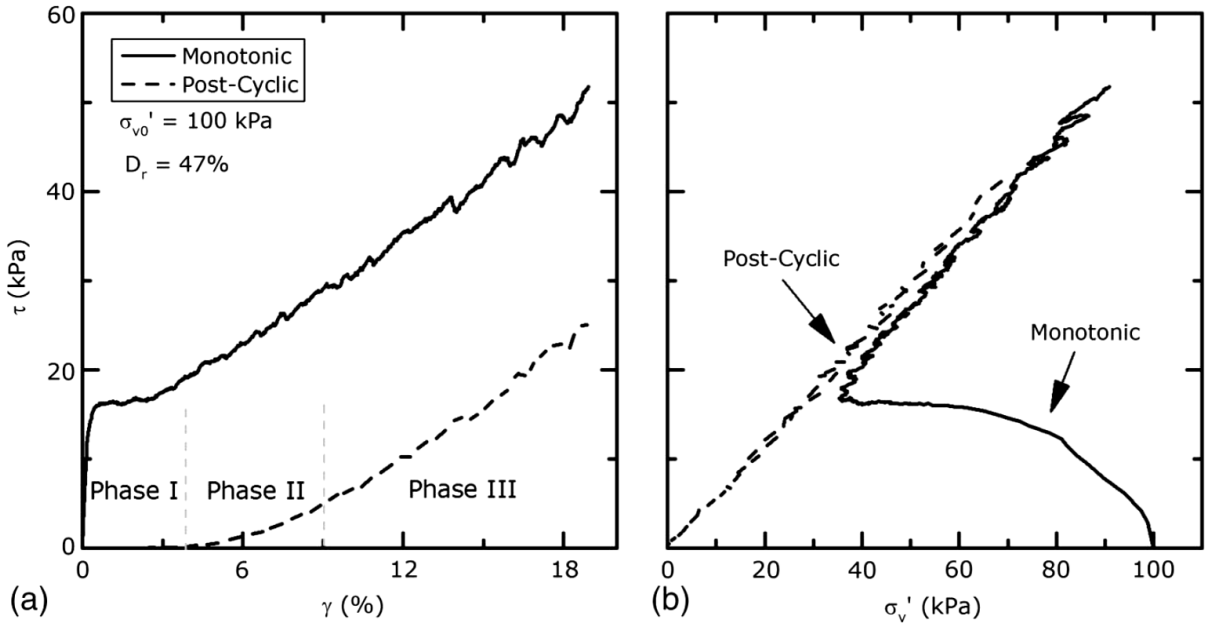

Figure 2.13 Comparison between monotonic and post-cyclic loading tests in: (a) stress-strain behavior, and (b) stress path (Hubler et al. 2017).

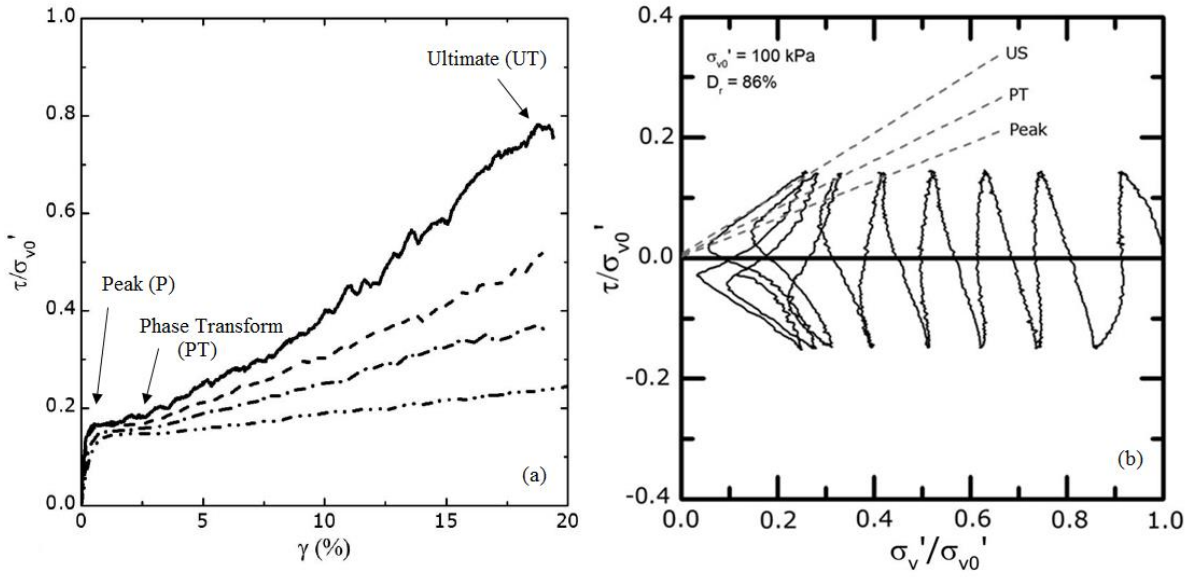

Figure 2.14 Comparison of (a) the different strength behaviors, and (b) the cyclic behavior with different shear strength of the gravelly soil (Hubler et al. 2017).

2.7 Dynamic Centrifuge Modeling

Geotechnical centrifuge modeling is an advanced physical modeling technique to evaluate prototype behaviors of small-scale models. Under centrifugal acceleration, the model is subjected to a geostatic stress condition equivalent to the field condition. A centrifuge shaker is utilized to apply shaking at the base of the model to simulate cyclic loading, dynamic loading, or earthquake loading. For the liquefaction study, a stacked-ring laminar container is one of the most common types of containers used to accommodate a centrifuge model as it allows large lateral soil deformation simulating an infinite ground and minimizing the boundary condition effects. Lee et al. (2010) suggested that the accelerometer and pore water pressure sensors should be located at a distance more than one-twentieth and one-fourth of the model length from the end walls of the model container, respectively.

2.7.1 Scaling Laws

The centrifuge's rotational spinning generates gravitational acceleration, N times ($N = a_{model} / a_{prototype}$) Earth's gravity. The model and the prototype stress conditions are similar (see in Figure 2.15) due to its the self-weight of the soils according to the fundamental scaling laws (e.g., Cargill and Ko 1983, Ko 1988, Joseph et al. 1988, Santamarina and Goodings 1989, Kutter 1995, Garnier et al. 2007, Taylor 2018). A summary of scaling laws relevant to the dimension, mass, and time is presented in Table 2.3. The centrifuge modeling technique is widely recognized as more advanced than other laboratory testing methods. Several limitations of the centrifuge technique were addressed by Kagawa et al. (2004) such as issues related to grain size, boundary effects, pore fluid velocity, variation of acceleration, and model size.

For example, the small size of the model cannot replicate the actual mechanism of soil behaviors because of boundary effect on the sensors' location in the model. Kagawa et al. (2004) studied the response of soil behaviors in the soil-pile-structure system using both centrifuge modeling and the large-scale shaking table. They found that amplification of response in the sand layer in the centrifuge modeling was lower than the response observed in the large-scale shaking table. The excess pore-water pressure in the liquefied sand layer for both methods generated and dissipated differently since the centrifuge model might experience a larger acceleration than the shaking table model. Moreover, the displacement observed in the centrifuge model was higher than that in the large-scale shaking table due to higher frequencies existing in the centrifuge model.

Despite the several limitations of centrifuge modeling, the technique has proven to be a power tool for geotechnical engineering research as it can provide valuable data to validate numerical model. Numerous liquefaction research studies have been conducted to date (e.g., Kutter et al. 1991, Kutter 1992, Elgamal et al. 1996 and 2005, Brennan et al. 2005, Garnier et al. 2007, Kutter et al. 2018 Antonaki et al. 2018, Manandhar et al. 2021).

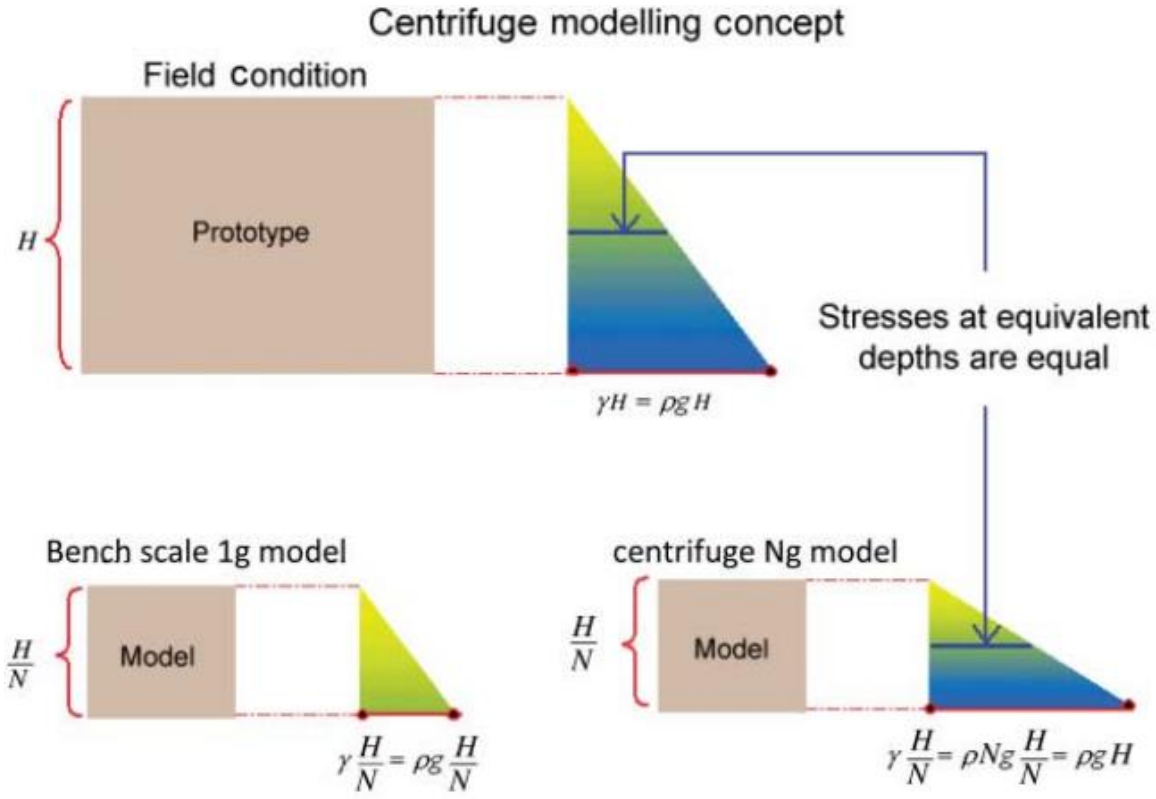

Figure 2.15 Vertical stress condition between prototype and model without/with gravitational acceleration.

Table 2.3 Scaling factors for geotechnical centrifuge modeling (Ko 1988, Ye et al. 2018).

Quality	Model	Prototype
Length	1	N
Area	1	N^2
Volume	1	N^3
Displacement	1	N
Velocity	1	1
Acceleration	1	1/N
Mass	1	N^3
Stress	1	1
Strain	1	1
Time (dynamic)	1	N
Time (consolidation)	1	N^2
Density	1	1
Cohesion	1	1
Friction angle	1	1

2.7.2 Diffusion Time in Centrifuge Modeling

Based on Table 2.3, the scale factor for consolidation time conflicts with the dynamic time when performing the dynamic centrifuge model test. Two techniques have been proposed to minimize conflict. The first technique utilizes the viscous pore fluid mechanism to scale up the velocity of the water flow (N times higher than water) by mixing the hydroxypropyl methylcellulose (or Methyl Cellulose) with water (Kimura 1993, Ko 1994, Chou et al. 2011); however, the solution may clog on the fine particles smaller than 0.075 mm (Kutter 1995). The second technique is practically applicable by using regular water since the soil permeability increases slightly in centrifuge models (Antonaki et al. 2018). In this technique, the rate of consolidation can be scaled by reducing soil particle size; however, it has some argument in the mechanical properties: Young's modulus,

friction angle, and stress ratio to cause liquefaction (Kutter 1995). Kutter (1995) states that stress and the number of interparticle contacts per unit area may have effects on the interparticle contact forces; both are dependent on the absolute particle size, not the scaled particle size without the effect of gravity force. As a result, if the model and prototype utilize the same soil, the interparticle contact force should be the same. Hence, the use of viscous pore fluid is preferable for the dynamic centrifuge test.

Adamidis and Madabhushi (2015) provided the derivation for time scale factors used for centrifuge test. If water is used in the centrifuge test, the permeability of the soil increases by n times higher than the prototype condition as presented in the following equations.

$$a = L/t^2 \qquad \text{Eqn. 2.12}$$

$$t_m = \sqrt{\frac{L_m}{a_m}} = \sqrt{\frac{L_p/n}{a_p\, n}} = \frac{t_p}{n} \qquad \text{Eqn. 2.13}$$

where *a* is acceleration; *L* is length; *t* is dynamic time while *m* and *p* represent model and prototype scale, respectively. The diffusion time (T_v) can be derived by the following equation.

$$T_v = C_v\,(t/d^2) \qquad \text{Eqn. 2.14}$$

Where $T_{v,m} = T_{v,p}$ for dimensionless time factor, and $C_{v,m} = C_{v,p}$ for the same soil and same water, and the *t* in Eqn. 2.14 -2.18 represents the diffusion time.

$$\frac{t_m}{d_m^2} = \frac{t_p}{d_p^2} \qquad \text{Eqn. 2.15}$$

$$t_m = \frac{t_p}{n^2} \qquad \text{Eqn. 2.16}$$

Where C_v is coefficient of consolidation, t is diffusion time, and d is distance. The conflict of time can be resolved by scaling down C_v and increasing viscosity of fluid (μ) by n time.

$$C_v = \frac{k}{m_v \rho_f g} \quad \text{and} \quad k = \frac{K_s \rho_f g}{\mu} \qquad \text{Eqn. 2.17}$$

$$t_m = \frac{t_p}{n} \quad \text{when} \quad \mu_m = \mu_p n \qquad \text{Eqn. 2.18}$$

where, k is permeability, m_v is compressibility of soil, K_s is intrinsic permeability, ρ_f is pore fluid density, and g is acceleration.

2.7.3 Preparation of Viscous Fluid in Centrifuge Modeling

Hydroxypropyl methylcellulose (HPMC) is used to increase viscosity of pore fluid in centrifuge modelling (Stewart et al. 1998, Dewoolkar et al. 1999, Chian and Madabhushi 2010, Adamidis and Madabhushi 2015, Antonaki et al. 2018, Manandhar et al. 2021). This method is beneficial without any change in soil grain sizes since the permeability is the same as prototype condition. For example, the Methocel F50 food gradient manufactured by the Dow Chemical company was suggested to be used as aquatic solution. The viscosity of 50 mPa·s can be achieved at 20°C with 2% concentration (Dow 2002). Notably, the viscosity used in the centrifuge modeling is dependent on the g-level. Previous studies used the scaling factor of N for the viscosity of the fluid (e.g., Stewart et al. 1998, Adamidis and Madabhushi 2015, Carey et al. 2020). Two preparation methods were proposed to make the viscous fluid: 1) surface hydration, and 2) hot/cold technique. It was found that both methods are effective in developing viscosity of the aquatic solution (Stewart et al. 1998).

However, the surface hydration method is preferable because it is simpler despite requiring more preparation time. Figure 2.16 can indicate that the viscosity of the solution increases as concentration increases and temperature decreases. However, different trends presented in Figure 2.16 (a) were dependent on the formulation of the HPMC which was changed after 1998. According to the Dow Chemical company, for a constant concentration, the viscosity of the viscous fluid should not change within a period of 30 days. Care should be taken if using a new batch of Methocel as the formula might be different.

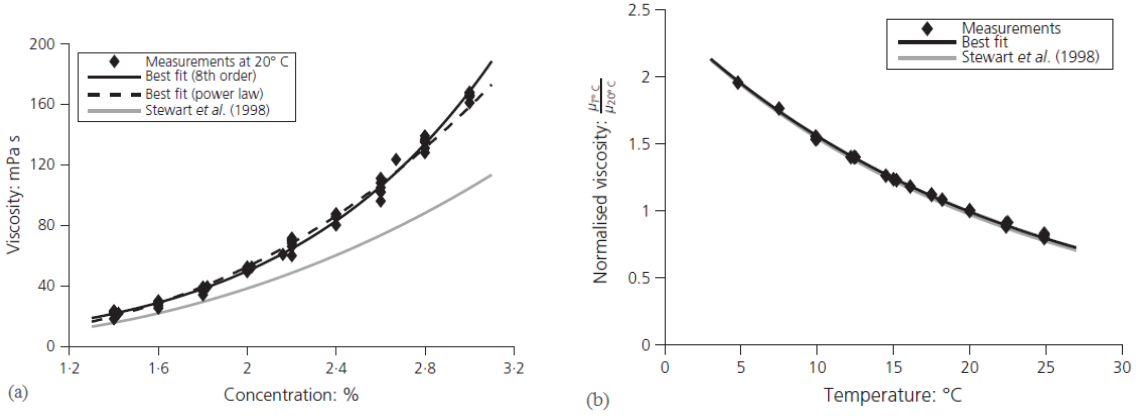

Figure 2.16 Change in viscosity of aquatic solution with (a) concentration at 20°C, and (b) temperature (Adamidis and Madabhushi 2015).

2.7.4 Data Analysis in Centrifuge Modeling

2.7.4.1 Filtering Acceleration Time History Data

Brennan et al. (2005) proposed a method for filtering raw data in order to eliminate vibration noise occurring at high frequencies and drift errors at low frequencies. Figure 2.17 shows the Fourier spectra of unfiltered compared with filtered data. Significant harmonics (see in Figure 2.17(c)) occurred at 150, 250, and 350 Hz while the main loading frequency was at 50 Hz in unfiltered data. The over filtered data (see in Figure 2.17(d))

represents a span of frequencies covering the loading frequencies applied to the model by the shaker. It is noted that additional vibration occurs in the centrifuge shaker system and is considered as part of the loading frequencies. The higher amplitude of acceleration (see in Figure 2.17(a)) was observed in the unfiltered data due to the integration of other vibrations at higher harmonics of the main loading frequency, not noise of the signal (Brennan et al. 2005). That led to an overestimated shear strain and additional uncertainties in the calculation of shear modulus and damping ratio. However, the stiffness and damping obtained from the filtered centrifuge data was more reliable than the unfiltered data when compared to the results of laboratory tests (Brennan et al. 2005).

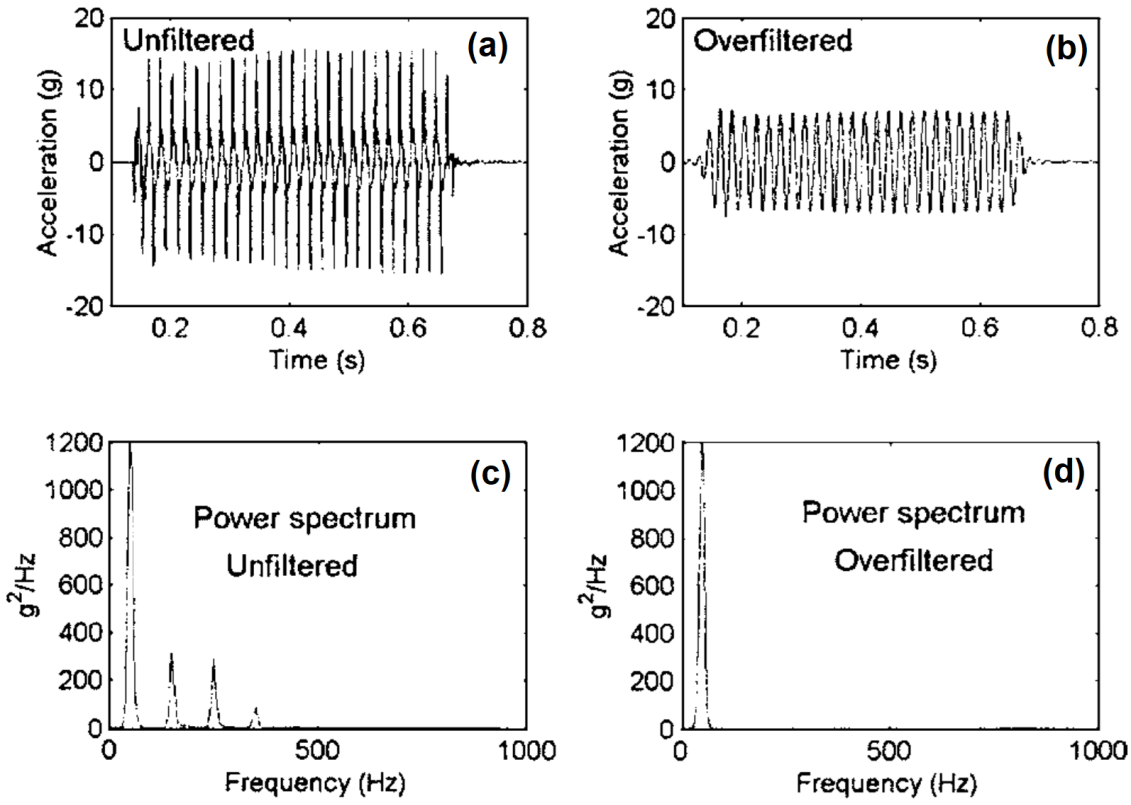

Figure 2.17 Effect of filtered acceleration-time response with Fourier spectra (Brennan et al. 2005).

2.7.4.2 Model Response in Frequency Domain

Manandhar et al. (2021) studied liquefaction evaluation of Ottawa F-65 sand in centrifuge tests. The work was part of the liquefaction experiment and analysis projects (LEAP) which was an international collaboration on liquefaction behavior of soils. The dense and medium-dense sand models prepared in the centrifuge were spun up to 40-g centrifugal acceleration. Both models were subjected to a 1 Hz sinusoidal base motion at a PGA of 0.15 g. The 5^{th} order Butterworth filter with cut-off band-pass frequency between 0.2 and 25 Hz was suggested to analyze displacement time histories. Fast Fourier Transform (FFT) of the motions at the base and top soil layer are presented in Figure 2.18. It was found that the amplitude of soil response at frequency of 1 Hz in the dense model follows the amplitude of base motion; however, the softening effect in the medium-dense model causes the amplitude of soil response at 1 Hz to not follow the amplitude of base motion. The shift in frequency to the lower frequency was captured in the fully liquefied soil layer. It was mentioned that the s wave is not able to propagate through the fully liquefied soils leading to the decrease in Fourier amplitude to near zero. In addition, the response showing at frequencies between 1 Hz and fundamental frequency (f_n) were influenced by the increasing r_u while the r_u greater than 0.9 (Kramer et al. 2016). Moreover, the dilative behavior of sand was observed as negative spikes in the acceleration time histories at frequencies higher than 10 Hz.

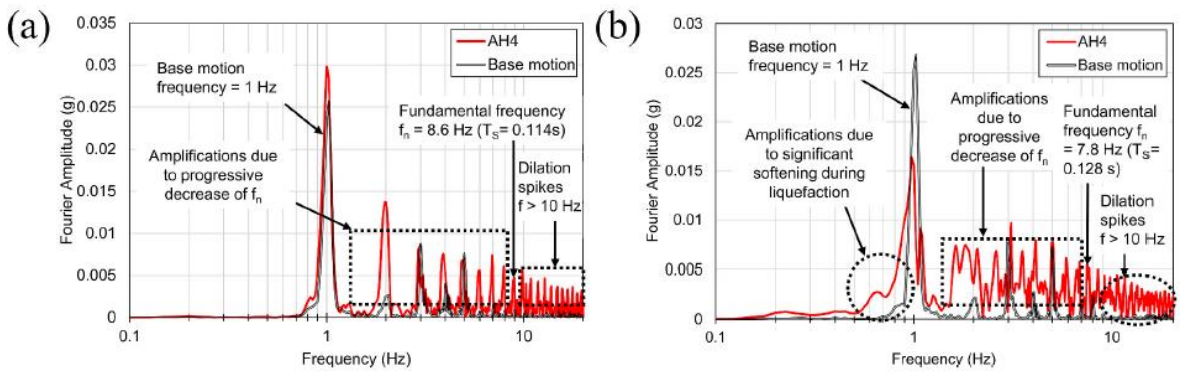

Figure 2.18 Fast Fourier Transform (FFT) of base motion and topsoil motion for (a) dense model and (b) medium-dense model (Manandhar et al. 2021).

2.7.4.3 Pore Pressure Behaviors during Shaking

The responses of pore water pressure behaviors along the soil profile are unique data obtained in centrifuge modeling that is closely related to the field condition. It can be used to indicate the soil liquefaction at each specific depth under the shaking condition. An example of typical pore pressure behaviors in centrifuge modeling are presented in Figure 2.19. Two models were prepared using Ottawa F-65 sand in dense and medium dense stage by Manandhar et al. (2021). Based on the excess pore pressure ratio (r_u) behaviors, the r_u increased immediately within the first few cycles after the beginning of shaking, and the rate of increasing r_u was lower until reaching the maximum r_u. The higher r_u was typically observed at the lower effective stress (or depth). The maximum amplitude of the r_u is dependent on the relative density of the sand. At top 3 m, the medium-dense sand model had the r_u higher than 1, that can indicate an occurrence of full liquefaction. In the centrifuge modelling, it is general to find the r_u higher than 1 due to in-stability of effective vertical stress during full liquefaction (e.g., Kutter et al. 2020, Hughes and Madabhushi 2018, Zhou et al. 2018, Carey et al. 2018, Tobita et al. 2018). In addition, Seed et al.

(1975) described that the initial liquefaction with limited stain potential could occur at an r_u of approximately 0.8. As a result, the initial liquefaction would be involved at the top 3 m in the dense sand model based on Figure 2.19 (a). However, both models at depth deeper than 4 m are not susceptible to liquefaction due to the maximum r_u is less than 0.8. Therefore, the denser sand had lower liquefaction susceptibility.

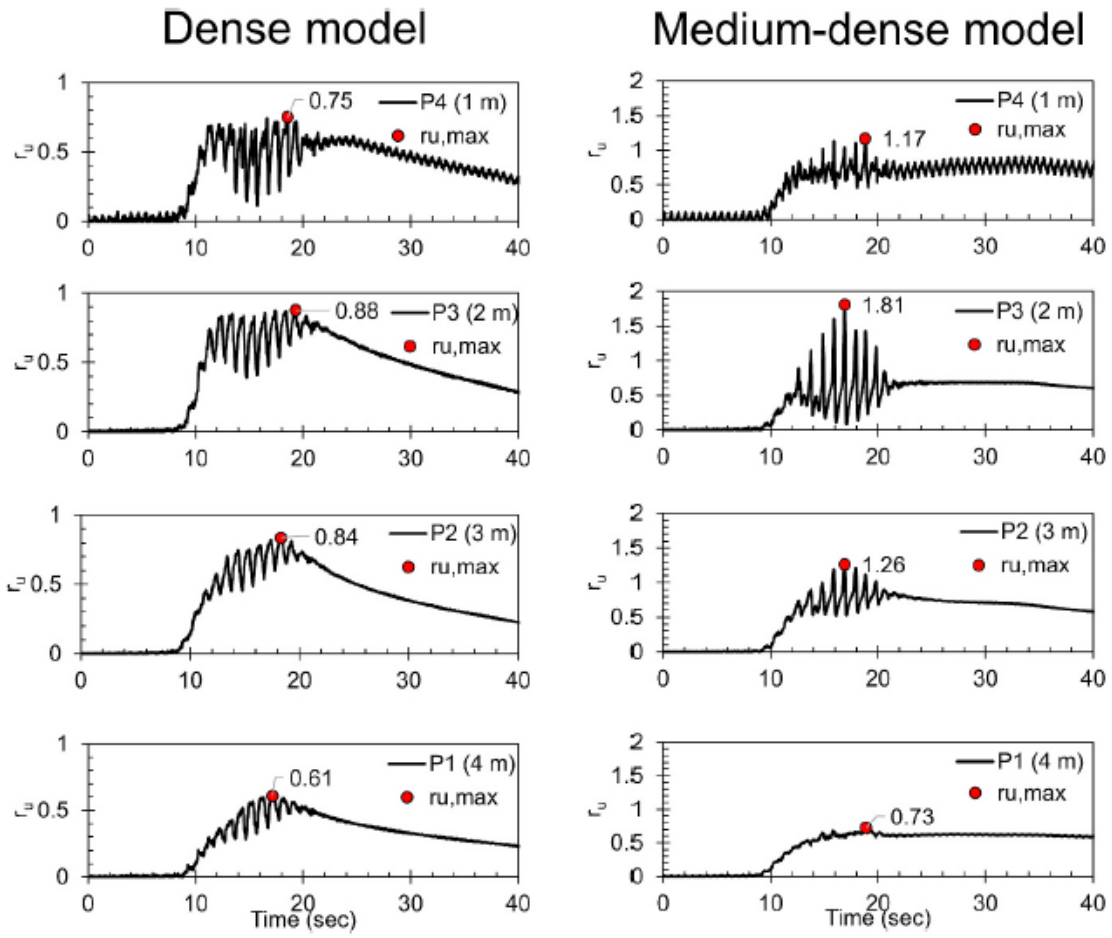

Figure 2.19 Pore pressure ratios (r_u) and maximum r_u ($r_{u,max}$) recorded at four different depths (P1 to P4) in dense models and medium-dense model. (Manandhar et al. 2021).

2.7.4.4 Dynamic Soil Characterizations in Centrifuge Modeling

The dynamic behaviors, including shear modulus and damping, can be evaluated by the response of the centrifuge model subjected to various shaking amplitudes. Those parameters are measured at higher shear strain level than that obtained from the resonant column and torsional shear tests. Strain levels generated in centrifuge model test may be comparable to the shear stain in cyclic triaxial test. Methods of data analysis applied to the centrifuge test results were described in detail by Ellis et al. (1998), Teymur and Madabhushi (2002), Pitilakis et al. (2004), and Brennan et al. (2005). The shear stress (τ) can be determined by the integration of density (ρ) multiplied by acceleration ($\ddot{u}$) as proposed by Zeghal and Elgamal (1994).

$$\tau(z) = \int_0^z \rho \ddot{u}\, dz \qquad \text{Eqn. 2.19}$$

$$\tau(z) = \frac{1}{2}\, \rho z\, (\, \ddot{u}(0) + \ddot{u}(z)\,) \qquad \text{Eqn. 2.20}$$

$$\tau(z_2) = \frac{1}{2}\, \rho\, \frac{[\, \ddot{u}_1 z_2^2 + \ddot{u}_2 z_2\, (\, z_2 - 2z_1)\,]}{[\, z_2 - z_1\,]} \qquad \text{Eqn. 2.21}$$

where z is the depth from the ground surface. The shear strain (γ) occurring at any depth can be approximately calculated from a relation of horizontal displacement (u) as:

$$\gamma = \frac{(u_2 - u_1)}{(z_2 - z_1)} \qquad \text{Eqn. 2.22}$$

Based on the calculated shear stress (τ) and shear strain (γ), a stress-strain loop (see Figure 2.20) can be developed. As a result, shear modulus (G) and damping ratio (D) can be determined using the following expressions.

$$G = \tau / \gamma \qquad \text{Eqn. 2.23}$$

$$D = \frac{1}{2\pi} \cdot \frac{W}{W_{elastic}} = \frac{1}{2\pi} \cdot \frac{\int \tau \, d\gamma}{(0.25 \cdot \Delta\tau \cdot \Delta\gamma)} \qquad \text{Eqn. 2.24}$$

Afacan et al. (2014) performed a set of centrifuge modeling to study the site response in soft clay. The shear modulus (G) reduction and damping (D) curves were developed from the stress-strain loop behaviors. Overestimated G and underestimated D were obtained at a low-strain dynamic range lower than 0.3%. However, the estimation of G and D at the shear strain higher than 0.3% is reliable in dynamic centrifuge modeling. The strain rate effect was found during the strong shaking due to the model subjected to the high frequency shaking, similar to findings by Kagawa et al. (2004). This effect might result in up to an approximately 40 percent increase in the shear resistance, which a calculated error relative to the prototype strain rate. However, the strain rate effect is more dominant in cohesive soils than cohesionless soils.

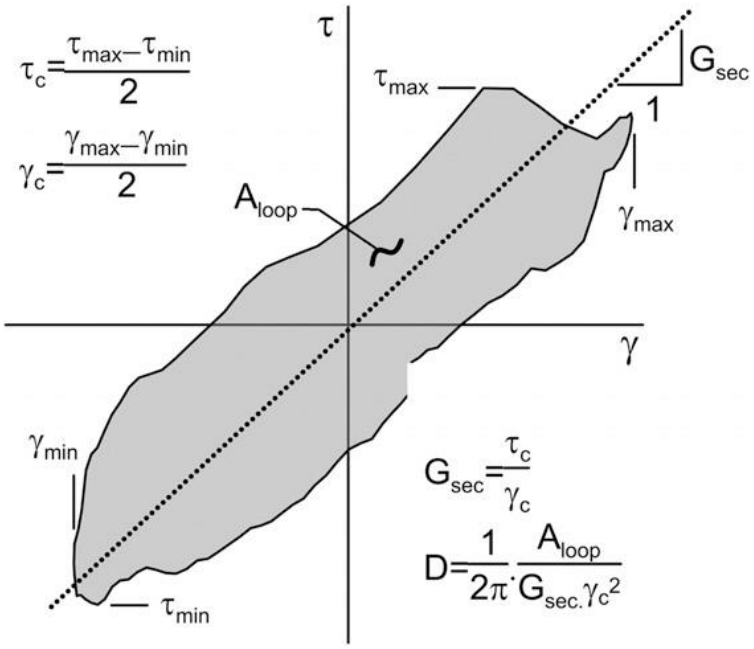

Figure 2.20 Nonsymmetrical stress-strain loop to estimate shear modulus and damping (Afacan et al. 2013).

2.7.4.5 Volumetric Strain due to Shaking

Okamura et al. (2019) investigated the pre-shaking effect on the volumetric strain and cyclic strength of sand using the centrifuge modeling tests in comparison with the cyclic triaxial tests. They found that liquefaction resistance increases as soil density increases and the degree of saturation decreases. The sample with the higher liquefaction resistance often exhibited the lowest volumetric strain due to the shaking. They also mentioned that the relative density and shear wave velocity were poor indicators to evaluate the liquefaction resistance because the change in these parameters are not noticeable during small pre-shaking. According to Sybico (1992), the excessive settlement induced from shaking may be influenced by partial drainage or dissipation behaviors, comparable to the deformation and strain behaviors observed during undrained shearing in cyclic triaxial tests (e.g., Okamura and Soga 2006, Kutter 1995, and Sybico 1992). After the liquefaction occurred in centrifuge modeling, the horizontal earth pressure coefficient (K_0), shear wave velocity (V_s), and liquefaction resistance tended to recover to the initial value before tests (Okamura et al. 2019).

2.7.5 A Summary Literature Review for Centrifuge Modeling to Evaluate Effect of Soil Composition on Liquefaction Behavior

Numerous case histories revealed that liquefaction can occur in gravelly soils (e.g., Coulter and Migliaccio 1966, Stokoe et al. 1988, Evan and Harder 1993, Kokusho et al. 1995), and catastrophic damages due to liquefaction of gravelly soils have been documented in several case histories (e.g., Andrus 1994, Harder and Stewart 1996, Yan and Lum 2003, Rico et al. 2008, Blight 2009, Cao et al. 2011, Rinehart et al. 2016).

However, the knowledge of cyclic behaviors relating to the gravel-sand-fines mixtures is limited, particularly in centrifuge modeling.

Recently, it was found that only a few research studies are relevant to the liquefaction behaviors of gravelly soils in centrifuge modeling. Among this is the work by Antonaki et al. (2018) to evaluate cyclic behavior of mine tailings and a mixture of tailings and waste rock materials using a centrifuge. The key considerations for the purpose of mixing mining materials, proposed by Wickland et al. (2006), are mixture ratio of waste rock materials and tailings, placement methods, and chemical compatibility. Four layers of the mixtures with 4% slope surface were prepared in a laminar container. Self-weight consolidation at 20 g was performed to prepare each soft soil layer, prior to the consolidation of the entire model at the target acceleration of 80 g. It should be noted that the rock particle was scaled down about 80 times, and water was used as pore fluid in this study. The models with higher rock content consolidated faster because of higher permeability and less pore pressure development as presented in Figure 2.21. It was also found that the shear wave velocity increases as gravel content increases, corresponding with an improvement in reinforcement and drainage of the soil mixtures. During the shaking, the liquefaction behavior was observed based on significantly decreasing in amplitude of soil acceleration and period elongation (frequency), as seen in Figure 2.22. The dilative behavior was observed as the pronounced spikes corresponding with the decrease in pore pressure (Antonaki et al. 2018, Zeghal et al. 1996, Zeghal and Elgama 1994). The mixture ratio of 2.3:1 (waste rock materials: tailings) was found to be the optimum mixture ratio, as tailings fully fill the rock voids. The performance of the 3:1

slope was satisfied with the earthquake amplitude up to 0.25 g and up to 0.10 g for the 2.4:1 slope.

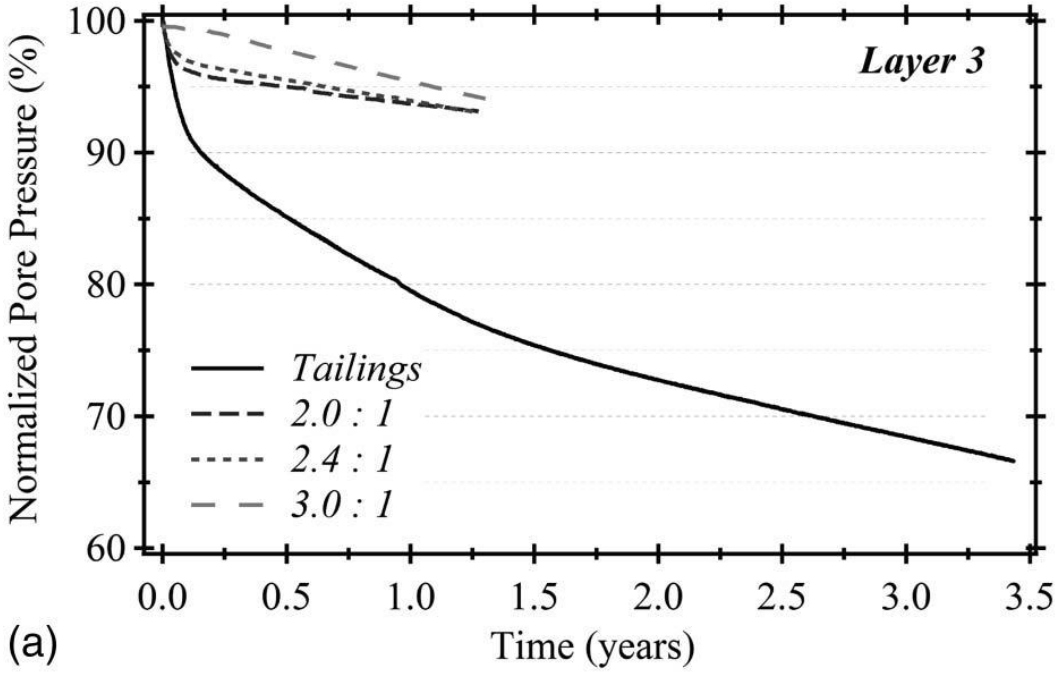

Figure 2.21 Normalized pore pressure with the initial pore pressure comparing with the consolidation time of various mining mixtures (Antonaki et al. 2018).

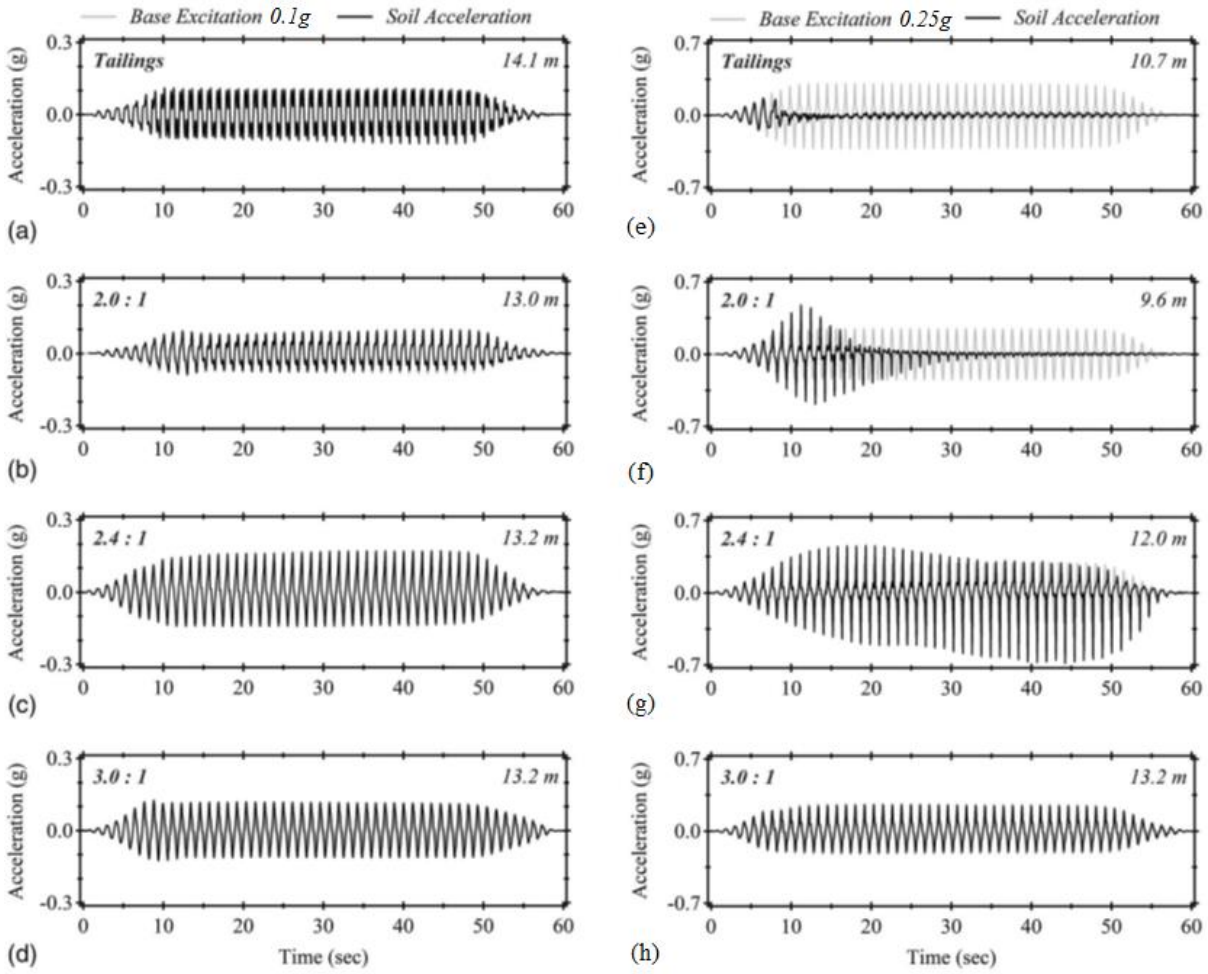

Figure 2.22 Soil acceleration response to the base excitation of 0.1 g and 0.25 g at various mixing ratio: (a and e) tailings; (b and f) 2:1 mixture; (c and g) 2.4:1 mixture; (d and h) 3:1 mixture, respectively (Antonaki et al. 2018).

CHAPTER 3

TOPIC 1: CYCLIC RESPONSE OF UNDISTURBED AND RECONSTITUTED GRAVELLY SOILS UNDER TRIAXIAL TESTING CONDITIONS[1]

[1] Ruttithivaphanich, P., & Sasanakul, I. (In preparation to be submitted to a journal paper).

3.1 Introduction and Motivation

Mine waste consisting of waste rock and tailings is the byproduct of mineral extraction. The focus of this study is mine waste rock, the waste material that is extracted and transported from mining pits and stored in mining facilities. Gradation of waste rocks are subject to change in a short period of time due to a chemical weathering. The material typically comprises a wide range of particle sizes including boulder, gravel, sand, and some fines with low plasticity. Mining operations accelerates chemical weathering of waste rock resulting in the change of gradation as well as unique soil structures that may not be easily replicated in a laboratory. While several researchers studied cyclic behaviors of reconstituted gravelly soil, waste rock material has not been extensively researched due to limitations related to large particle size, large sample size, and high-stress requirements.

To collect undisturbed waste rock materials, a large-diameter thin wall Shelby tube sampler is required for sampling and the maximum particle size of the sample cannot be larger than the gravel particle size. To perform laboratory testing, the grain size distribution may need to be adjusted further to reduce the overall particle sizes to meet the required standardized sample size and equipment capabilities. In this study, a series of stress-controlled cyclic triaxial (CTX) tests were performed on minimally disturbed samples of waste rock (containing gravel, sand, and fines) collected from a mine site using large thin wall Shelby samplers. The cyclic behaviors of the waste rock material (gravelly soils) were analyzed to evaluate the liquefaction susceptibility and compared with literature. Analyses were performed to evaluate several strength and stiffness parameters including the ultimate, phase transform, and post-cyclic friction angles, and high strain shear modulus. Based on

the results, the soil composition was analyzed to investigate the influence of soil structure matrix of the composite soils containing gravel, sand, and fines on liquefaction potential.

3.2 Sample Preparation and Testing Procedure

Cyclic and post-cyclic behaviors of undisturbed and reconstituted mine waste materials were evaluated using the cyclic triaxial (CTX) test. Mine waste materials comprised of gravel, sand, and low plasticity fines, were collected in thin wall Shelby tube with a dimension of 150 mm in diameter and 910 mm in length. The Shelby tubes were cut lengthwise as seen in Figure 3.1. The samples were carefully removed and trimmed to 100 mm in diameter and a 2:1 dimension ratio (length to diameter) for the CTX test to minimize the effect of the maximum particle size following the ASTM D4767-11. The specimen was placed above a set of porous stone and filter paper in the CTX device. A rubber membrane was then installed before close the CTX cell. The CTX test was conducted in accordance with ASTM D5311M-13. The specimen was flushed using de-aired water under a cell pressure of 30 kPa until the amount of water approximately 10 liters draining out of the sample prior to saturation. The flushing process time is dependent on the permeability of the specimen. The saturation process was then performed by increasing cell and back pressure simultaneously in a small increment to prevent prestressing the sample under an effective stress of approximately 35 kPa. The fully saturated sample is achieved when the B-value is greater than 0.95. The specimen was then consolidated at the target effective stress, until reaching the end of primary (EOP) consolidation. The stress-controlled cyclic loading test was performed under an undrained condition by applying 0.5-Hz sinusoidal loading frequency. It is noted that relatively low frequency was used to minimize the effect of membrane compliance that might appear in granular materials as suggested by Alhani

et al. (2018). Initial liquefaction was determined based on two criteria: pore pressure ratio of 0.95 or a double strain amplitude of 6%. If the sample did not liquefy, the cyclic test stopped at 500 cycles.

For the post-cyclic behavior, the undrained monotonic loading test was performed at a loading rate of 0.02% strain/min until the axial strain of 20% was reached. The slow loading rate was selected to minimize the effect of loading rate on pore pressure development based on ASTM D4767-11. The post-test investigation was performed after the monotonic loading test, regarding final water content, final density, and gradation.

In addition to the CTX tests, the consolidated isotopically drained triaxial (CIDTX) tests were performed on two reconstituted samples prepared to the same-sized specimen as in the CTX tests. The specimen preparation and consolidation procedures are the same as the CTX tests. For these tests, the shearing was performed until the 20% strain is reached in accordance with ASTM D7181-11.

Furthermore, the resonant column (RC) test was conducted on five samples. One sample was taken from the Shelby tube sampler and was trimmed to specific dimensions. The other four samples were reconstituted. The diameter of the undisturbed specimen was 71 mm, while the diameter of the four reconstituted specimens was 100 mm. All specimens have a 2:1 (length to diameter) dimension ratio. Each specimen was consolidated until the end of primary consolidation in accordance with Ruttithivaphanich and Sasanakul (2019), and the RC test was then performed according to ASTM D4015. The RC test was performed on each specimen at three confining pressures. For the first two confinements, the test was performed at a range of strains until the normalized shear modulus (G/G_{max})

of 0.8 was reached. For the last (highest) confinement, the test was performed until G/G_{max} of 0.5 was reached.

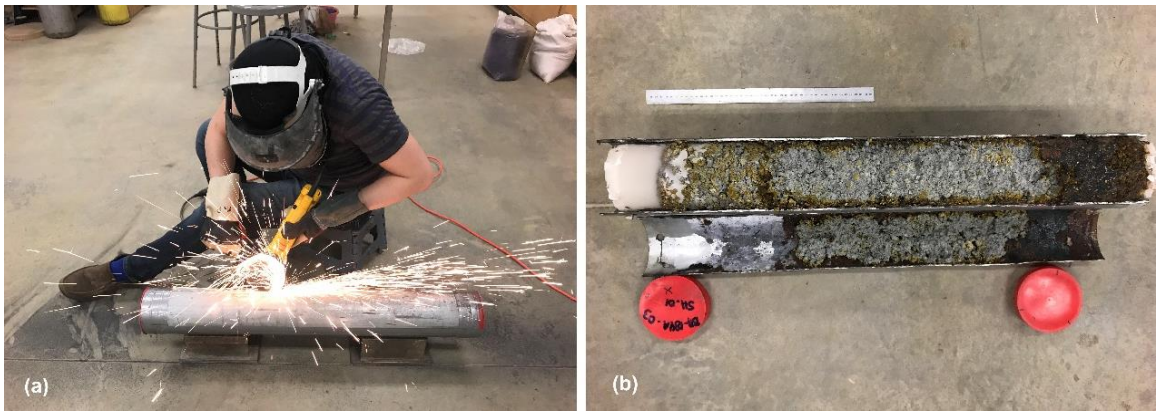

Figure 3.1 Lengthwise cut on Shelby tube (a) during cutting, and (b) after opening.

3.3 Material Properties

Table 3.1 presents index properties and soil composition of the samples tested in this study. Figure 3.2 summarizes the particle size distribution curves and indicates that all of the samples have comparable gradation, with exceptions for minor variations in gravel, sand, and fine content. It was observed that the entire gradation curves of these samples were not within the possibility of liquefaction, as proposed by Andrus and Stokoe (2000) and republished by Dobry et al. (2015). Most of the gravel particle size for the samples in this study was not considered liquefiable material, however the sand particle sizes have a possibility to liquefy. This observation indicated that the assessment of liquefaction for gravelly soils in this study should not be relied upon the grain size distribution only.

The correlations between the void ratio and each soil content are shown in Figure 3.3. The estimated curves for the maximum and minimum void ratios (e_{max} and e_{min}) were developed based on the reconstituted samples. It was found that most of the samples were in dense condition as the void ratio values were close to the e_{min} curve. Four undisturbed

samples were found to be denser than the maximum density, shown in Figure 3.3. This could be due to some difference in soil compositions between the undisturbed samples and the reconstituted samples for the development of the e_{min} curves. Interestingly, the relative density of a composite soil comprised of gravel, sand, and fines is very sensitive since a small change in the weight of any soil component can have a significant effect on the void ratio of the composite soil.

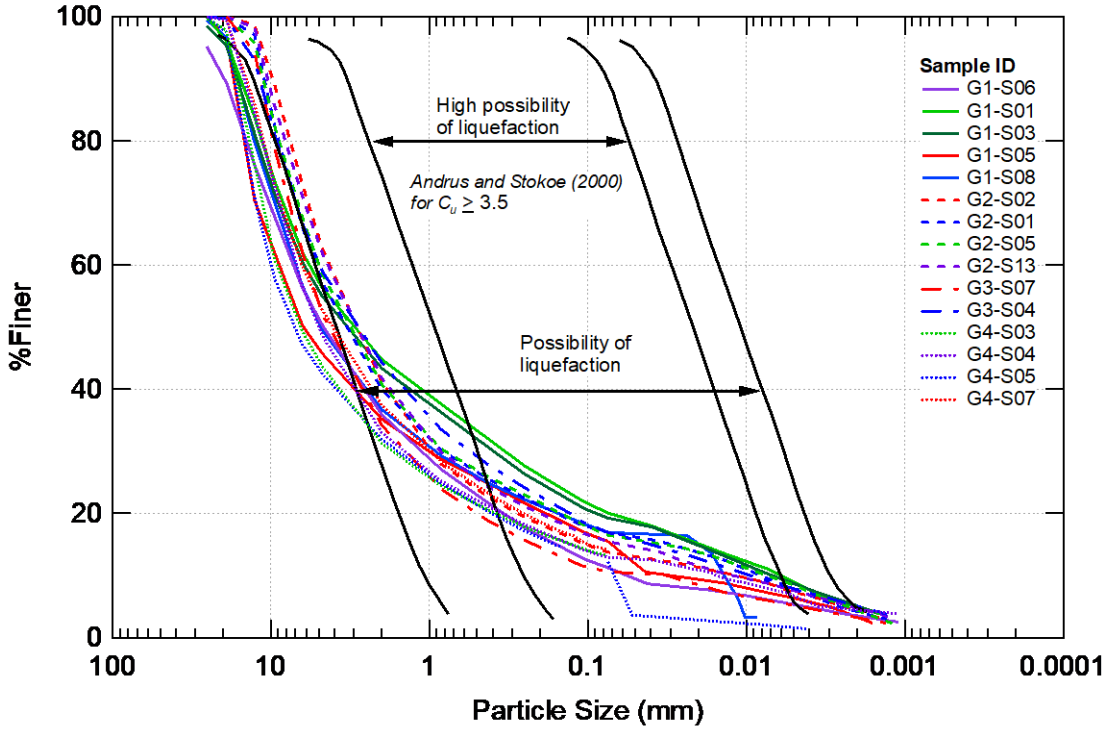

Figure 3.2 Grain size distribution curve for samples in this study.

Table 3.1 Index properties of the specimens used in Topic 2-1.

Sample number	Relative density	Specific gravity	Wet sieve / Dry sieve / Hydrometer					Atterberg limit		USCS	AASHTO	Gross Gs	Void ratio	Total unit weight (kN/m^3)
	C127	D854	D1140 / D6913 / D7928					D4318						
	$G_{s,\ gravel}$	$G_{s,\ sand\ and\ fines}$	%Gravel	%Sand	%Fine	Cu	Cc	LL	PI					
G1-Shelby6	2.75	2.77	49.65	39.05	11.30	116	2.4	26.3	7.1	GW-GC	A-2-6	2.76	0.33	21.40
G1-Shelby1	2.67	2.79	43.69	36.20	20.11	1000	2.8	27.0	10.0	GC	A-2-4	2.74	0.27	22.57
G1-Shelby3	2.75	2.81	45.05	35.66	19.29	854	3.8	27.7	19.0	GC	A-2-4	2.78	0.32	21.87
G1-Shelby5	2.72	2.86	54.20	30.30	15.50	346	3.9	27.6	10.7	GC	A-2-6	2.78	0.28	22.82
G1-Shelby8	2.70	2.72	43.41	40.10	16.49	423	9.9	30.0	12.0	GC	A-2-6	2.71	0.38	23.12
G2-Shelby2	2.74	2.65	37.33	48.89	13.78	420	19.3	26.5	7.1	SC	A-2-4	2.68	0.49	19.28
G2-Shelby1	2.67	2.79	42.80	40.21	16.99	638	17.7	25.0	7.7	GC	A-2-4	2.74	0.46	19.68
G2-Shelby5	2.74	2.72	41.45	42.01	16.54	676	19.5	23.9	6.1	SC-SM	A-2-4	2.73	0.46	19.69
G2-Shelby13	2.71	2.69	38.11	46.43	15.46	297	12.8	29.9	5.5	SM	A-1-b	2.70	0.39	20.26
G3-Shelby7	2.72	2.72	47.87	41.54	10.59	152	8.7	23.6	17.7	GP-GC & GP-GM	A-1-a	2.72	0.35	18.35
G3-Shelby4	2.74	2.69	41.01	42.00	16.99	490	5.1	27.2	10.0	SC	A-2-4	2.71	0.29	22.35
G4-Shelby4*	2.72	2.70	51.35	35.74	12.91	404	16.3	25.0	6.3	GC-GM	A-2-4	2.71	0.38	19.29
G4-Shelby3*	2.76	2.59	56.33	30.38	13.29	-	-	33.7	16.1	GC	A-2-6	2.69	0.41	19.29
G4-Shelby5*	2.74	2.69	57.47	30.30	12.23	147.1	3.8	26.5	9.7	GC	A-2-4	2.72	0.37	19.12
G4-Shelby7*	2.75	2.68	47.7	38.3	14.0	-	-	30	11	GC	A-2-6	2.71	0.34	19.12
GR-H10*	2.72	2.69	50.0	38.0	12.0	-	-	25.4	6.5	GC-GM	A-2-4	2.71	0.47	19.26

* Reconstituted sample

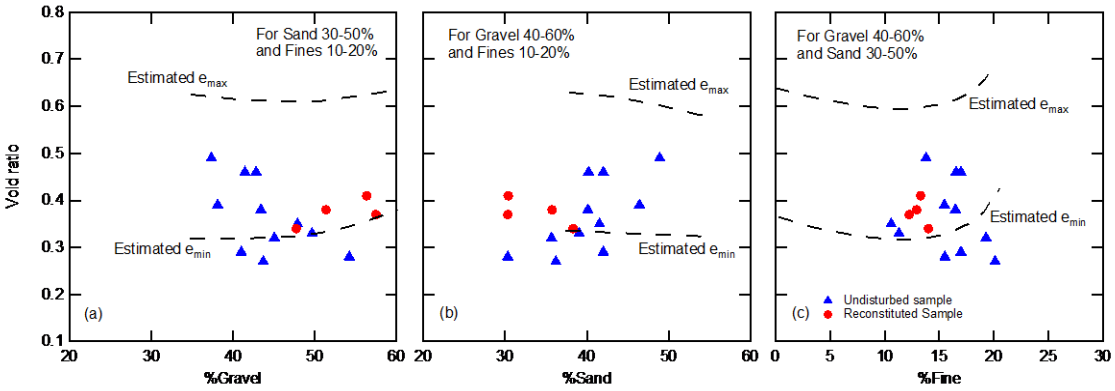

Figure 3.3 Correlation of void ratio with (a) gravel, (b) sand, and (c) fines contents.

3.4 Testing Program

Table 3.2 presents the testing program for all of the testing including CTX, RC, and CID-TX tests. The CTX tests were conducted on 42 specimens. The RC tests were performed on one undisturbed and four reconstituted samples. These reconstituted samples were prepared to have the same gradation as the field conditions and tested at the same effective stress as the CTX samples for G4-S3, G4-S4, G4-S5, and G4-S7. The RC test results were used to evaluate the shear modulus of the sample at low to medium strains. In addition, two CID-TX tests were conducted to evaluate monotonic loading behaviors and ultimate friction angle.

3.5 Results, Analysis and Discussion

According to the grain size distribution curves shown in Figure 3.2, the gradation of all samples in this study is comparable. A summary of cyclic triaxial results presents in Table 3.3, including the cyclic stress ratio (CSR), single amplitude strain (e_{sa}), and excess pore pressure ratio (r_u) at the number of cycles to cause liquefaction (N_L). All samples were liquefied at the CSR higher than 0.15, in exception to two specimens of the sample ID

G1S1. In addition, these specimens were performed at an effective confining stress (σ'_c) of 100 kPa and a cyclic stress ratio (CSR) of less than 0.2. It was obvious that the CSR was not high enough to trigger liquefaction, even though the cyclic loading was performed up to 500 cycles. It should be noted that the loading condition and effective stress do not entirely explain no liquefaction of these specimens. There are a few specimens liquified at the same loading condition and confinement. It is possible the reason is a combination of loading conditions and initial properties. The non-liquefied specimens were relatively denser and had relatively high fine content (approximately 20%). The cyclic behaviors of three specimens of Sample G2-S5 are presented in the subsection to represent the typical cyclic behaviors of the gravelly soils which liquefied during the cyclic loading. Additional subsections include strength and stiffness parameters, and liquefaction assessment of gravelly soils tested in this study.

Table 3.2 Testing program for undisturbed mine waste materials.

Sample number	Effective stress (kPa)	Lab ID number	CSR	G/G_{max}	Estimated $V_{s,1}$ (m/s)
G1-S6	325	CTX1	0.20	-	-
		CTX2	0.25	-	
		CTX3	0.28	-	
G1-S1	100	CTX1	0.15	-	-
		CTX2	0.20	-	
G1-S3	150	CTX1	0.25	-	-
		CTX2	0.20	-	
G1-S5	325	CTX1	0.30	-	-
		CTX2	0.20	-	
		CTX3	0.25	-	
G1-S8	325	CTX1	0.20	-	350.9
		CTX2	0.15	-	
	100	RC1	-	0.80	
	300		-	0.80	
	600		-	0.50	
G2-S2	100	CTX1	0.35	-	-
		CTX2	0.25	-	
		CTX3	0.30	-	
G2-S1	90	CTX1	0.30	-	-
		CTX2	0.25	-	
		CTX3	0.20	-	
G2-S5	180	CTX1	0.30	-	-
		CTX2	0.25	-	
		CTX3	0.20	-	
G2-S13	400	CTX1	0.20	-	-
		CTX2	0.25	-	
		CTX3	0.28	-	
G3-S7	300	CTX1	0.30	-	-
		CTX2	0.25	-	
		CTX3	0.20	-	
G3-S4	200	CTX1	0.20	-	-
		CTX2	0.25	-	
		CTX3	0.28	-	
G4-S4*	200	CTX1	0.30	-	317.8**
		CTX2	0.25	-	
		CTX3	0.15	-	
G4-S3*	120	CTX1	0.30	-	315.1**
		CTX2	0.25	-	
		CTX3	0.15	-	
G4-S5*	270	CTX1	0.30	-	296.0**
		CTX2	0.25	-	
		CTX3	0.15	-	
G4-S7*	350	CTX1	0.30	-	277.6**
		CTX2	0.25	-	
		CTX3	0.15	-	
GR-H10*	100	CIDTX	-	-	-
	350	CIDTX	-	-	

CTX = Cyclic triaxial test;
RC = Resonant column test;

CIDTX = Isotropically consolidated drained triaxial test;
[*] *reconstituted sample;*
[**] $V_{s,1}$ *estimated from beside borehole in the same location.*

Table 3.3 Summary of cyclic triaxial results

Sample number	Effective stress (kPa)	Lab ID number	CSR	N_L or $N_{ru=0.95}$	ε_{sa} (%)	ϕ'_{pt} (°)
G1-S6	325	CTX1	0.2	27	2.68	38.0
		CTX2	0.25	6	2.29	39.4
		CTX3	0.28	7	3.23	39.7
G1-S1	100	CTX1	0.15	>500	>1.60	-
		CTX2	0.2	>500	>4.10	-
G1-S3	150	CTX1	0.25	16	2.24	38.9
		CTX2	0.2	58	1.78	32.1
G1-S5	325	CTX1	0.3	4	2.19	41.6
		CTX2	0.2	16	3.08	39.4
		CTX3	0.25	6	2.33	40.7
G1-S8	325	CTX1	0.2	25	1.70	37.5
		CTX2	0.15	81	1.65	30.3
G2-S2	100	CTX1	0.35	6	2.19	30.3
		CTX2	0.25	86	2.30	33.4
		CTX3	0.3	88	2.15	33.5
G2-S1	90	CTX1	0.3	9	3.93	30.3
		CTX2	0.25	34	1.29	32.1
		CTX3	0.2	54	1.25	29.7
G2-S5	180	CTX1	0.3	4	6.78	37.4
		CTX2	0.25	30	1.77	38.4
		CTX3	0.2	247	0.51	37.5
G2-S13	400	CTX1	0.2	19	1.73	37.4
		CTX2	0.25	20	1.58	38.9
		CTX3	0.28	14	3.34	36.0
G3-S7	300	CTX1	0.3	3	2.75	30.2
		CTX2	0.25	26	3.46	29.2
		CTX3	0.2	26	1.64	33.0
G3-S4	200	CTX1	0.2	175	3.94	-
		CTX2	0.25	16	1.60	37.9
		CTX3	0.28	6	1.36	40.0
G4-S4*	200	CTX1	0.3	4	4.65	31.2
		CTX2	0.25	7	3.89	31.1
		CTX3	0.15	34	2.44	-
G4-S3*	120	CTX1	0.3	13	2.98	-
		CTX2	0.25	13	2.49	-
		CTX3	0.15	36	1.53	-
G4-S5*	270	CTX1	0.3	4	5.65	31.8
		CTX2	0.25	4	4.59	32.0
		CTX3	0.15	19	2.76	27.3
G4-S7*	350	CTX1	0.3	3	6.81	34.6
		CTX2	0.25	4	5.24	34.7
		CTX3	0.15	19	3.40	30.3
GR-H10*	100	CIDTX1	-	-	-	51.5**
	350	CIDTX2	-	-	-	

* *Reconstituted sample* ** *Ultimate friction angle*

3.5.1 Cyclic Behavior of Gravelly Soils

This section presents a sample of results for three tests conducted for Sample G2-S5 at three different cyclic stress ratios: 0.2, 0.25, and 0.3. The cyclic stress ratio (CSR), excess pore pressure ratio (r_u), and axial strain (ε) with the number of cycles are presented in Figure 3.4. Based on literature reviews (Seed and Lee 1966, Ishihara 1993, Vaid and Sivathayalan 1996, Sivathayalan 2000, Wu et al. 2004, Darcino et al. 2008, and Hubler et al. 2017), the r_u of 0.95 and double amplitude strain of 6% are the failure criteria due to liquefaction for gravelly soils. The stress-controlled CTX allows applying a constant CSR to the specimen at the beginning of the test, however a reduction in the CSR typically occurred as the specimen could no longer maintain the applied load as the strength and stiffness degradation occurred. This behavior was initially observed prior to the initiation of liquefaction when the r_u ranging from 0.75-0.85 (average value is 0.8) for all the samples tested in this study. The number of cycles when this behavior occurred depends mainly on the level of CSR. The reduction in CSR was more severe when the r_u higher than 0.95. It is noted that in some cases, the CSR might reduce immediately at the very first applied cycle. It led to the maximum amplitude of CSR not reaching the desired level. For the results shown in Figure 3.4, a significant reduction in CSR was observed at the 5^{th} cycle for the CSR of 0.3; however, the reduction of CSR was found in the tests with CSR of 0.2 and 0.25 at 258^{th} and 25^{th} cycles, respectively, as presented in Figure 3.4 (a). For the pore pressure development, the r_u developed immediately as soon as the loading started, and the r_u increased gradually with the number of cycles until it reached maximum value. The maximum r_u value depends on the loading amplitude (or level of CSR). As mentioned, the initial liquefaction was defined when the r_u reached 0.95. Similar to sand behavior, the

gravelly soils require less cycles to liquefy as the CSR increases. For the axial strain, the amplitude of the strain gradually increased with the number of cycles. The rate of increasing strain is higher at higher CSR. The strain amplitude for the gravelly soils is relatively low due to the impact of interlocking as discussed by Hubler et al. (2017). Previous studies found that for soil mixtures containing gravel content higher than 25% by weight, the gravel particles may exhibit high contact force (Do et al. 2016, Chang and Phantachang 2016, Chang and Hong 2008, Vallejo and Mawby 2000). Overall cyclic behaviors prior to initial liquefaction of all gravelly soils in this study, the axial strain slightly increased and continued until the r_u reached 0.95. The strain rapidly increased when the r_u higher than 0.95 while the double amplitude strain hardly exceeded 6%, before the r_u reached 0.95. It is noted that a few samples in this study exhibited the strain over 6% due to the high CSR. Figure 3.5 (b) shows the relationship between the r_u and the normalized number of cycles (N/N_L), as the rate of increasing r_u with N/N_L is not significantly different despite different CSRs. Based on the results of all tests, the failure of the gravelly soils was mostly a consequence of the pore pressure development.

During liquefaction ($r_u \geq 0.95$), it was observed that the pore water pressure remained constant while axial strain gradually increased with the number of cycles. However, the large flow-type deformation, in which the soil exhibits excessive strain development with number of cycles indicating that the soil behaves like fluid, was not observed in the gravelly soils. The observed behavior is comparable to dense gravelly soils reported by Hubler et al. (2017), and Youd et al. (2001). However, the large flow-type deformation was typically found in loose sand (e.g., Baziar and Dobry 1995, Cubrinovshi and Ishihara 2000, Yang and Pan 2017). In the case of a specimen undergoing a large flow-

type deformation, the specimen would exhibit a significant level of excessive strain at a stiffness near zero. It should be noted that the compression and extension loading conditions in the cyclic triaxial testing are the main causes of asymmetry strain behaviors since the compression and tensile strength of granular soils are significantly different. The tensile strain is greater than the compressive strain in the gravelly soils.

The relationship between the CSR and axial strain is described using the hysteretic stress-strain loop presented in Figure 3.6. The slope of the loop represents the stiffness of the material as Young's modulus (E) = stress (σ) / axial strain (ε). In each cycle, the positive amplitude of the CSR represents the behavior under the compression loading and the negative amplitude for the extension loading.

The axial strain due to compression was observed to be slightly less than the extension that is typically found in dense soil behavior. Also, asymmetrical loops are usually observed in cohesionless samples due to the asymmetrical strain behavior (e.g., Gerrard et al. 1972, Pyke 1978). During cyclic loading tests, the decrease in soil stiffness is anticipated due to granular particle rearrangement, leading to a significant decrease in the CSR. It was also found that the size of the hysteretic loop increases as the axial strain increases. This implies that there could be an increase in damping with strain. Moreover, the dilative behavior involved in the specimen before liquefaction occurred resulted in the distortion of the shear–strain loops, and the detorsion of the loop after the liquefaction occurred mainly since the excessive strain occurred while the reduction in CSR was also dominant in the specimen. Similar findings were observed in sands based on many literatures (e.g., Ishihara 1993, Vaid and Sivathayalan 1996, Sivathayalan 2000, Wu et al. 2004, Darcino et al. 2008, and Hubler et al. 2017).

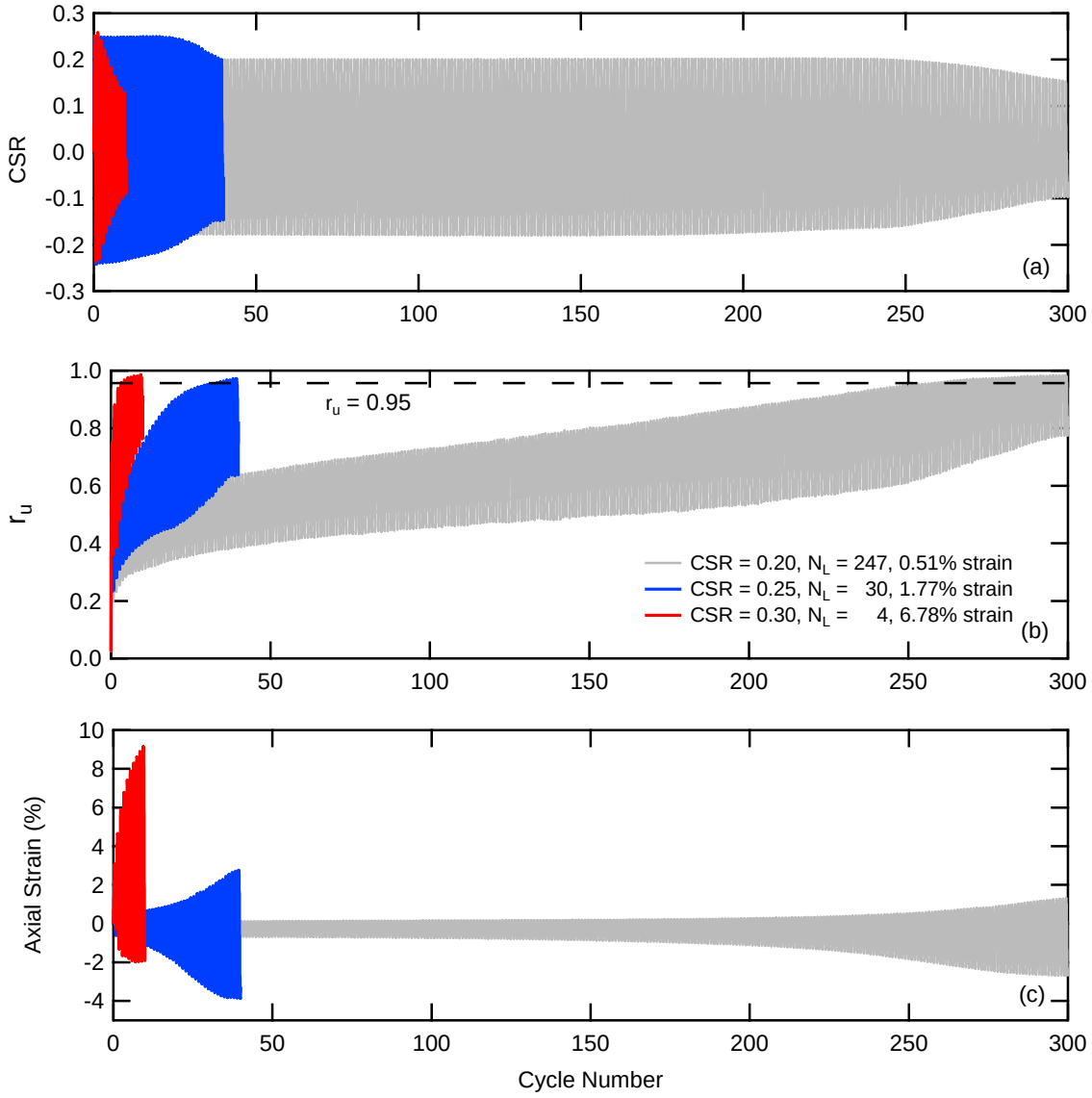

Figure 3.4 Cyclic responding behaviors on: a) cyclic stress ratio, b) pore water pressure ratio, and c) axial strain.

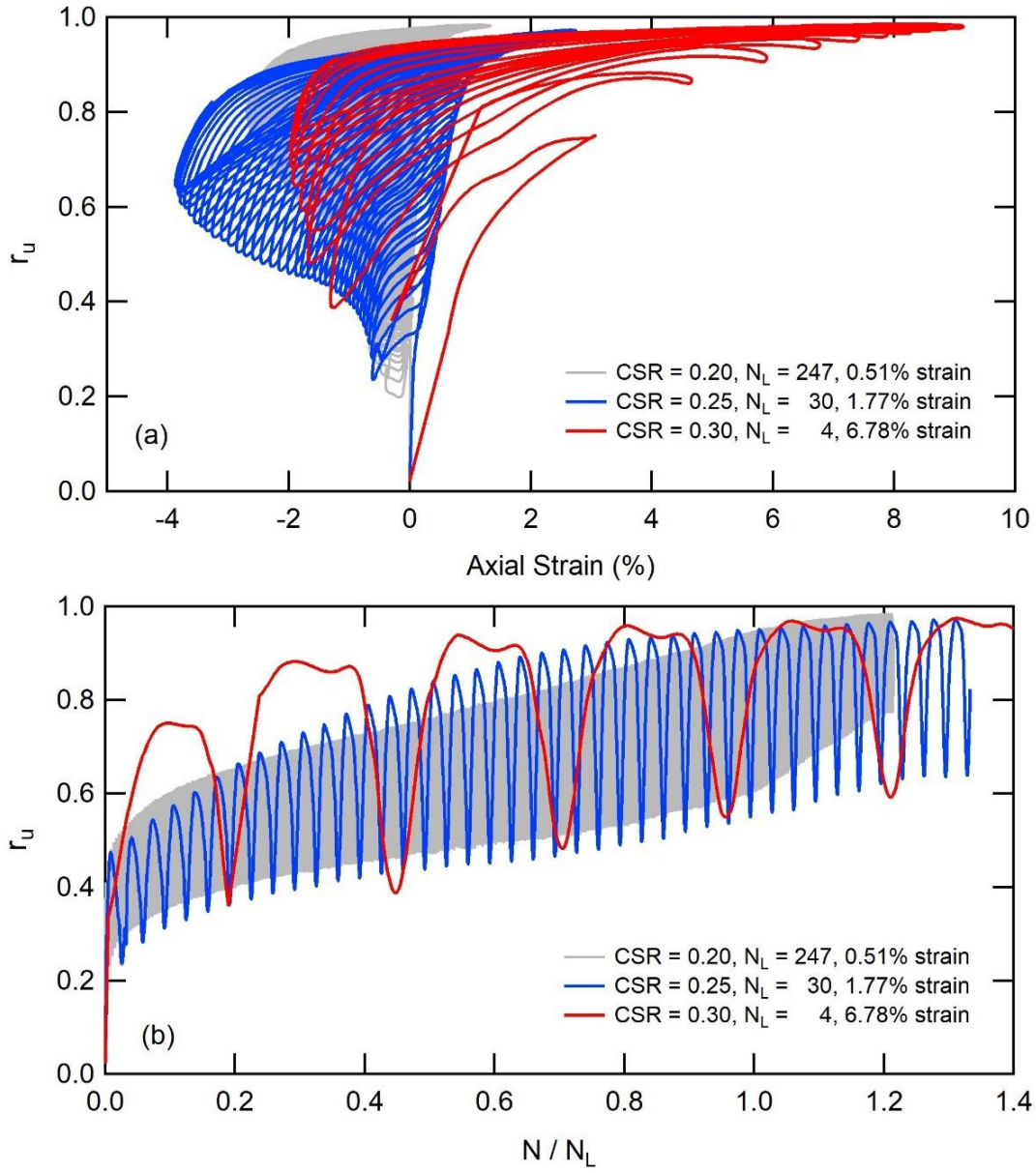

Figure 3.5 Excess pore pressure ratio behaviors with:
a) axial stain, b) normalized number of shaking cycles.

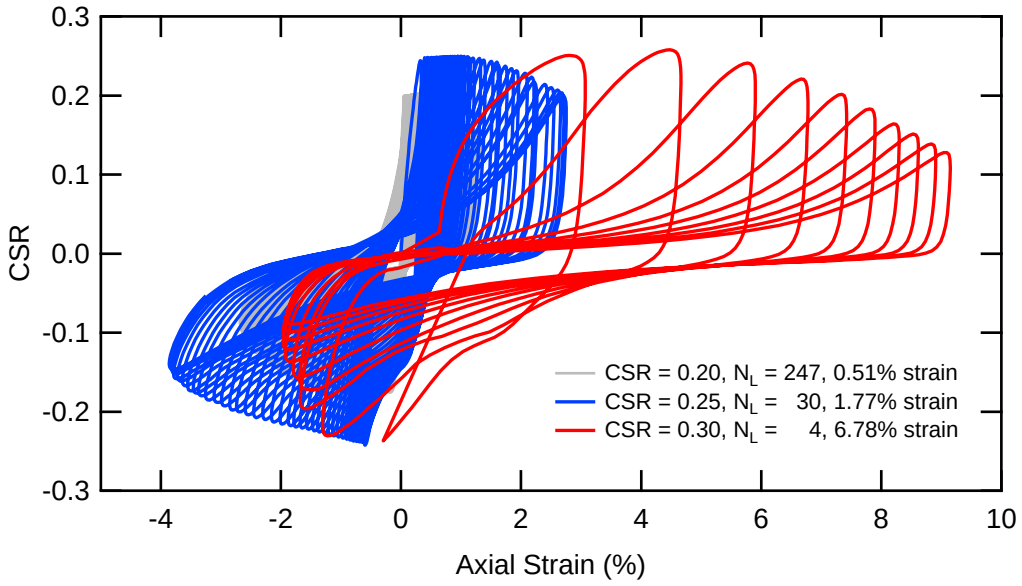

Figure 3.6 Effect of cyclic stress ratio on axial strain.

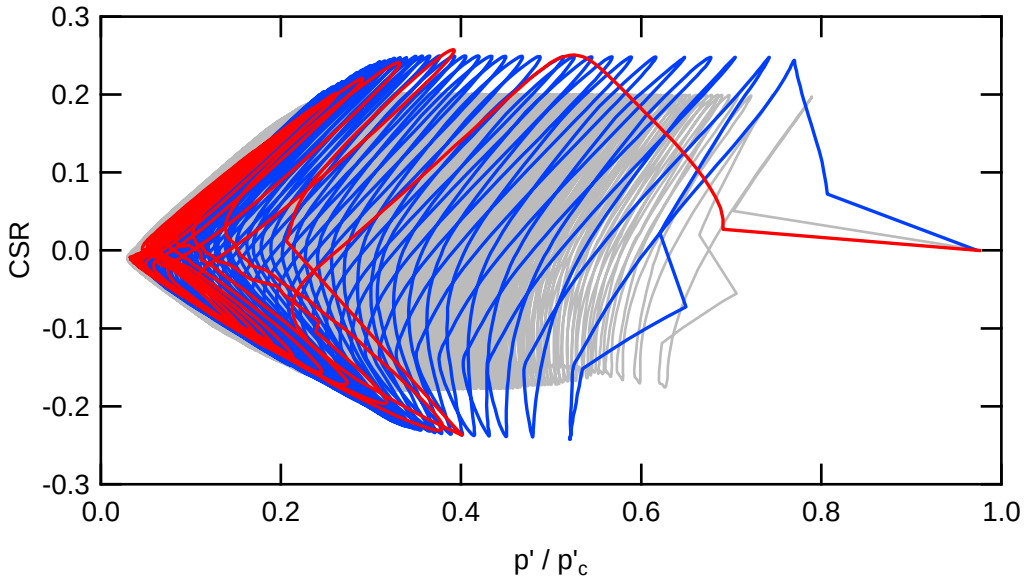

Figure 3.7 Effect of cyclic stress ratio on the normalized effective stress.

3.5.2 Phase Transform Friction Angle of Gravelly Soils

In this study, the mean effective stress (p') decreases as the number of cycles increases because of the pore water pressure development during the cyclic loading. The initial liquefaction occurred when the normalized mean effective stress (p'/p'_c) of around 0.1 was reached for all the tests. The phase transform friction angle (ϕ'_{pt}) was used as a reference point to indicate when the sample behavior switches from contractive to dilative behavior (Sivathayalan 1994, Vaid and Sivathayalan 1996, Porcino et al. 2008, Hubler et al. 2017). It was evaluated from the effective stress path using the slope of a line from the origin to the cycle at a r_u of 0.95, as presented in Figure 3.8. A summary of the ϕ'_{pt} for each sample is presented in Table 3.3. The maximum ϕ'_{pt} was approximately 41.6 degrees for undisturbed samples, while it was approximately 35 degrees for reconstituted samples. Due to the natural densification and cementation processes in the field, it is possible that the undisturbed sample was stronger than the reconstituted sample.

3.5.3 Ultimate Friction Angle of Gravelly soil

Two isotropically consolidated drained (CID) triaxial tests were conducted to estimate the ultimate friction angle of a gravel sample. The tests were performed on a reconstituted sample (GR-H10), which contained 50% gravel, 38% sand, and 12% fines by weight. This composition is a representative of the composition of all samples. No pore pressure development during the drained shearing, thus the effective ultimate friction angle (ϕ'_{ult}) was directly obtained. The ϕ'_{ult} was determined from the major and minor principal stresses at failure corresponding to 15 and 20% axial strain for the

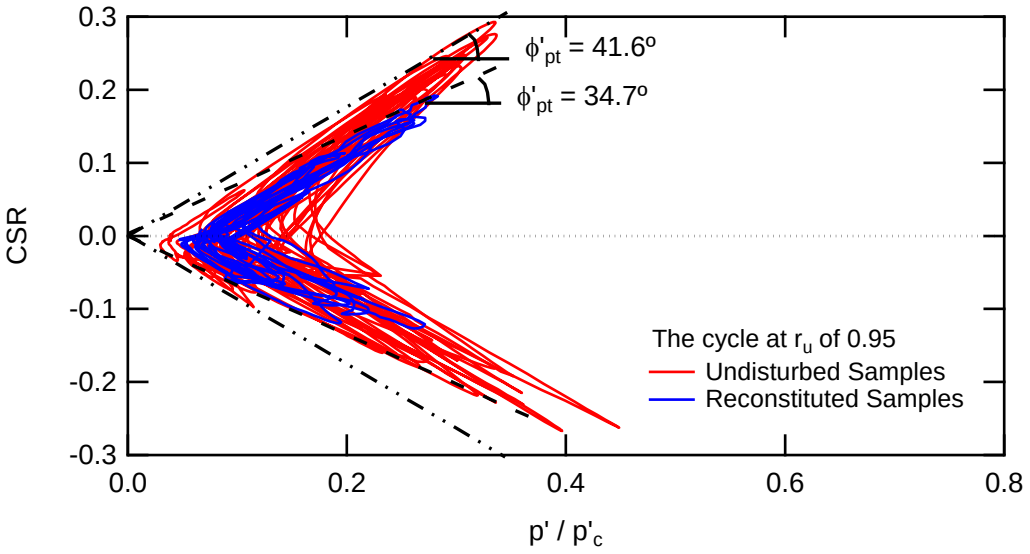

Figure 3.8 Average phase transform friction angle of the cycle at r_u of 0.95.

two tests. As presented in Figure 3.9, the ϕ'_{ult} from Sample GR-H10 was found to be 51.5° regardless of the strain level. It should be noted that Hubler et al. (2017) found comparable results utilizing cyclic simple shear (DSS) testing on round to sub-angular pure gravels with a relative density between 40 and 80 percent, and the soil composition was found to have some influence on the friction angle. Hubler et al. (2017) reported the ϕ'_{ult} of 40-30° and the ϕ'_{pt} of 32-27° for pure gravels. In this study, the ϕ'_{ult} (of 51.5°) obtained from CIDTX testing was found to be slightly higher than the ϕ'_{pt} (of 35-42°) obtained from CTX testing for the gravelly soils. The higher friction angles than Hubler et al. (2017) are possible due to the high angularity of the samples in this study. It is noted that the ϕ'_{pt} indicates the point at which the sample reaches r_u of 0.95 during cyclic loading, whereas the ϕ'_{ult} represents a failure under static loading.

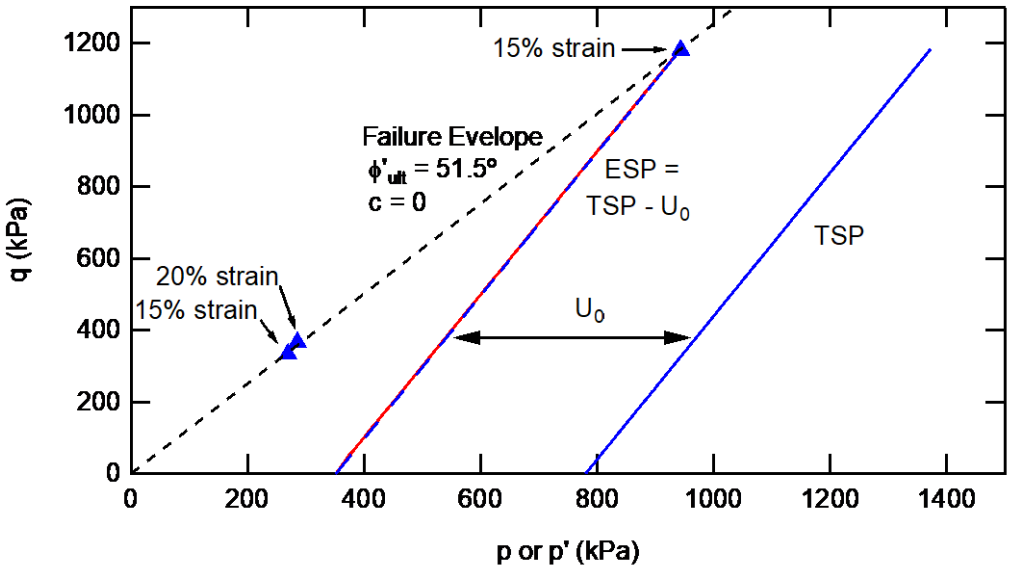

Figure 3.9 Ultimate friction angle from the CIDTX test.

3.5.4 Effect of Cyclic Stress Ratio on Number of Cycles

The cyclic stress ratio (CSR) and the corresponding number of cycles to cause initial liquefaction (N_L) are presented in Figure 3.10 for all the tests. This value of CSR then becomes the cyclic resistant ratio (CRR) for these soils. Results are separated into three ranges of effective confining stresses: 100, 180, and 325 kPa. It was found that the CRR increases as the N_L decreases. The effective confining stress (σ'_c) is lower at the higher CRR. The slopes of the CRR - NL lines for σ'_c of 100 and 180 kPa are comparable, however the slope of the line for 325 kPa is steeper. The lines for the σ'_c of 180 and 325 kPa are merged at the N_L below third cycle. This observation is similar to the behavior of clean sand suggested by Vaid and Sivathayalan (1996). It is noted that the relative densities of the specimens are close, leading to the dry densities of these specimens being in similar range. In addition, Hubler et al. (2017) found that density does not significantly affect the cyclic behavior of pure-pea gravels. Based on the observation, it appears that the effect of effective confining stress is significant.

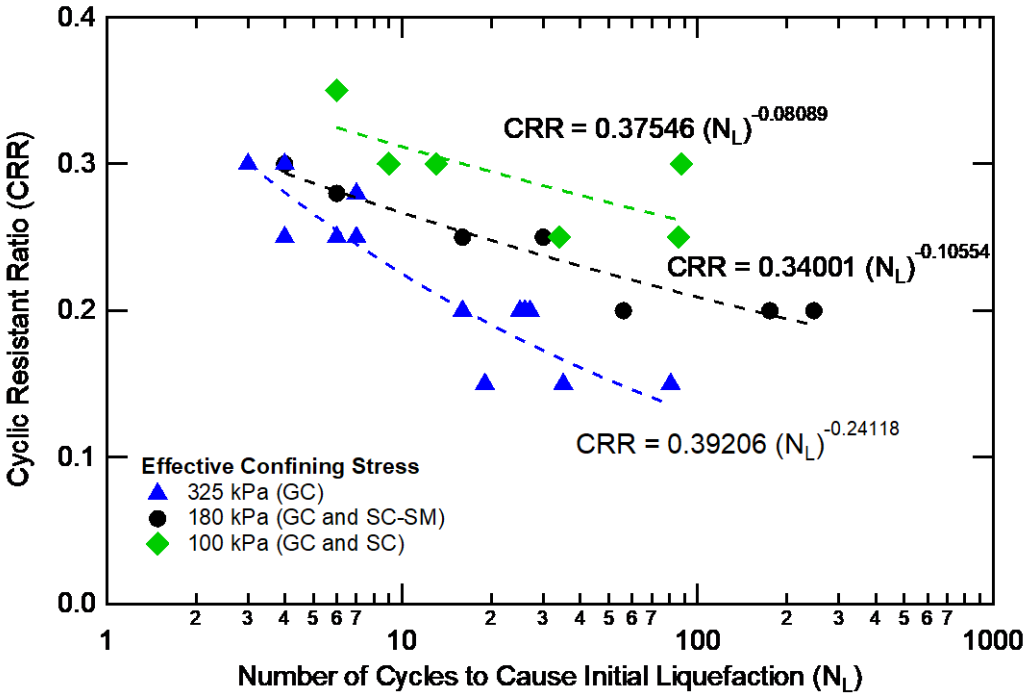

Figure 3.10 Effect of cyclic resistance ratio on the number of cycles to cause initial liquefaction based on cyclic triaxial testing.

Correlations are developed to estimate the CRR from N_L for effective confining stresses of 100, 180, and 325 kPa, as presented in Eqn. 3.1-3.3. Based on the data shown in Figure 3.10, the cyclic resistance ratio at an earthquake magnitude of 7.5 ($CRR_{M=7.5}$) can be determined using the CSR at 15 cycles. The $CRR_{M=7.5}$ is 0.20, 0.26, and 0.30 for effective confining stress of 100, 180, and 325 kPa, respectively.

$$CRR_{CTX} = 0.39206\ (N_L)^{-0.24118} \qquad \text{for } \sigma'_c \text{ of 325 kPa} \qquad \text{Eqn. 3.1}$$

$$CRR_{CTX} = 0.34001\ (N_L)^{-0.10554} \qquad \text{for } \sigma'_c \text{ of 180 kPa} \qquad \text{Eqn. 3.2}$$

$$CRR_{CTX} = 0.37546\ (N_L)^{-0.08089} \qquad \text{for } \sigma'_c \text{ of 100 kPa} \qquad \text{Eqn. 3.3}$$

It should be noted that the CRR obtained using cyclic triaxial (CTX) testing is significantly higher than the CRR obtained using direct simple shear (DSS) testing. The correlation used to correct those CRRs is presented below (Finn et al. 1971, Seed and Peacock 1971, Castro 1975, and Kramer 1996). The DSS testing overestimated the field CRR value by about 10%

$$CRR_{field} = 0.9(CRR_{DSS}) = 0.9\ (C_r)(CRR_{CTX}) \qquad \text{Eqn. 3.4}$$

$$c_r = (1+ K_0) / 2 \qquad \text{Eqn. 3.5}$$

The correction factor (C_r) can be obtained using Equation 3.5. If K_0 is assumed to be 0.5, the Cr value is 0.75, indicating that the CRR obtained from the CTX testing is overestimated by around 25% compared to the CRR from the DSS testing. Therefore, the range of CRR was reduced from approximately 0.35 to 0.26. The correlation between CRR and the number of cycles to cause liquefaction for DSS was presented in Figure 3.11 and Equation 3.6-3.8. The $CRR_{M=7.5}$ for DSS is 0.16, 0.20, and 0.23 for effective confining stress of 100, 180, and 325 kPa, respectively.

$$CRR_{DSS} = 0.31517(N_L)^{-0.24118} \quad \text{for } \sigma'_c \text{ of 325 kPa} \qquad \text{Eqn. 3.6}$$

$$CRR_{DSS} = 0.26287\ (N_L)^{-0.10554} \quad \text{for } \sigma'_c \text{ of 180 kPa} \qquad \text{Eqn. 3.7}$$

$$CRR_{DSS} = 0.28822\ (N_L)^{-0.08089} \quad \text{for } \sigma'_c \text{ of 100 kPa} \qquad \text{Eqn. 3.8}$$

Based on both testing methods, the $CRR_{M=7.5}$ decreased with increasing effective confining stress. The effect of normalization of the effective confining stress (σ'_c/P_a) on $CRR_{M=7.5}$ was presented in Figure 3.12, and it was found that the $CRR_{M=7.5}$ decreases as the σ'_c/P_a increases. The following equations are provided for the gravelly soils tested in this study.

$$CRR_{M=7.5} = -0.04298(\sigma'_c/P_a) + 0.33926 \quad \text{for CTX testing} \quad \text{Eqn. 3.9}$$

$$CRR_{M=7.5} = -0.02955(\sigma'_c/P_a) + 0.25651 \quad \text{for DSS testing} \quad \text{Eqn. 3.10}$$

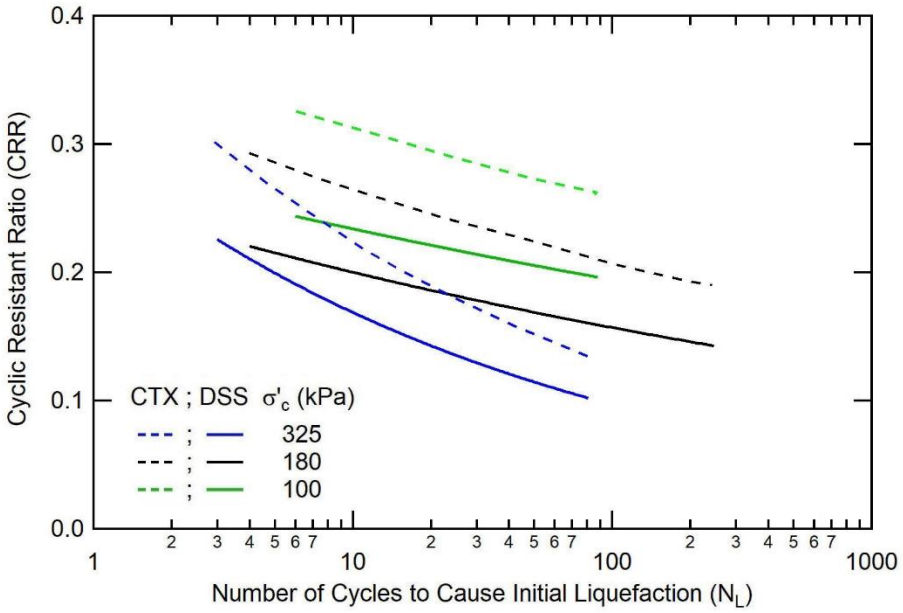

Figure 3.11 Estimation of cyclic resistance ratio for DSS testing with number of cycles to cause liquefaction from CTX testing data.

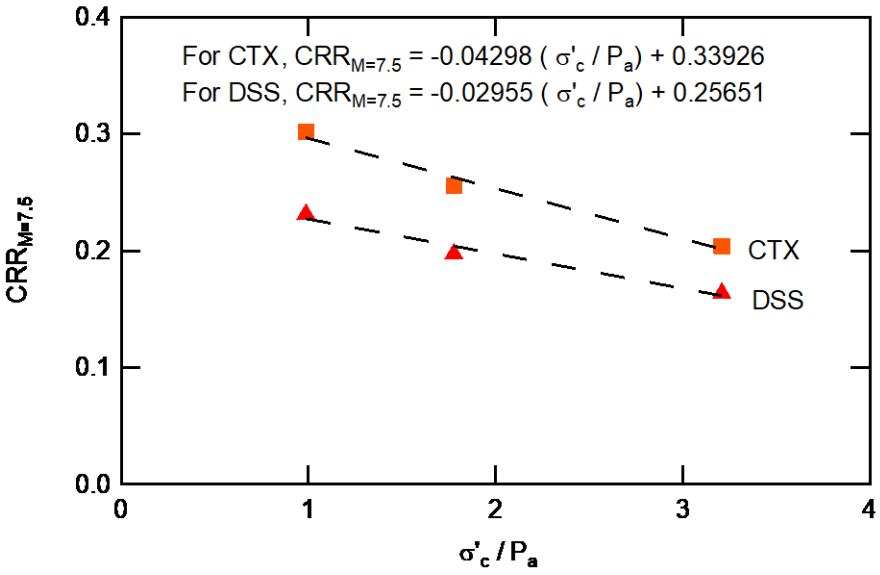

Figure 3.12 Effect of $CRR_{M=7.5}$ on the normalized effective confining stress.

The relationship between CRR and N_L of gravelly soils were compared with the behaviors of clean sand proposed by De Alba et al. (1976) because the work consists of a large database for clean sands and has been cited by numerous scientific papers (e.g., Seed et al. 1985, Andrus and Stokoe 1997, Idriss and Boulanger 2006, Andrianopoulos et al. 2010, Abdoun et al. 2013, and Boulanger and Idriss 2015). The relationship of gravelly soils in this study was also compared to the behaviors of clean gravel proposed by Hubler et al. (2017) due to having data available. Figure 3.13 shows that the range of CRR for gravelly soils falls in the same range as clean sand. It is noted that the tests in this study were conducted at higher effective stresses. However, when compared to pure gravel under 100 kPa of effective stress, gravelly soils in this study required a significantly higher number of cycles to liquefy. This could be related to the higher friction angles as analyzed in the previous section.

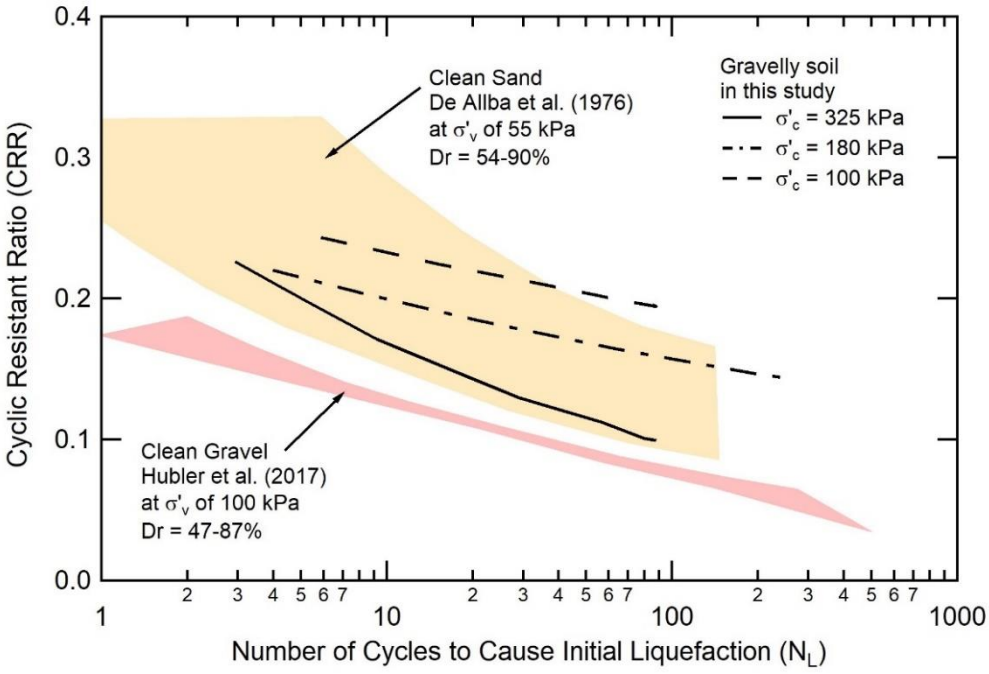

Figure 3.13 Comparison of CRR for gravelly soils in this study with pure sand and gravel.

The effect of effective stress was described in literature by the overburden correction factor (K_σ), originally proposed by Seed (1983). The K_σ can be determined using the following equation:

$$K_\sigma = \frac{CRR_{\sigma'_c}}{CRR_{\sigma'_{c=1}}} \qquad \text{Eqn. 3.11}$$

Where $CRR_{\sigma'c}$ is the CRR at the specific σ'_c and $CRR_{\sigma'c=1}$ is the CRR at atmospheric pressure. The K_σ for the gravelly soils in this study was found to be lower at higher σ'_c as presented in Figure 3.14. In comparison to sand, the K_σ value for gravelly soils is slightly lower than the K_σ value for the sand samples obtained by Seed and Harder (1990) and Harder and Boulanger (1997). This could be because the K_σ in the literature were calculated using a failure criterion of 3% strain in 10 cycles. This study utilizes the criteria for r_u of 0.95 rather than strain criteria due to the significant effect of particle interlocking on the strain level. In addition, the gravelly soils have higher relative densities than the sand samples tested by Vaid and Sivathayalan (1996).

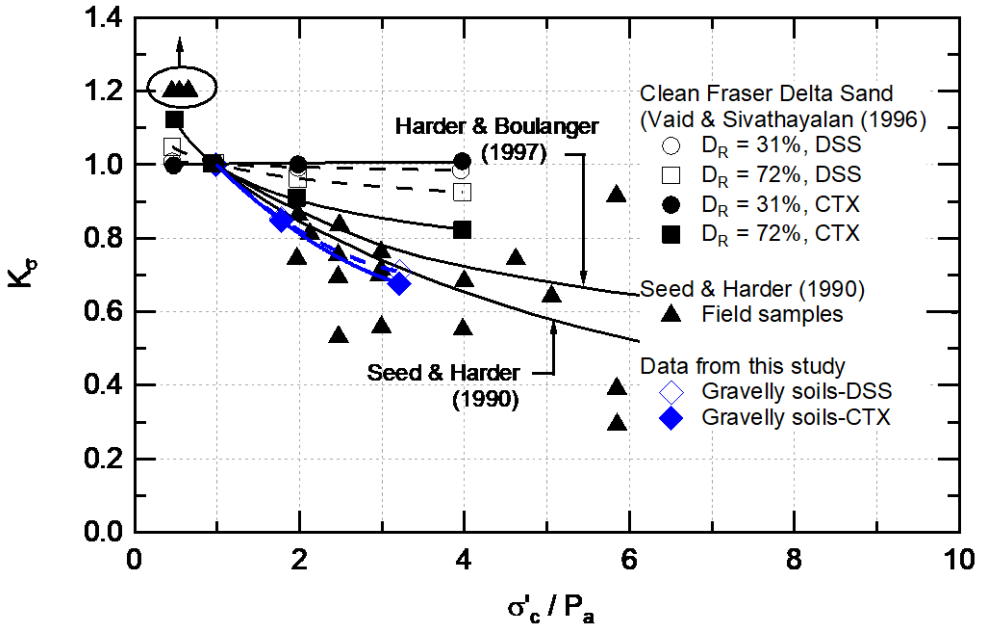

Figure 3.14 Comparison of K_σ of gravelly soils with sandy soils.

3.5.5 V_s-Based Assessment of Liquefaction Susceptibility

In general, the liquefaction susceptibility is assessed by the relationship between CRR and shear wave velocity (V_s). The Vs-based liquefaction susceptibility chart was initially developed for sandy soils, which typically has a V_s below 250 m/s (Andrus and Stokoe 2000). To date, there is no liquefaction susceptibility chart available for gravelly soils. In this study, the V_s was obtained from resonant column (RC) testing for representative gravelly soil samples, collected from a borehole near other boreholes where the CTX samples were collected. Unfortunately, only one undisturbed sample of the G1-S8 Shelby tube was tested in the resonant column. Results are presented in Section 2.3.6. The adjusted shear wave velocity at the atmospheric pressure ($V_{s,1}$) for G1-S8 samples is approximately 351 m/s, while the $V_{s,1}$ for four reconstituted samples ranging for 260-400 m/s. The CTX test results indicated that the gravelly soils liquefied with CRR_{DSS} ranging between 0.15 and 0.35, while the $V_{s,1}$ of these materials was higher than 260 m/s, falling in the no-liquefaction zone proposed by Andrus and Stokoe (2000) as shown in Figure 3.15. Hubler et al. (2017) also found that the pure gravel is liquefiable material at the CRR_{DSS} higher than 0.07 within range of $V_{s,1}$ higher than 260 m/s. This observation indicates that the Vs value is not appropriate for the liquefaction assessment of gravelly soils.

3.5.6 Shear Modulus and Damping Behavior

The shear modulus (G) and damping (D) over a range of shear strain between 0.0001 and 0.02% were measured using the resonant column (RC) test at 3 different

confining pressures on Sample ID: G1-S8. Dynamic behaviors at the confinement of 325 kPa were estimated based on the modified hyperbolic equation proposed by

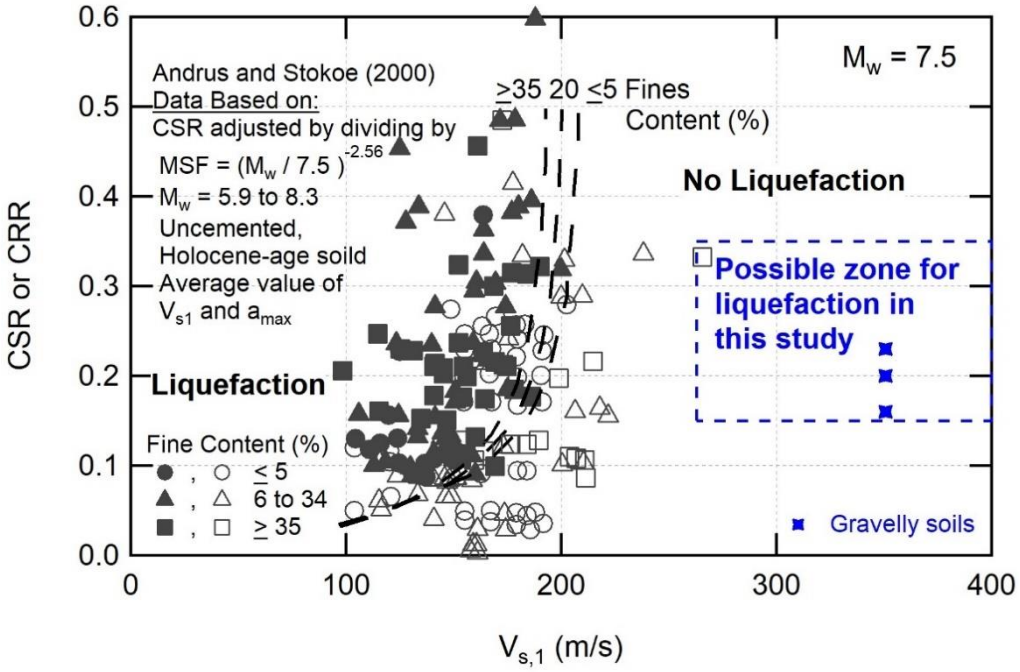

Figure 3.15 Comparison of $CRR_{M=7.5}$ and $V_{s,1}$ of gravelly soils with liquefaction susceptibility chart (modified from Andrus and Stokoe 2000).

Stokoe et al. (1999) as well as the standard polynomial equations. The purpose is to compare with results measured from the cyclic triaxial (CTX) tests at the same effective stress. The CTX results are not directly comparable because of the different loading conditions. The equations derived by Barden (1963) used to adjust the axial strain to shear strain were suggested by Pyke (1978). The equation accounts for an effect of inherent anisotropy of the stress-strain loop behavior that was observed to be similar to the results found in this study. The anisotropic shear modulus (G_{hv} or G_{aniso}) is presented as:

$$G_{hv} = \frac{E_v}{(1+1/n+2\mu_{vh})} \qquad \text{Eqn. 3.12}$$

where $n = E_h / E_v$ is Young's modulus in the horizontal per vertical direction, and μ_{vh} is the ratio of the strain in the horizontal to the vertical direction. For a linear elastic material, the isotropic shear modulus (G_{iso}) is described in the following equation:

$$G_{iso} = \frac{E}{2\,(1+\mu)} \qquad \text{Eqn. 3.13}$$

where E is Young's modulus, and μ is Poisson's ratio. The μ value of 0.3 is assumed in accordance with the typical gravelly soils. It is to convert the E to the G_{iso}, and the effect of anisotropic shear modulus is accounted using an equation proposed by Park and Silver (1975) as following:

$$G_{aniso} = G_{iso} \cdot (1 - K_0) \qquad \text{Eqn. 3.14}$$

where the coefficient of lateral earth pressure (K_0) of 0.5 is assumed as typical value. The damping (D) of each cycle can be estimated using the hysteretic loop as shown in Figure 3.16. Because damping represents the ratio of the loop area (A_{loop}) to the triangular area (A_T) of maximum stress development, the damping calculated from an axial stress-strain plot is equal to the damping obtained from a shear stress-strain plot in accordance with Kumar et al. (2020).

$$D = A_{loop} / (4\,\pi\,A_T) \qquad \text{Eqn. 3.15}$$

$$A_T = (\sigma \cdot \varepsilon)/2 \qquad \text{Eqn. 3.16}$$

The equation to calculate the damping is presented in Equation 3.16. The shear strain (γ) can be estimated from the axial strain using the following equation:

$$\gamma = \varepsilon_a - \varepsilon_r = \varepsilon_a \cdot (1 + \mu) \qquad \text{Eqn. 3.17}$$

where ε_a is the axial strain, and ε_r is the radial strain. The μ value of 0.3 is assumed to estimate the shear strain. Consequently, the shear modulus over the same range of shear strain can be developed based on the CTX results at an effective stress of 325 kPa as presented in Figure 3.17. The shear modulus and damping calculated from the CTX results were compared with the low-strain shear modulus and damping obtained by the RC test as presented in Figure 3.18. Therefore, shear modulus reduction and damping curves under the entire range of shear strain between 0.0001 to 5% were developed for the gravelly soils. It was found that damping is scattered at shear strains higher than 0.25%.

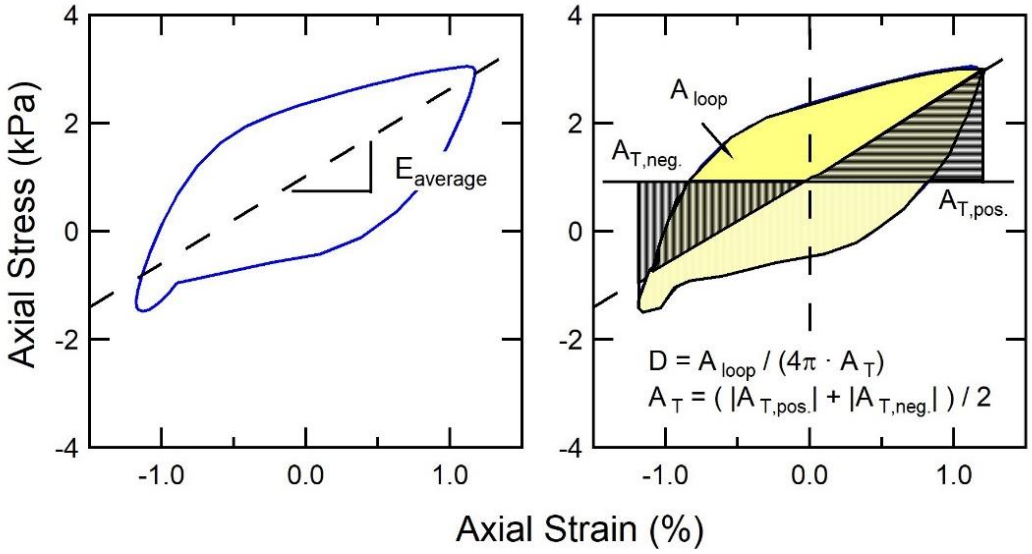

Figure 3.16 Concept of Young's modulus and damping calculated from cyclic triaxial data.

The correlation between damping and pore pressure development was also investigated as presented in Figure 3.18 (b) and (c). The damping values increase as r_u increases. It is interesting to observe the damping reached a maximum value at some point then started to decrease. This point of the damping curves coincides with the high excess pore water pressure development occurred at the initial liquefaction. This implies that when

the soil began to change from a solid state to a liquid state, the energy dissipation capability is reduced.

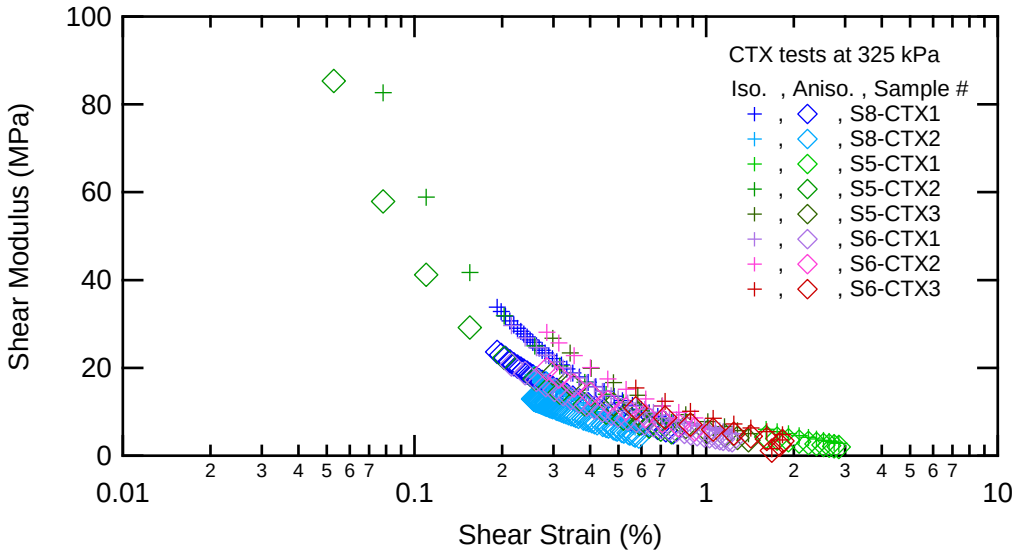

Figure 3.17 Comparison between isotropic and an isotropic shear modulus obtained from cyclic triaxial testing results.

3.5.7 Post cyclic (monotonic) loading behavior

Post-cyclic loading tests were conducted under undrained conditions imme-diately after the cyclic loading test. The deviator stress and pore pressure dissipation were analyzed to estimate the strength parameters, including friction angle and cohesion. An example of post-cyclic loading test of Sample ID G1-S8 is presented in Figure 3.19. At the end of the cyclic loading test, the liquefied soil sample had high excess pore water pressure and it began to dissipate under the post- cyclic monotonic undrained loading condition. Based on results shown in Figure 3.19, it was found that when the axial strain was less than 3%, the excess pore water pressure is nearly constant. This implies that the buildup of pore pressure due to the monotonic loading was counteracted by the dissipation of pore pressure

at the end of cyclic loading, hence there was no change in the excess pore pressure. However, it appears that the excess pore water pressure continued to dissipate until the axial strain reached 20%. The observations are in agreement with Hubler et al. (2017), and Sivathayalan and Yazdi.

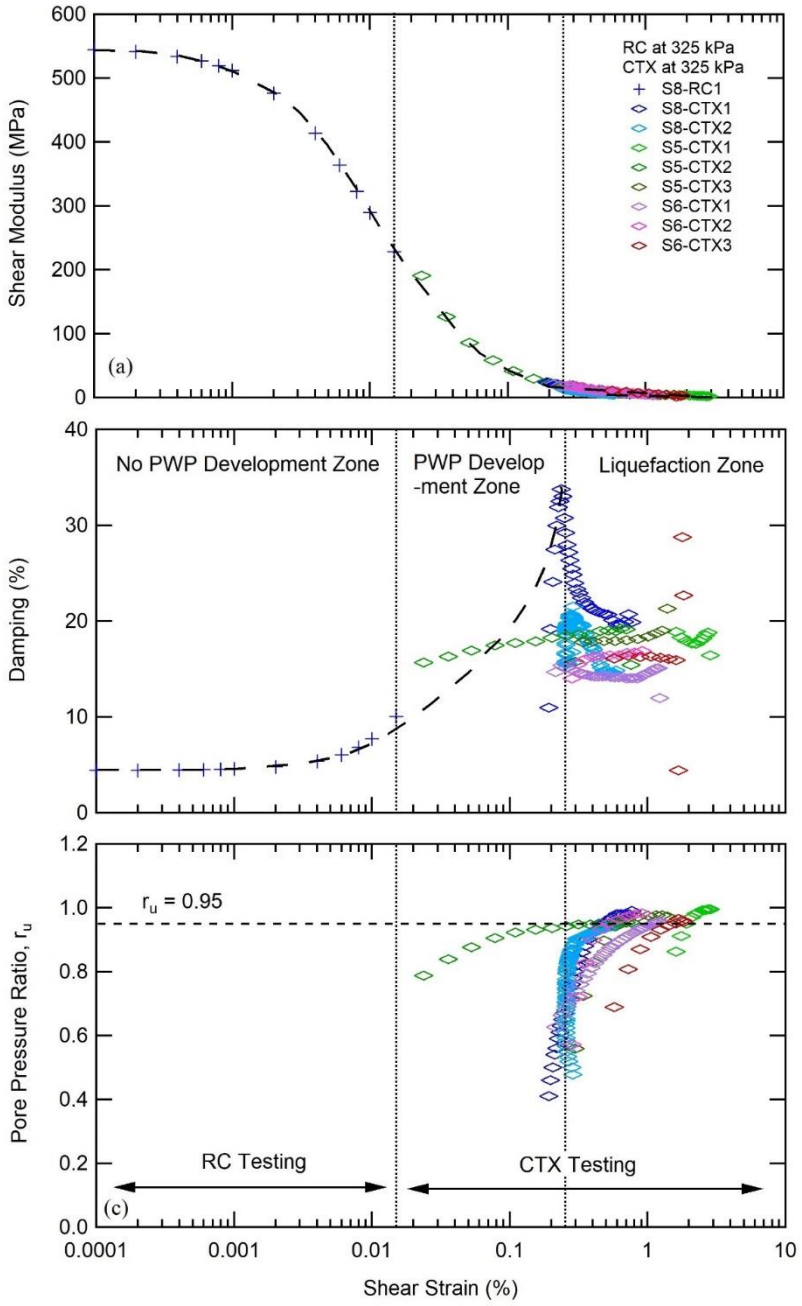

Figure 3.18 Dynamic behavior of mine waste material over all range of shear strain.

(2014). Hubler et al. (2017) also found that the shear modulus at shear strain level of between 5 and 20% for post-cyclic loading tests was very similar to the initial shear modulus for monotonic loading tests on undisturbed soils, and the residual strength of gravelly soil sample can be determined at 20% strain. Due to the soil being under temporary zero effective stress at the beginning of the post-cyclic test, peak failure was not observed indicating that the specimens behave similarly to loose soil. However, the negative pore pressure developed during the shearing indicative of the soil dilative behavior.

The normalized deviator stress ($\Delta\sigma/\sigma'_c$) and normalized excess pore pressure with shear strain of the undisturbed samples are shown in Figure 3.20. The deviator stress in these samples began to develop at a shear strain of approximately 2 to 4%, which corresponds to the pore pressure dissipation following the end of cyclic loading tests. As mentioned, most of the samples liquefied during the cyclic loading test, which resulted in the maximum excess pore pressure at the beginning of the post-cycle loading test. During post-cyclic loading, the pore pressure gradually dissipated until the axial strain reached above 10%. The influence of effective confining stress (σ'_c) was evidenced as higher pore water dissipation that was observed the higher σ'_c value for the same axial strain. More variation of $\Delta\sigma/\sigma'_c$ was found in testing at the lower σ'_c, regardless of the initial properties, which might influence the behavior of the undisturbed soil samples. Figure 3.21 presents the post-cyclic behavior of the reconstituted samples. The effect of σ'_c was clearly observed as the $\Delta\sigma/\sigma'_c$ increased when the σ'_c increased, while the pore pressure dissipation increased. At 20% strain, the $\Delta\sigma/\sigma'_c$ ranged from 0.3 to 0.6, which is significantly lower than the undisturbed samples. It is noted that the reconstituted samples were slightly looser than the undisturbed samples.

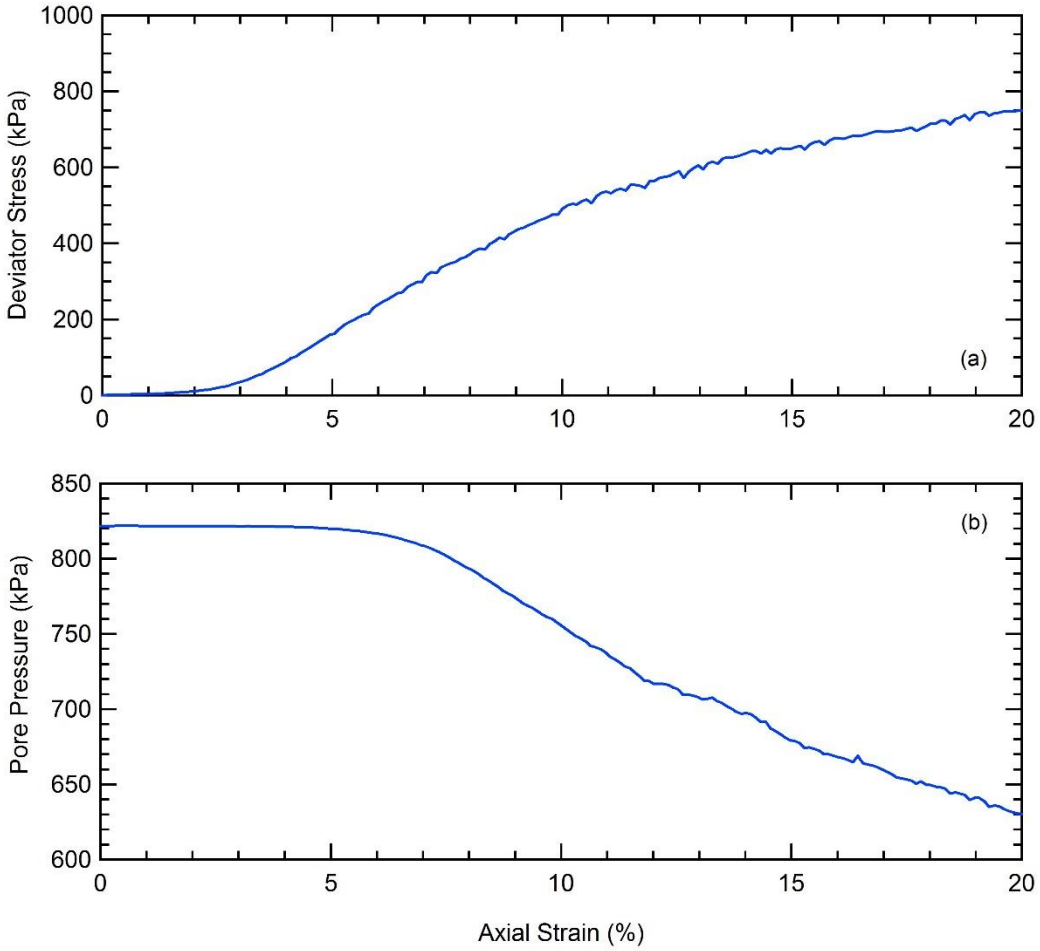

Figure 3.19 Example of post cyclic loading behavior.

The major and minor principal stresses at failure were calculated using undrained post-cyclic loading tests at 5-20% axial strain for all 30 undisturbed samples to determine strength parameters, including friction angle (ϕ') and cohesion (c'). Figure 3.22 presents Mohr-Coulomb failure envelopes at four axial strain levels at 5, 10, 15, and 20% strain. The small variation of soil content and density on the ϕ' was observed as the ϕ' was found to be between 31 and 34°, while the c' was found to be zero. These values fall within the same range for pure gravels (ϕ'= 30 - 40°) reported by Hubler et al. (2017). The ϕ' slightly decreases as axial strain increases, indicating the strength reduction with strain, as

presented in Figure 3.23. The equation to estimate the ϕ' with axial strain (ε) is presented in the following equation.

$$\phi' = 9.3457\ (\varepsilon)^{-0.61975} + 30.416 \qquad \text{Eqn. 3.18}$$

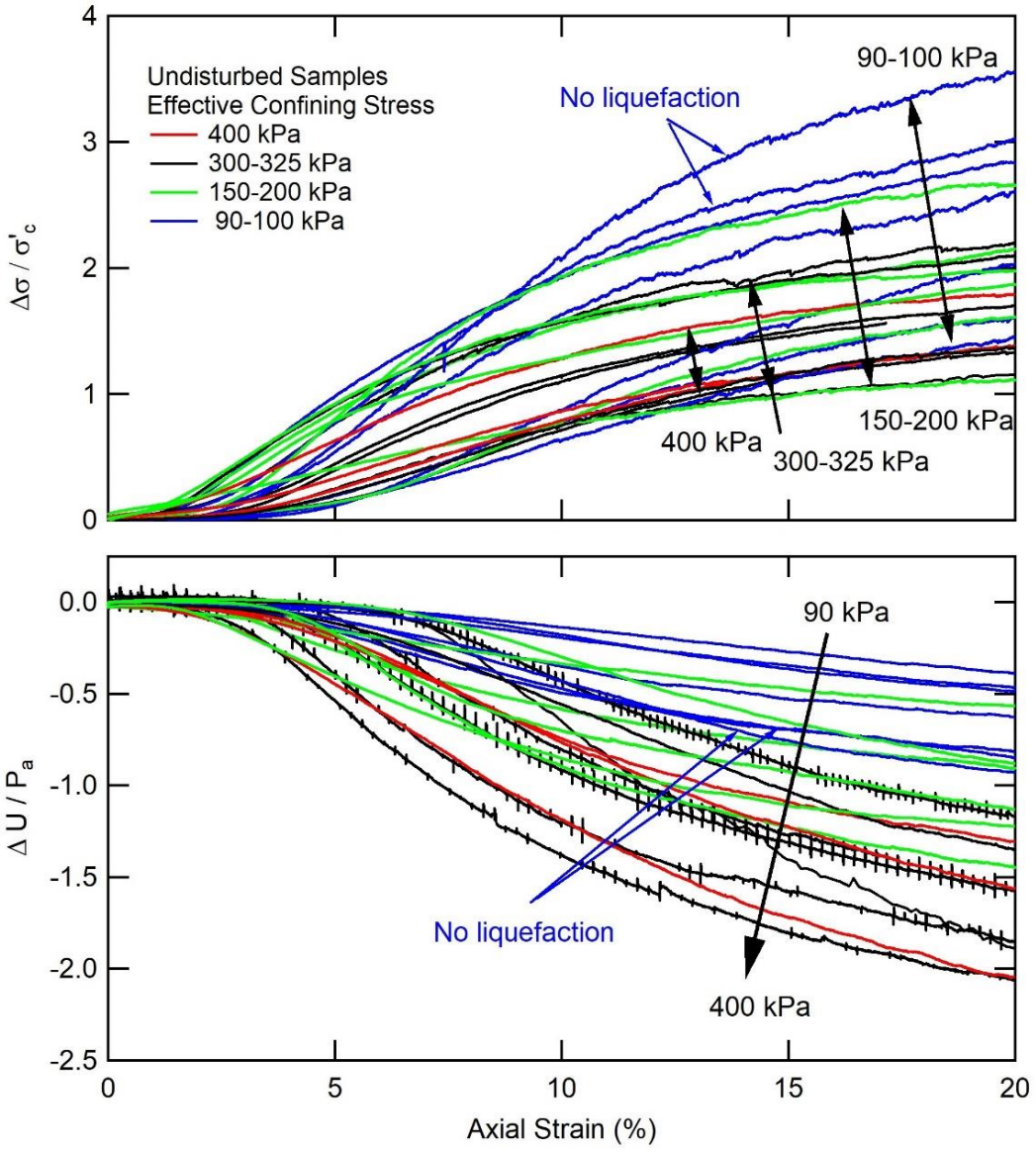

Figure 3.20 Post-cyclic loading test for undisturbed samples.

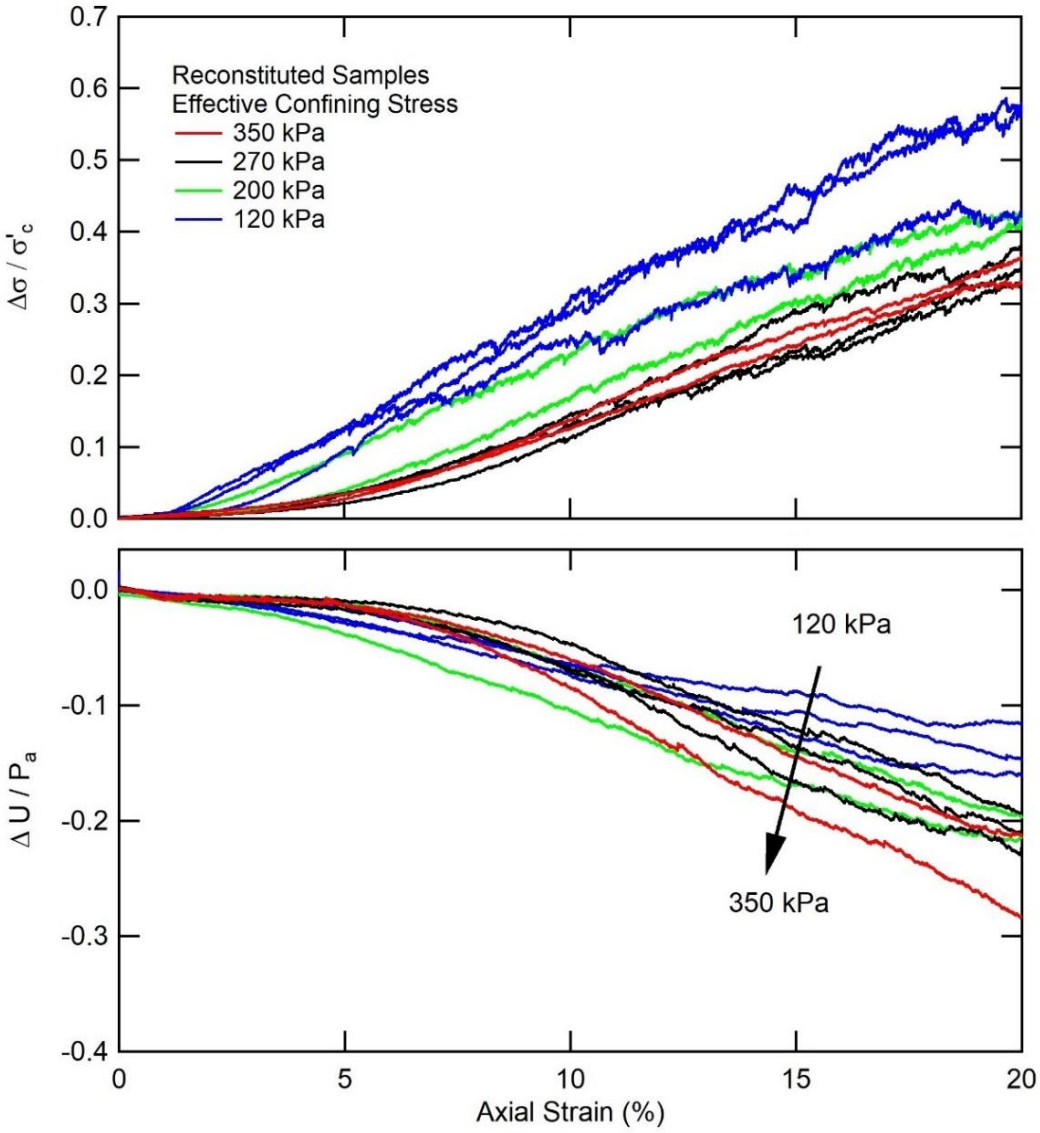

Figure 3.21 Post-cyclic loading test for reconstituted samples.

Due to the gravelly soils in this study having a comparable soil composition, the effect of particle interlocking on the friction angle is expected to be comparable. The average ϕ' of these gravelly soils was approximately 32.5°. At 5 to 20% strain, a small variation of the ϕ' was observed within ±5%, indicating that the axial strain had low effect on the ϕ'. The gravelly soil would change from contractive to dilative behaviors when the

stress path passed through the phase transform line at 41.6° due to initial liquefaction. During liquefaction, the strength of the gravelly soil was significantly reduced, then regained to the ϕ' of 32.5° during post-liquefaction due to pore pressure dissipation. It is noted that if the stress path reached the ultimate line at 51.1° in either static or dynamic loading conditions, the gravelly soil would be considered a complete collapse.

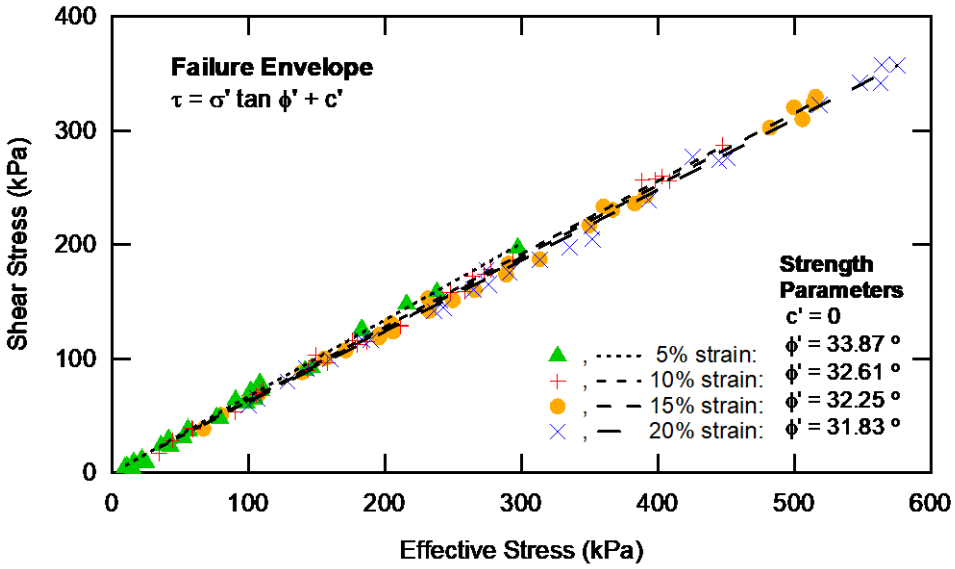

Figure 3.22 Mohr-Coulomb failure envelope
for post cyclic loading test of undisturbed samples.

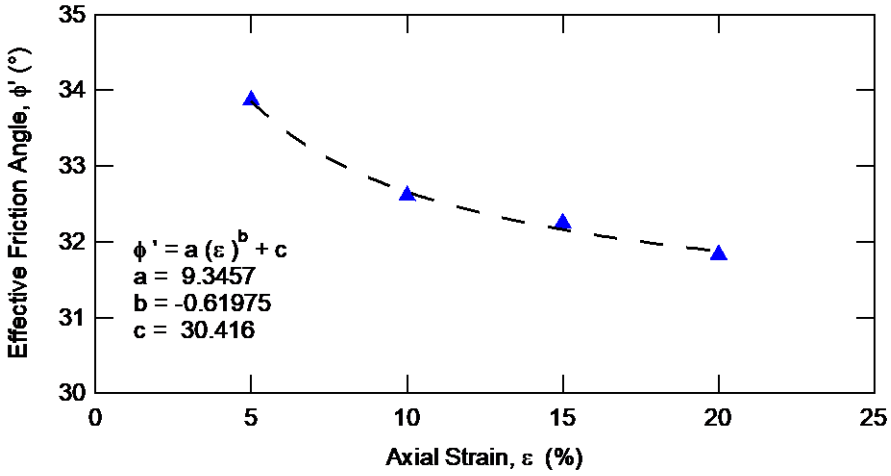

Figure 3.23 Correlation between strength parameter
with axial strain after liquefaction of undisturbed samples.

3.6 Analysis of Soil Composition

3.6.1 Effect of Soil Composition on Liquefaction

Figure 3.24 shows a relationship between gravel, sand, and fines content and the $CRR_{M=7.5}$ at the effective confining stress of 325 kPa. It was observed that the $CRR_{M=7.5}$ increases as the difference between sand and fines contents significantly increases. However, no correlation between gravel content and the $CRR_{M=7.5}$ was observed. Figure 3.25 presents a relationship between the soil composition and the $CRR_{M=7.5}$ at various effective stresses. Based on the results of soils containing gravel content between 40 and 55%, the difference between sand and fines contents may have some influence on the $CRR_{M=7.5}$. However, more data is needed to further assess the impact of effective confining stress on the $CRR_{M=7.5}$. Further investigation of soil structure matrix based on different soil composition was performed in the following section.

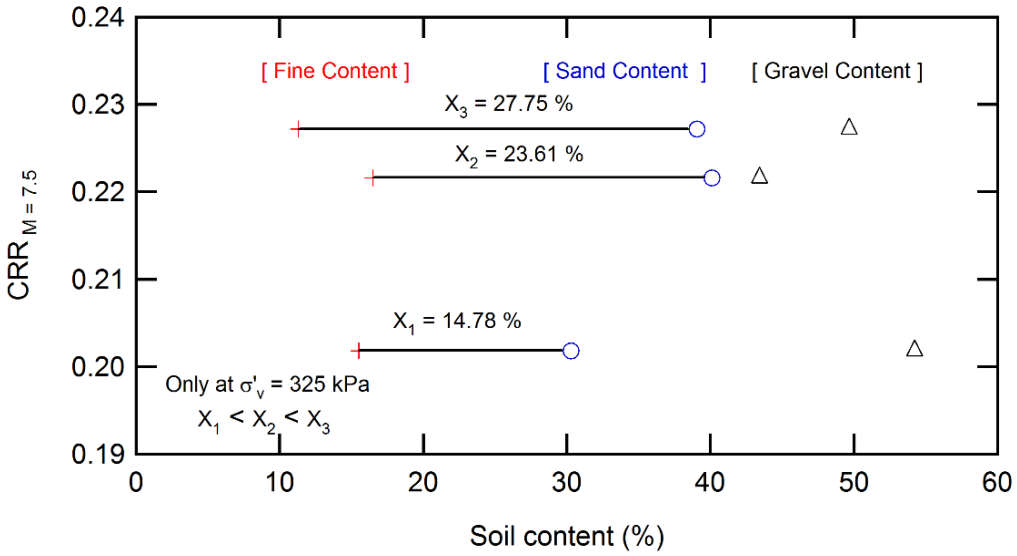

Figure 3.24 Effect of soil composition on the cyclic resistance ratio at a given earthquake magnitude of 7.5 ($CRR_{M=7.5}$) at effective confining stress of 325 kPa.

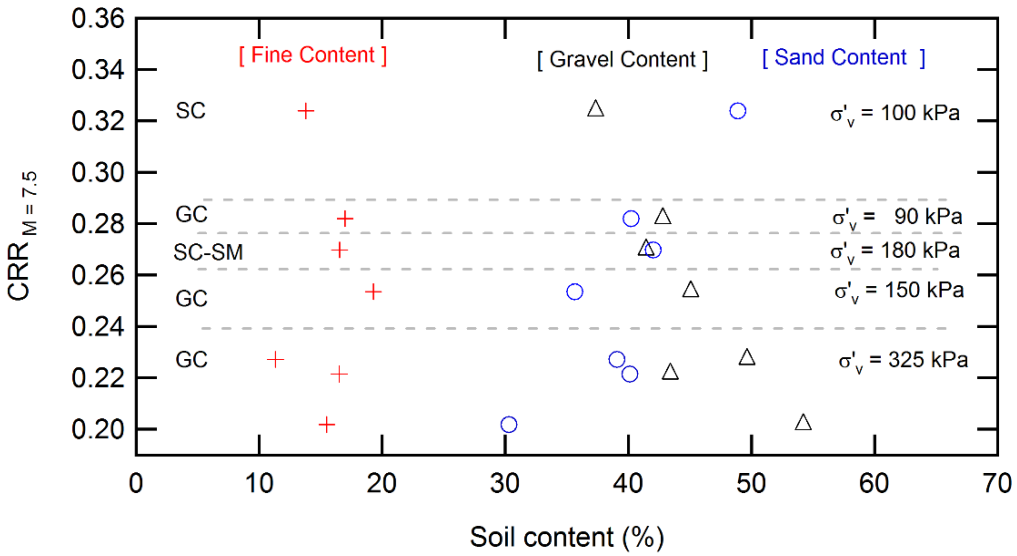

Figure 3.25 Effect of soil composition on the cyclic resistance ratio at a given earthquake magnitude of 7.5 ($CRR_{M=7.5}$) at different effective confining stress.

3.6.2 Effect of Soil Fabric and Structure Matrix on Liquefaction

Several research studies have effectively investigated the soil behaviors associated with materials composed of gravel and sand, sand and fines, and gravel and fines (e.g., Yamamuro and Covert 2001, Do et al. 2016, Hubler et al. 2018). However, when mixing gravel, sand, and fines, the investigation of the mechanical properties and behaviors of the mixture is challenging as a large variation of soil fabrics can result in the infinite possibilities of soil structure matrix. Using the concept of phase relationship, this study aimed to develop an insight into the soil structure matrix consisting of gravel, sand, and fines. Figure 3.26 presents a concept of phase relationship of a composite soil containing gravel, sand, and fines.

To evaluate the possible soil structure matrix of composite soils, the volumes of solids (V_s) of each soil type were calculated and compared to the volumes of voids (V_v)

that can occur in each pure soil type. Three primary soil types were classified based on the unified soil classification system (USCS) as gravel (G), sand (S), and fines (F).

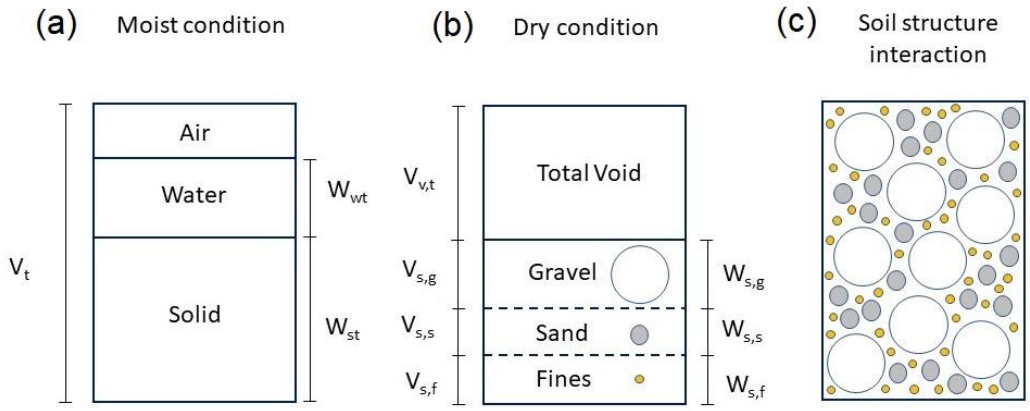

Figure 3.26 Phase relationship for a composite soil containing gravel, sand, and fines.

However, silt (M) and clay (C) were not separated from the fines in this study. The volume of solid and the void for each soil type were utilized under the assumption that the total volume of solid ($V_{s,t}$) is one. The conceptual phase relationship for a composite soil containing gravel, sand, and fines is presented in Figure 3.27. The percentage of gravel, percentage of sand, percentage of fines, and specific gravity (G_s) of gravel, sand, and fines are required as initial parameters for calculating the mass of gravel ($W_{s,g}$), sand ($W_{s,s}$), and fines ($W_{s,f}$).

$$G_{s,t} = \frac{(G_{s,g} \cdot \%\text{Gravel}) + (G_{s,s} \cdot \%\text{Sand}) + (G_{s,f} \cdot \%\text{Fines})}{100} \qquad \text{Eqn. 3.19}$$

$$W_{s,t} = (G_{s,t} \cdot \gamma_w) \cdot V_{s,t} \qquad \text{Eqn. 3.20}$$

$$W_{s,g} = \frac{W_{s,t} \cdot \%\text{Gravel}}{100} \qquad \text{Eqn. 3.21}$$

$$W_{s,s} = \frac{W_{s,t} \cdot \%\text{Sand}}{100} \qquad \text{Eqn. 3.22}$$

$$W_{s,f} = \frac{W_{s,t} \cdot \%\text{Fines}}{100} \qquad \text{Eqn. 3.23}$$

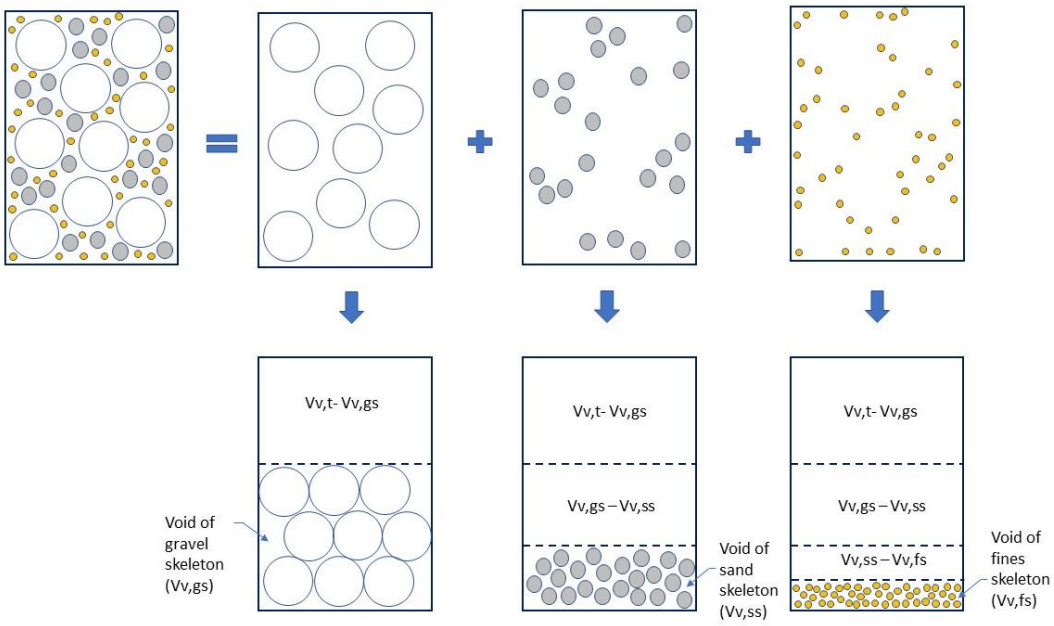

Figure 3.27 Conceptual of phase relationship for gravel, sand, and fine particles in a composite soil.

Then, using the following equation, the volume of gravel ($V_{s,g}$), sand ($V_{s,s}$), and fines ($V_{s,f}$) can be determined.

$$V_s = \frac{W_s}{G_s \cdot \gamma_w} \qquad \text{Eqn. 3.24}$$

The maximum and minimum dry densities ($\gamma_{d,max}$ and $\gamma_{d,min}$) of both gravel and sand are also required to determine the volume of void of gravel skeleton ($V_{v,gs}$) and sand skeleton ($V_{v,ss}$), which refers to the void space in pure gravel and pure sand under their densest and loosest conditions, respectively. The $V_{v,gs}$ and $V_{v,ss}$ can be calculated using the equations below.

$$V_{v,gs} = \left(\frac{G_{s,g} \cdot \gamma_w}{\gamma_{d,g}} - 1\right) \cdot V_{s,g} \quad \text{Eqn. 3.25}$$

$$V_{v,ss} = \left(\frac{G_{s,s} \cdot \gamma_w}{\gamma_{d,s}} - 1\right) \cdot V_{s,s} \quad \text{Eqn. 3.26}$$

After obtaining $V_{s,g}$, $V_{s,s}$, $V_{s,f}$, $V_{v,gs}$, and $V_{v,ss}$, the soil structure matrix can be analyzed by comparing $V_{v,gs}$ to $V_{s,s}$ and $V_{s,f}$. For example, three type of soil structure matrix can be defined: Interlocked Gravel matrix, Gravel-Sand matrix, and Gravel-Fines matrix. Interlocked Gravel Matrix is defined as when the $V_{v,gs}$ is larger than $V_{s,s} + V_{s,f}$, the sand and fine particles can pack into the void space between the gravel particles. The gravel particles are therefore in contact and interlocked with each other. Gravel-Sand Matrix and Gravel-Fines Matrix are possible when the $V_{v,gs}$ is less than $V_{s,s} + V_{s,f}$, the gravel particles float in the finer particles (sand and fines). Gravel-Sand Matrix is defined as when the $V_{v,ss}$ is larger than $V_{s,f}$, sand-like behavior may be dominant. Lastly, the Gravel-Fines Matrix is defined as when $V_{v,ss}$ is less than $V_{s,f}$, the behavior may be controlled by fine particles. The determination of possible matrix soil structures is summarized in Figure 3.28 and Table 3.4. In addition, the particle interactions of each soil structure matrix are presented in Figure 3.29

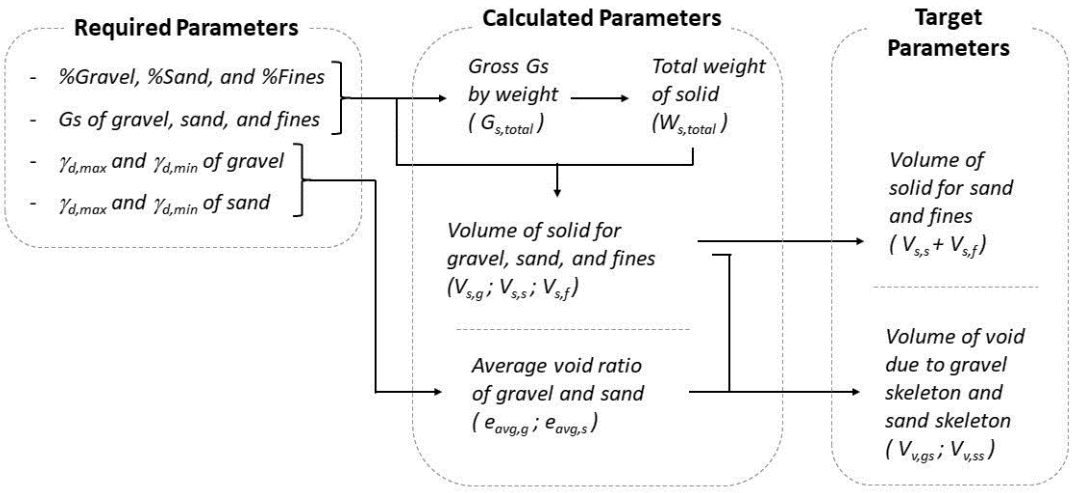

Figure 3.28 Soil structure matrix determination flowchart.

Table 3.4 Summary of soil structure matrix.

When Vs,g, Vs,s, and Vs,f > 0		
$V_{v,gs} \geq V_{s,s} + V_{s,f}$	Interlocked Gravel Matrix	
$V_{v,gs} < V_{s,s} + V_{s,f}$	Gravel-Sand-Fines Matrix	
	$V_{v,ss} \geq V_{s,f}$	Gravel-Sand Matrix
	$V_{v,ss} < V_{s,f}$	Gravel-Fines Matrix
When $V_{s,g}$ = 0; $V_{s,s}$ and $V_{s,f}$ > 0		
$V_{v,ss} \geq V_{s,f}$	Interlocked Sand Matrix	
$V_{v,ss} < V_{s,f}$	Sand-Fines Matrix	
When $V_{s,g}$ and $V_{s,s}$ = 0; $V_{s,f}$ > 0		
Fines Matrix		

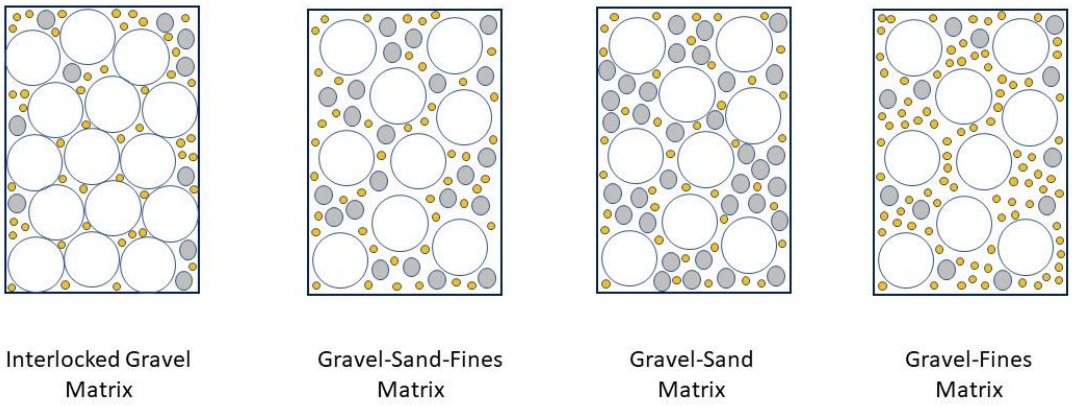

Figure 3.29 Possible soil structure matrix for a composite soil containing gravel, sand, and fines.

The procedure to apply to the proposed method of calculations is detailed here. The wet sieve analysis is performed on undisturbed soil samples to precisely measure the amount of gravel, sand, and fine particles by weight. The specific gravity (Gs) and relative density tests are also performed on pure gravel and pure sand. In this study, the Gs for gravel, sand, and fines is 2.72, 2.73, and 2.63, respectively. The $\gamma_{d,max}$ and $\gamma_{d,min}$ is 15.5 and 13.9 kN/m^3 for pure gravel and 19.2 and 16.0 kN/m^3 for pure sand, respectively. Hence, the average void ratio obtained is 0.819 for gravel and 0.535 for sand. A summary and classification of the soil structure matrix of composite soils containing gravel, sand, and fines is provided in Table 3.5 and Figure 3.30, respectively. Based on the proposed method of calculations and measured soil parameters, Interlocked Gravel Matrix is determined when samples contain gravel content greater than 55 percent by weight. The matrix soil structure would be deemed to have the Gravel-Sand-Fines Matrix if the gravel content is less than 55 percent. It is also found that is Gravel-Fines Matrix if the fines content exceeds two times the sand content. Otherwise, the matrix soil structure is classified as Gravel-Sand Matrix.

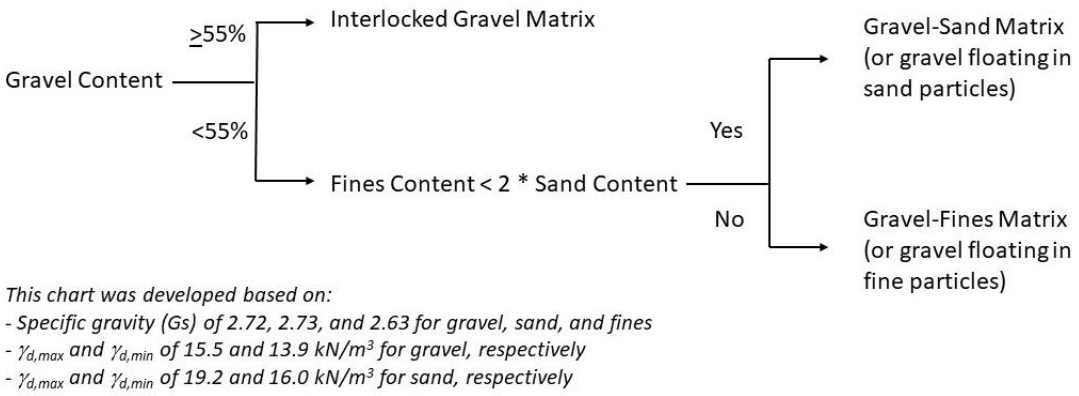

Figure 3.30 Classification of composite soil structure containing gravel, sand, and fines.

The soil structure matrix in Table 3.5, was evaluated for all the gravelly soils tested in this study. The gravelly soils composed of fine content greater than 20 percent are not liquefiable because the matrix structure is described as Gravel-Fine Matrix, which has gravel floating in the fine particles. The Sample G1-Shelby1 fell into this category. However, Sample G1-Shelby3 did not follow the prediction as the sample liquefied, possibly due to its loose state. Other samples having matrix structures described as Gravel-Sand Matrix, having gravel floating in sand particles, liquefied. The matrix structure described as Interlocked Gravel Matrix may also be susceptible to liquefaction, but the loading amplitude and the relative density of the sample should also be considered.

Table 3.5 Summary of matrix soil structures in this study.

Sample ID	%Gravel	%Sand	%Fines	Matrix Soil Structure
G1-Shelby6	49.65	39.05	11.30	Gravel-Sand Matrix
G1-Shelby1	43.69	36.20	20.11	Gravel-Fines Matrix**
G1-Shelby3	45.05	35.66	19.29	Gravel-Fines Matrix
G1-Shelby5	54.20	30.30	15.50	Gravel-Sand Matrix
G1-Shelby8	43.41	40.10	16.49	Gravel-Sand Matrix
G2-Shelby2	37.33	48.89	13.78	Gravel-Sand Matrix
G2-Shelby1	42.80	40.21	16.99	Gravel-Sand Matrix
G2-Shelby5	41.45	42.01	16.54	Gravel-Sand Matrix

G2-Shelby13	38.11	46.43	15.46	Gravel-Sand Matrix
G3-Shelby7	47.87	41.54	10.59	Gravel-Sand Matrix
G3-Shelby4	41.01	42.00	16.99	Gravel-Sand Matrix
G4-Shelby4*	51.35	35.74	12.91	Gravel-Sand Matrix
G4-Shelby3*	56.33	30.38	13.29	Interlocked Gravel Matrix
G4-Shelby5*	57.47	30.30	12.23	Interlocked Gravel Matrix
G4-Shelby7*	47.70	38.30	14.00	Gravel-Sand Matrix

* Reconstituted sample ** No liquefaction

3.7 Conclusions

This study examined the cyclic and post-cyclic behaviors of undisturbed and reconstituted mining waste materials (or gravelly soils) composed of gravel, sand, and fines. For these gravelly soils, the number of cycles to cause liquefaction (N_L) was found to increase as the cyclic resistant ratio (CRR) decreases and the confining effective stress increases. The CRR behavior of gravelly soils in this study is comparable to that of pure sands but that significantly higher than the CRR of pure gravels. For the Vs-base liquefaction susceptibility charts, the chart developed for clean sands do not apply to the gravelly soils tested in this study because the gravelly soils are liquefiable at the $V_{s,1}$ within 260-400 m/s. Prior to liquefaction, the damping values increase as r_u increases. When liquefaction occurs, the damping reaches its maximum value and then starts to reduce, while the shear modulus reduces significantly. The ultimate friction angle of the reconstituted gravelly soils (ϕ'_{ult}) is 51.5 degrees, while the phase transform friction angle (ϕ'_{pt}) is around 34.7 and 41.6 degrees for reconstituted and undisturbed gravelly soils respectively under cyclic loading condition. For the post-cyclic loading, a significant reduction in the effective friction angle (ϕ') is dominant, and it rebounds to be approximately 32.5 degrees at the axial strains between 5 and 20% due to pore pressure dissipation. For the matrix soil structures of the composite soils, containing gravel, sand,

and fines, the soils having Gravel-Fines Matrix described as gravel floating within the fine particles are non-liquefiable, but the soils having Gravel-Sand Matrix described as gravel floating in sand particles are liquefiable. For the matrix structure described as Interlocked Gravel Matrix, it may also be susceptible to liquefaction, but the loading amplitude and the relative density of the sample should also be considered.

CHAPTER 4

TOPIC 2: CENTRIFUGE MODELING OF LIQUEFACTION BEHAVIOR OF GRAVELLY SOILS[1, 2, 3, 4]

---

[1] Sasanakul, I, Ruttithivaphanich, P., & Dejphumee, S. (2022). "Dynamic Characterization of Mine Waste Rock in Centrifuge Testing." *In 10th International Conference on Physical Modelling in Geotechnics, KAIST, Daejeon, Korea.*

[2] Ruttithivaphanich, P., & Sasanakul, I. (2022). "Liquefaction Evaluation of a Gravel-Sand Mixture Using Centrifuge Tests." *In Geo-Congress 2022,* 288-296.

[3] Ruttithivaphanich, P., & Sasanakul, I. (2022). "Centrifuge modeling studies on effects of composition on liquefaction of mine waste rock." *Soil Dynamics and Earthquake Engineering, 160,* 107378.

[4] Ruttithivaphanich, P., & Sasanakul, I. (2022). "Centrifuge Modeling of Fines Content Influence on Liquefaction Behaviors of Loose Gravelly Soils." *Journal of Geotechnical and Geoenvironmental Engineering, ASCE.* (Under Review)

4.1 Introduction and General Motivation

The main objective of the study is to investigate the liquefaction behavior and response of soil mixtures composed of gravel particles using centrifuge modeling. While sandy soil is well-known as a liquefiable material, the liquefaction behavior of gravelly soil remains unclear. It is generally observed that the void ratio and relative density of soils vary with their composition, resulting in an effect on the time required for excess pore water development and dissipation through the soil, influencing liquefaction behavior. Recently, numerous researchers have examined the cyclic response of gravelly soils composed of two-composite materials under homogeneous stress conditions (e.g., Holtz and Ellis 1961, Evan and Zhou 1995, Cubrinovski 2013, Xu et al. 2019, Vallejo and Mawby 2000, Basham and Athanasopoulos-Zekkos 2020, and Gouxing et al. 2021). However, only a research study in centrifuge modeling on gravel-fines mixtures performed by Antonaki et al. (2018) is available. In this study, physical model test using a centrifuge and shaker was utilized to evaluate the liquefaction behavior and cyclic response of the various gravelly soil mixtures under varied shaking amplitudes. Centrifuge modeling testing has advantages in simulating more realistic stress condition and providing a solution to the sample size limitation in conventional laboratory testing. During the shaking, acceleration and pore pressure behaviors are analyzed along the soil profile in the model. Centrifuge modeling data generated in this study provides insight into the dynamic response and liquefaction behavior of gravelly soils closely related to the field conditions.

4.2 Centrifuge Model Preparation

Geotechnical centrifuge modeling with a shake table was utilized to evaluate the liquefaction resistance of various gravelly soil mixtures under different shaking amplitudes. A series of testing was performed at the centrifugal acceleration of 50 g to simulate the level ground soil profile of 7.6 m without an impervious surface layer. A stacked-ring laminar model container was used to reduce the boundary effect in the shaking direction due to allowable soil deformation. A 0.635 mm (0.025") thickness-rubber membrane sheet with a durometer of 40A (medium soft) was used to make a rubber bag to contain the sample with fluid inside of the laminar container. The viscous fluid was prepared to satisfy the seepage and dynamic time scaling by mixing methylcellulose (HPMC) with deaired water using the surface hydration method in accordance with Adamidis and Madabhushi (2015). The Dupont Methocel F50 food gradient (in powder form) was used as methylcellulose in this study. The target viscosity of 50 mPa.s at 20 °C was achieved, corresponding to the centrifugal acceleration at 50 g to simulate the realistic flow rate of the pore fluid. The sample was prepared by mixing the dry soil mixture with viscous fluid at an initial water content of 7%.

The centrifuge model was prepared in a laminar container with the dimensions of 203.2 mm (width) by 279.4 mm (length). To achieve the target dry density, the level-ground model was prepared in eight layers up to the surface, reaching a height of approximately 152.4 mm (7.6 m at prototype scale) using a moist tamping method. During sample preparation, accelerometer and pore pressure sensors were carefully installed in the middle of each soil layer as presented in Figure 4.1. After compaction, the model was flushed by carbon dioxide (CO_2) gas for 20 min in a separated vacuum chamber in order

to push oxygen (O_2) out of the pore space since the CO_2 gas was later able to dissolve in the viscous fluid. The saturation process was then performed with viscous fluid outside the centrifuge to achieve fully saturated state (as presented in Figure 4.2). After the model was completely saturated, the model was carefully installed on the centrifuge shaker as presented in Figure 4.3. All external sensors were installed along the side of laminar container and on the shake table. Signal cables were securely attached to appropriate locations and connected to the national instrument data acquisition (NI-DAQ) system. Additionally, the centrifuge beam was manually balanced before running the test to maintain stability during the spinning.

At the beginning of the test, the model was started spinning by gradually increasing the rotational speed rate of 4 g/min until centrifugal acceleration reached 50 g (as presented in Figure 4.4). The model was then consolidated by self-weight at the target g-level until the excess pore pressure was fully dissipated, meaning the end of primary (EOP) consolidation had been passed. During consolidation, viscous fluid was allowed to drain to the surface of the model. Then, shaking motion was applied underneath the model by using a 1-Hz uniform sinusoidal motion for 40 shaking cycles. Pore pressure dissipation was then monitored for approximately 30 minutes after the shaking event to allow for complete pore pressure dissipation and to accurately assess the volumetric strain after the test. After the model was spun down, a post-test investigation of the model was conducted to observe physical changes regarding, model settlement, lateral deformation, sensor locations, final water content, and change of soil composition in each layer.

4.3 Experimental Plan

Three variables are evaluated in this study including shaking amplitude, fines content, and grain size distribution. The material tested is a product of mine waste rock composed of coarse crushed material that covered a range of particle sizes from 1.9 cm (3/4 inches) gravel to fine sand particles and non-plastic fine particles. Visual assessment was performed in accordance with Muszynski and Vitton (2012), the roundness factor (R) and sphericity factor (S) of the gravel and sand particles were within the range of 0.27-0.31 and 0.60-0.80, respectively. The material shape is classified as subangular and is light brownish gray (2.5Y-6/2) in color. Four specimens that were composed of different amounts of gravel, sand, and non-plastic fines were mixed to achieve different compositions and grain size distributions for the study, as provided in Figure 4.5. These specimens are called G40S48F12, G50S38F12, G50S50F00, and G70S30F00. Letter G, S, and F represents gravel, sand, and fines, respectively, and the numbers represent the corresponding % by weight. The composition of soil specimens was selected to evaluate the impact of gravel (i.e., G70S30F00 and G50S50F00) and sand (i.e., G40S48F12 and G50S38F12), and to evaluate the influence of fines content (i.e., G50S38F12 and G50S50F00). Table 4.1 presents a summary of index properties for these specimens. The initial void ratio of each soil was carefully selected based on the initial relative density (D_r) to achieve a range of initial soil stiffnesses prior to dynamic centrifuge testing. The initial void ratio was intended to create specimens at very loose states to mimic the loose state of mine waste dump. The specimens were consolidated under 50-g gravitational acceleration in the centrifuge, and the void ratio prior to shaking varied from 0.49 to 0.68. The increase in the D_r was approximately 6-12% after consolidation. Compressibility of the models with

fines was higher than the models without fines. Table 4.1 summarizes the D_r and void ratio for each specimen at different stage of testing. Centrifuge bender element tests were performed to evaluate the shear wave velocity of these specimens after the 50-g centrifuge consolidation in accordance with Sasanakul et al. (2022), and the result of normalized shear wave velocity ($V_{s1} = V_s \cdot \left(\frac{100}{\sigma'_{v0}}\right)^{0.25}$) was calculated from the curve fitting function presented in Fig. 4.6. Shear wave velocities agree reasonably well with the function, $V_s = C\,(\sigma'_v)^{0.25}$, where C is a constant influenced by several factors, including, but not limited to, particle shape, gradation, and index properties. Overall, the average V_{s1} for the entire depth of model of all four specimens were very close, ranging from 117 to 128 m/s as presented in Table 4.1. The variation of permeability of these soils was observed due to the influence of fabric, as well as the initial void ratio. Specimens G50S50F00 and G70S30F00 have permeability that is approximately an order of magnitude higher than specimens G40S48F12 and G50S38F12.

For the effect of soil composition, these models were utilized to perform centrifuge modelling tests at an approximately the same amplitude of 0.27 g. For the effect of shaking amplitude, G50S50F00 and G50S38F12 samples were used with three respective centrifuge models prepared for each sample. Three models of each sample were subjected to three different maximum shaking amplitudes: 0.20, 0.27, and 0.40 g. The summary of testing program for centrifuge modeling for this topic is presented in Table 4.2

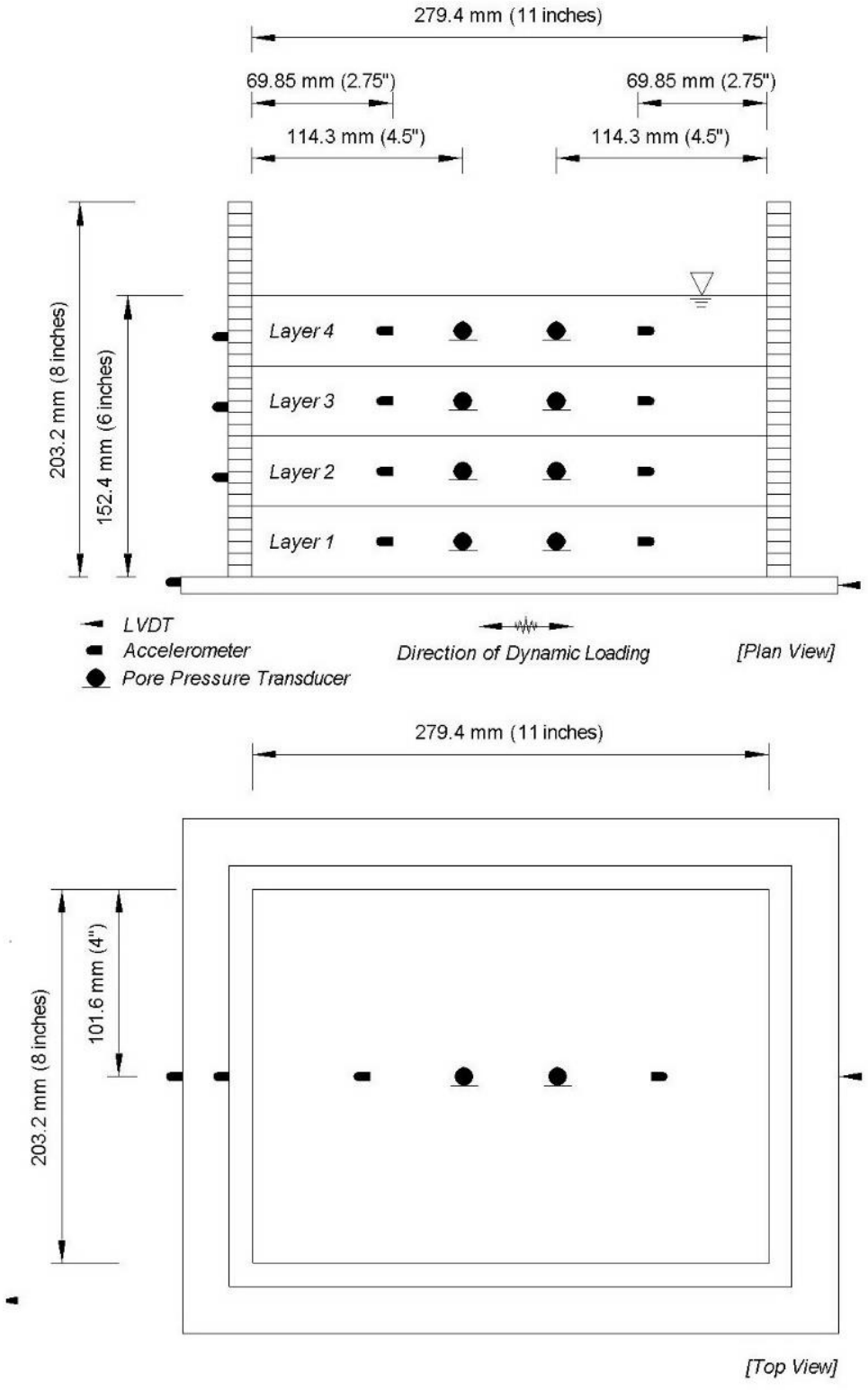

Figure 4.1 Model dimension and location of sensors in a laminar container.

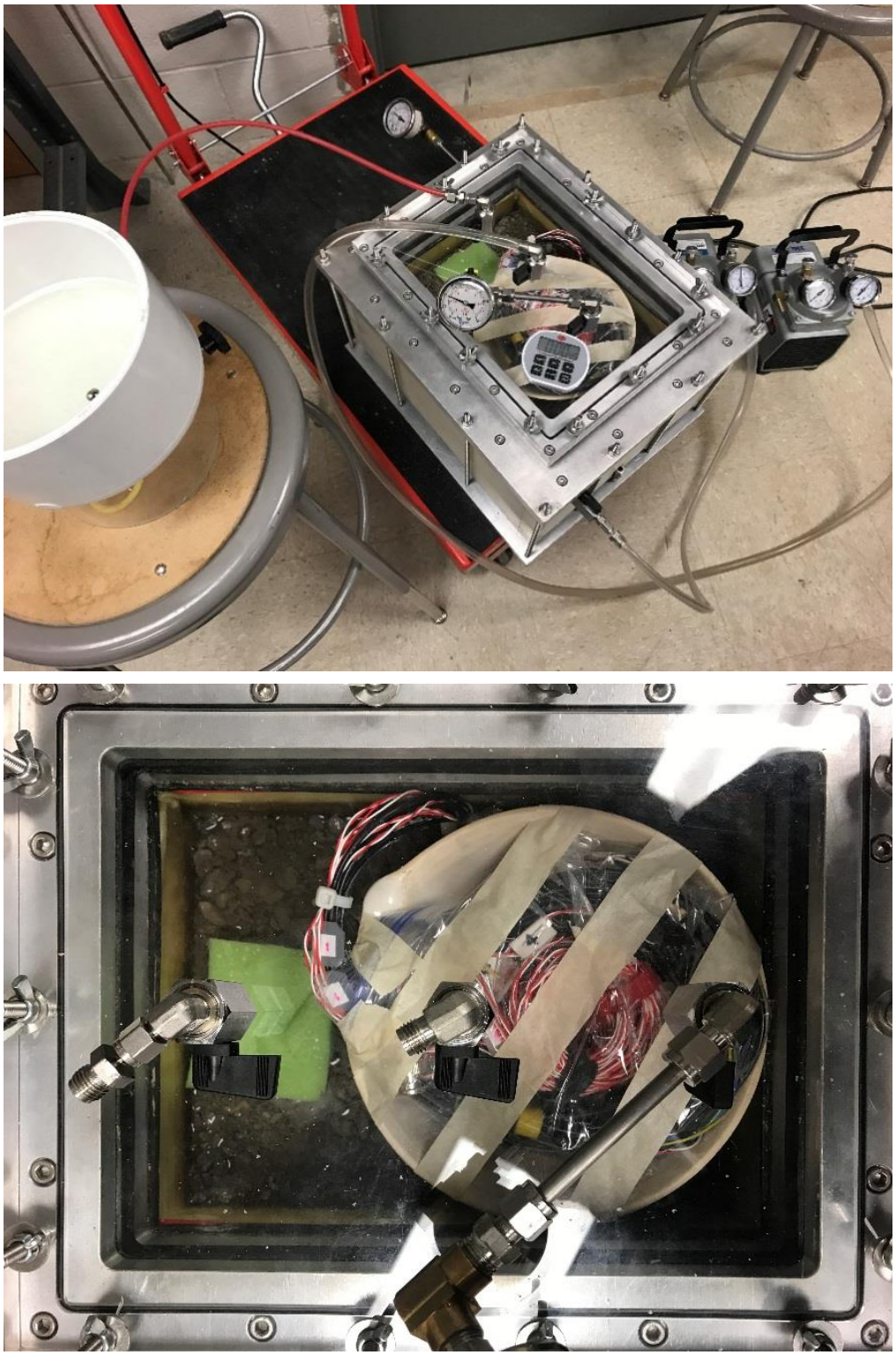

Figure 4.2 Saturation process of specimen inside laminar box.

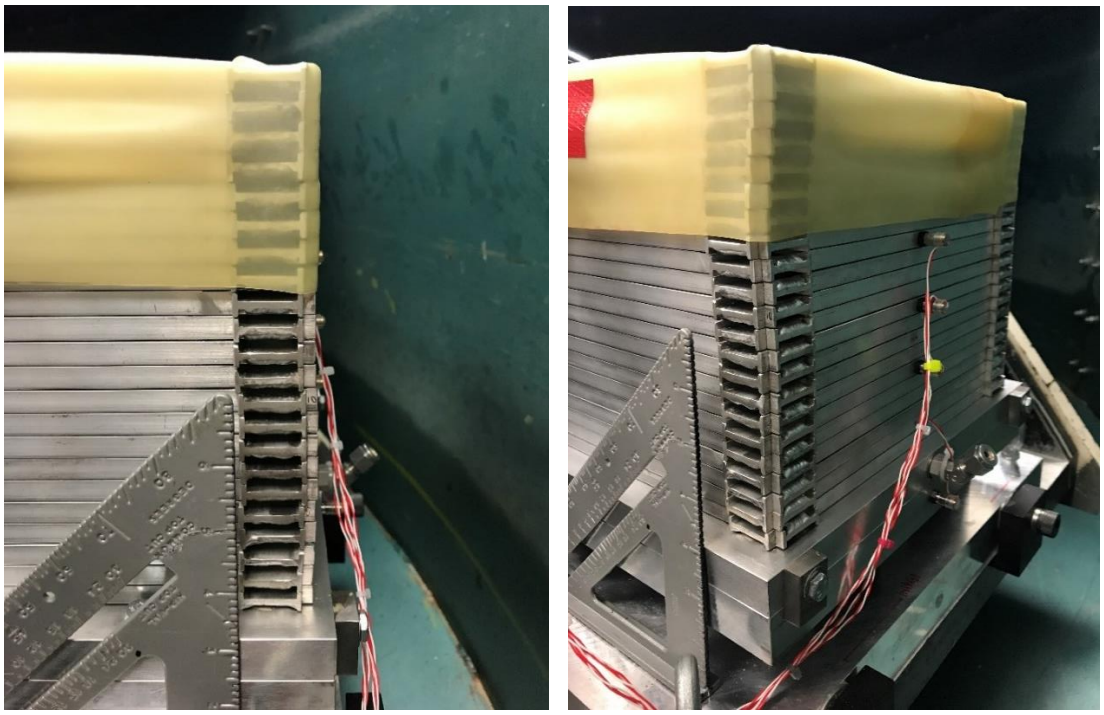

Figure 4.3 Initial condition of laminar box on centrifuge shaking table.

Figure 4.4 In-flight monitoring (a) centrifuge spinning and (b) top view of the model.

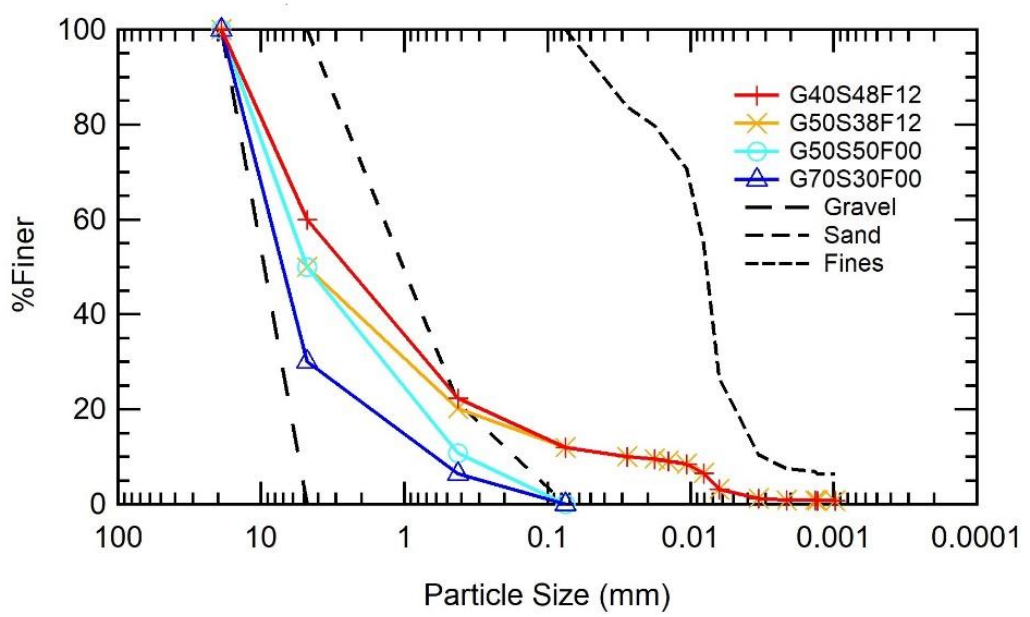

Figure 4.5 Grain size distribution of all soil specimens.

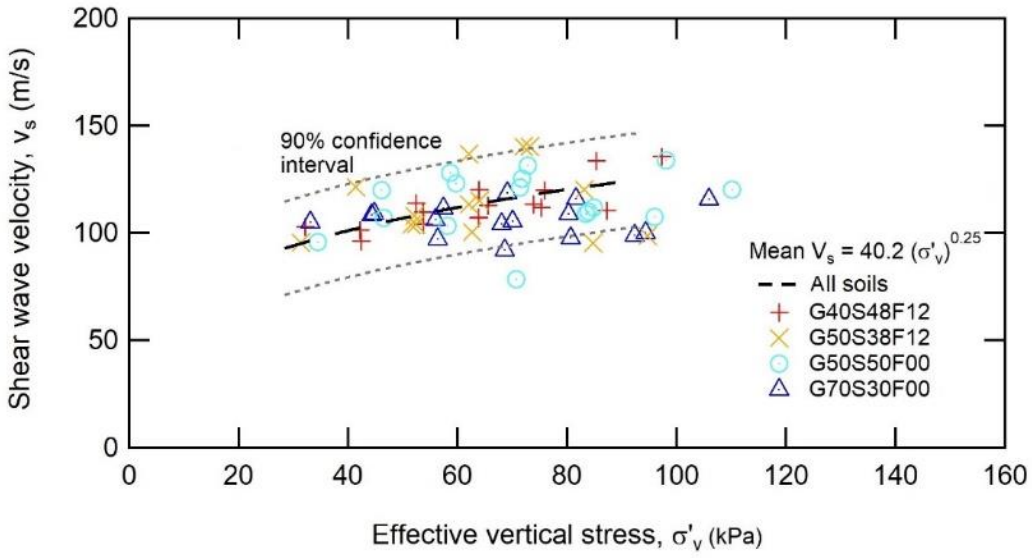

Figure 4.6 Variation of shear wave velocity and effective vertical stress.

Table 4.1 Summary of material properties before shaking event.

Sample ID	Gravel-Sand-Fines Mixing Ratio (%)	Cu[a]	Cc[a]	USCS[b]	Gs[c]	Initial Condition				After Consolidation at 50 g				After test
						γ_d (kN/m^3)	K_{20}[d] (cm/s)	Void ratio	Dr[e] (%)	γ_d (kN/m^3)	Void ratio	Dr[e] (%)	V_{s1} (m/s)	Dr[e] (%)
G40S48F12	40 – 48 - 12	173	3.8	SP-SM	2.70	17.57	7.9×10^{-4}	0.53	10.0	17.85	0.49	20.8	127	64.3
G50S38F12	50 – 38 - 12	226	5.6	GP-GM	2.76	17.00	8.6×10^{-4}	0.59	1.1	17.39	0.56	13.4	128	49.1
G50S50F00	50 – 50 - 00	15	0.7	GP/SP	2.75	17.00	1.2×10^{-2}	0.58	10.2	17.15	0.57	15.8	125	41.1
G70S30F00	70 - 30 - 00	15	4.5	GP	2.73	15.77	1.2×10^{-2}	0.72	10.0	15.92	0.68	17.5	117	50.2

[a.] ASTM D422 and D6913M-17, [b.] ASTM D2487-17, [c.] ASTM D854-00, [d.] ASTM D2434-19, [e.] ASTM D4253-16e1, and D4254-16

Table 4.2 Summary of Testing Program.

Sample ID	Estimated Base Shaking Amplitude (g)
G70S30F00	0.27
G50S50F00	0.40
	0.27
	0.20
G50S38F12	0.40
	0.27
	0.20
G70S30F00	0.27

4.4 Results, Analysis and Discussion

The effect of soil composition, the effect of shaking amplitude of the model without fines, and the effect of fines content in soil mixtures were discussed in this section as presented in 4.4.1 to 4.4.3, respectively.

4.4.1 Effect of Soil Composition

4.4.1.1 Observed Horizontal Acceleration and Pore Pressure Time Histories

The results of the measured horizontal acceleration and excess pore pressure time histories for all four models are depicted in Figures. 4.7 and 4.8, respectively. The base shaking motion for each model is also presented in both figures. As mentioned, and observed, the base shaking motion is consistent for all four tests. Different level of reduction in horizontal acceleration near the top half of the model was found for all soil models which indicates the loss of strength that could lead to the initiation of liquefaction. For all soil models, horizontal time histories show numerous negative spikes where the records are not symmetrical, and negative amplitude is higher than positive amplitude. The negative amplitude can be as large as 5-8 times higher than the positive amplitude in some cases, and it can occur at the beginning of shaking, as well as toward the end of shaking. It is clear that the impact of negative spikes is considerably lower at the deepest depth (Layer 4) of all models. Model G70S30F00 showed fewer negative spikes in the acceleration time histories than other models, and very high acceleration was observed near the surface.

Different criteria of liquefaction have been suggested in literature (e.g., Ishihara 1993, Wu et al. 2004). In this study, the initiation of liquefaction is considered when the excess pore pressure ratio, r_u, approaches 0.90 ($r_u = u_e / \sigma'_v$, where u_e is excess pore pressure

and σ'_v is initial effective vertical stress). It can be observed that the r_u increased as the shaking started and continued. It is clear that the liquefaction occurred at the top layer of Model G50S48F12 and Model G50S48F12. It is noted that r_u more than 1 (above 100%) is possible due to the increase in the mean total stress in the centrifuge models (Boulanger and Idriss 2004, Hughes and Madabhushi 2018, Kutter et al. 2020, Manandhar et al. 2021). In Model G50S50F00, the r_u values increased progressively and reached above 0.90 at the top three layers. Due to the fact that the maximum r_u of 0.96 was observed at the second layer of Model G50S50F00, liquefaction likely occurred at the top three layers of this model as similar behaviors observed by Ruttithivaphanich and Sasanakul 2022. In Model G70S30F00, the maximum r_u value of 0.71 was observed at the second layer, therefore the model did not fully liquefy. Table 4.1 presents a summary of r_u values, and their corresponding number of cycles observed at each soil layer. Model G40S48F12 liquefied within 3-8 cycles, while Model G50S38F12 liquefied within 19-40 cycles. It is interesting to observe that the r_u at the surface of Model G50S50F00 only reached a maximum 0.91 at the end of shaking (40 cycles) while the r_u value at the second layer reached 0.96 at the 22^{nd} shaking cycles. Similar behavior was observed in Model G70S30F00 where the r_u observed at the second layer is higher than that of the surface. It is possible that the development of excess pore water pressure at the surface stopped due to high permeability of these specimens, hence they were under partially drained condition. In Model G50S50F00 and Model G70S30F00, in which the soil specimens have no fines content, dissipation of pore water pressure was also observed during shaking, particularly at deeper depths. While the pore pressure development in models with fines content (G50S48F12 and G50S38F12) stabilized for the entire shaking duration.

Close inspection of Figures 4.7 and 4.8 indicates that correlations exist between negative spikes in acceleration and excess pore water pressure ratio. When the r_u, approached a value of 0.70, a relatively high amplitude of negative spikes was observed. In Layer 3 (4.76 m), for instance, the peak of the negative spike was observed at approximately the 7^{th} cycle of Model G40S48F12 when the excess pore pressure ratio reached 0.93. For the same layer, the peak of the negative spike was observed at approximately the 11^{th} cycle of Model G50S50F00 when the excess pore pressure ratio reached 0.92. This observation is similar to the dilative behavior of dense sand during liquefaction (e.g., Balakrishnan and Kutter 1999, Elgamal et al. 2005, Kutter et al. 2018, Manandhar et al. 2021). Comparing the behavior between these two models, Model G40S48F12 liquefied at a lower number of cycles and presented a relatively lower amplitude of negative spikes than Model G50S50F00 when the r_u value was high with the exception of the top layer. This implies that Model G50S50F00 exhibited more dilative behavior than Model G40S48F12. When comparing the two models with fines content (G40S48F12 and G50S38F12), the characteristics of the acceleration time histories are similar, but the development of excess pore pressure showed some differences, as it appears to be slightly higher in Model G40S48F12. This result is to be expected because Model G40S48F12 has more sand than gravel by weight when compared to G50S38F12. Therefore, the permeability is slightly lower, due to differences in void size and particle distribution. Model G40S48F12 is also slightly denser than Model G50S38F12. After the end of shaking, the dissipation of the pore pressure occurred much more rapidly in Model G7030F00. In contrast, the excess pore pressure in Model G40S48F12 dissipated at the slowest rate.

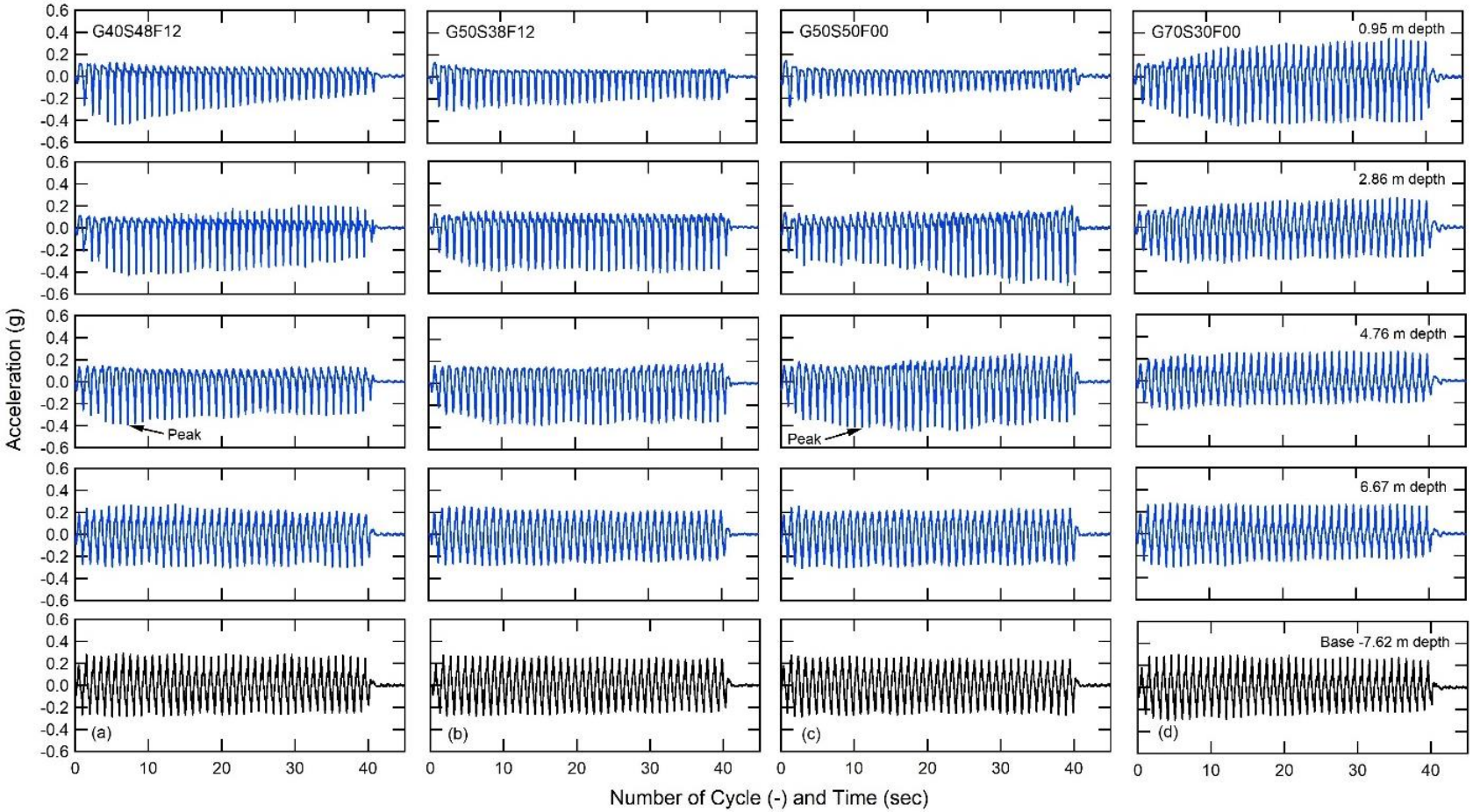

Figure 4.7 Acceleration time histories at 0.95, 2.86, 4.76, and 6.67 m depths for: (a) G40S48F12, (b) G50S38F12, (c) G50S50F00, and (d) G70S30F00 samples.

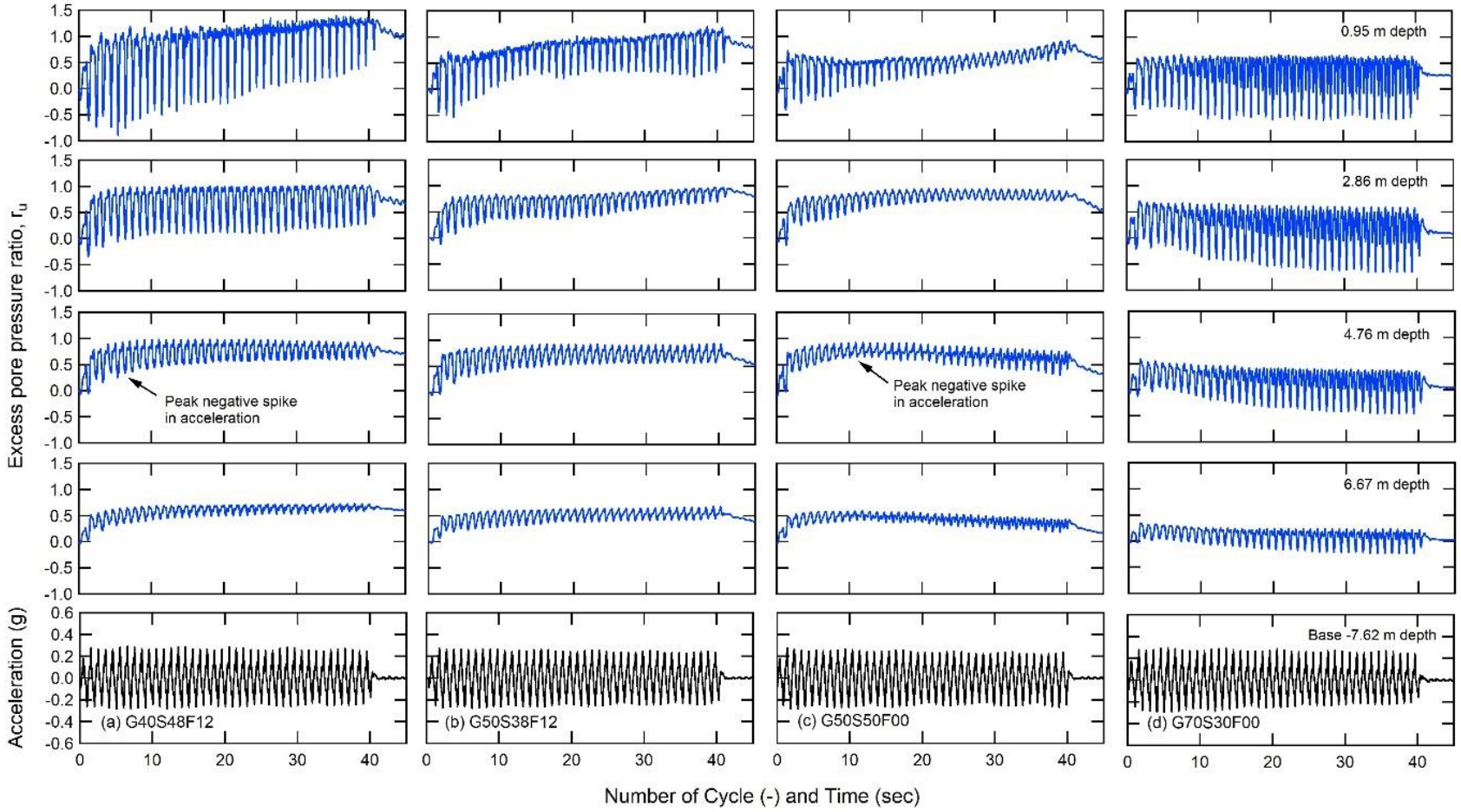

Figure 4.8 Excess pore pressure ratio at 0.95, 2.86, 4.76, and 6.67 m depths for: (a) G40S48F12, (b) G50S38F12, (c) G50S50F00, and (d) G70S30F00 samples.

4.4.1.2 Pore Water Pressure Development and Dissipation

Figure 4.9 presents the development of pore water pressure with depth at different numbers of cycles. This figure presents more evidence of liquefaction in the top 3 m of Model G40S48F12 and the top layer of Models G50S38F12 and G50S50F00. The rate of pore pressure development increases as the depth decreases. In other words, the pore pressure developed faster at lower effective stress. The impact of composition on the pore pressure behavior can be clearly observed in this figure. Pore pressure developed and stabilized in Model G40S48F12 and Model G50S38F12. Meanwhile, pore pressure developed rapidly and dissipated quickly in Model G50S50F00 and Model G70S30F00, as seen in Figure 4.10. The base shaking motion of approximately 0.27 g was not strong enough for Model G70S30F00 to develop excess pore pressure that was high enough to reach full liquefaction in all layers. Nevertheless, relatively high excess pore pressure ($r_u \approx$ 0.65) was developed near the surface due to very low effective stress. It is interesting to observe that for models with the same gravel content (G50S38F12 and G50S50F00), the excess pore pressure ratio reached roughly the same maximum value, but Model G50S50F00 required a fewer number of cycle due to its higher permeability. When comparing the two models with the different ratios of gravel and sand (G40S48F12 and G50S38F12), the rate of pore pressure development, as well as the maximum value of excess pore pressure, were higher for Model G40S48F12, due to the higher amounts of sand, as discussed previously. More than 90% of the excess pore pressure in all models dissipated within 200 seconds after shaking.

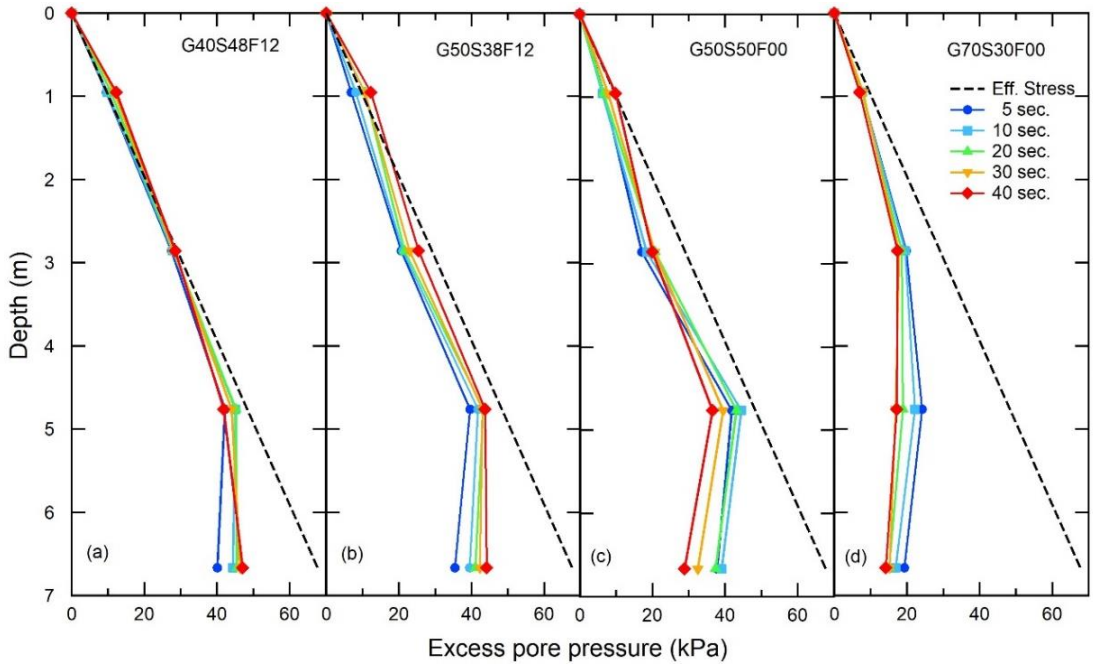

Figure 4.9 Development of excess pore pressure during shaking for:
(a) G40S48F12, (b) G50S38F12, (c) G50S50F00, and (d) G70S30F00 samples.

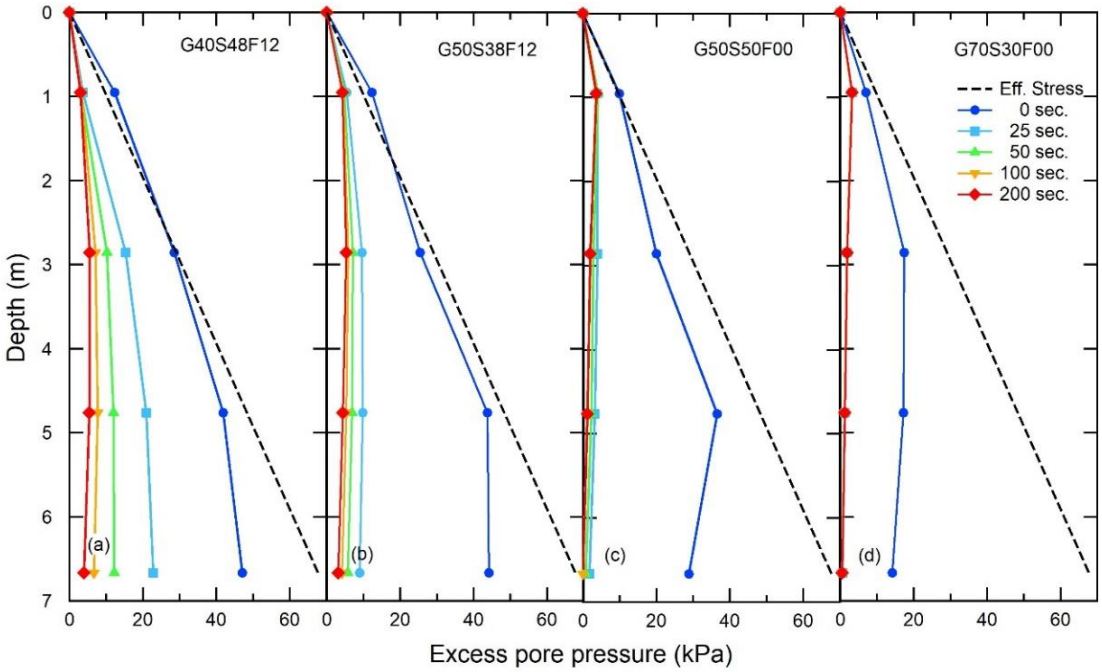

Figure 4.10 Excess pore pressure dissipation after shaking for:
(a) G40S48F12, (b) G50S38F12, (c) G50S50F00, and (d) G70S30F00 samples.

4.4.1.3 Normalized Shear Stress or Cyclic Stress Ratio

Cyclic shear stresses induced at each depth in level-ground soil models during shaking can be calculated using the measured acceleration time histories, following the assumption of the shear beam condition proposed by Zeghal and Elgamal 1994, Zeghal et al. 1995, and Brennan et al. 2005. The acceleration data were filtered using a 4^{th} order Butterworth filter with a band pass frequency of 0.1 to 7 Hz to eliminate unexpected noise. The cyclic stress ratio (CSR), which is the normalization of cyclic shear stress initiated in each layer with the initial vertical effect stress, is evaluated and presented in Table 4.3. An example of the normalized shear stress at effective vertical stress of approximately 30 kPa and 70 kPa are presented in Figure 4.11. CSR values ranging from 0.19 to 0.26 for all four soils were observed at the bottom depth (effective stress of approximately 70 kPa) and remained fairly uniform for all 40 cycles. This layer is emphasized because the pore pressure development is relatively low and therefore, less impact of negative spikes. For the shallow depths, the CSR reduced to lower values and was asymmetric with loading cycles. The observation implied that a significant reduction in shear stress occurred when soil is loaded in one direction, and conversely, a significant increase in shear stress occurred when soil is loaded in another direction. As discussed previously, the observed negative spikes in acceleration time histories (as well as shear stresses) are an indication of dilative behavior. It implies that more void space is being created (volume expansion) while shearing. As shown in Figure 4.11 for the effective stress of approximately 30 kPa, all models with the exception of Model G70S30F00 exhibited a reduction in CSR with number cycles. An increase in value of CSR with number of cycles was clearly observed for Model G70S30F00 suggesting that the soil dilated during shearing. It is important to

note that the CSR values obtained from centrifuge tests may not be comparable to the values observed from cyclic simple shear or cyclic triaxial tests because of the self-weight stress condition reproduced in centrifuge models associated with more complex phenomena, such as complex wave propagation, flow of water, pore pressure development and distribution, and volume change due to partial drainage.

4.4.1.4 Cyclic Resistance Ratio

The dependence of cyclic strength on the number of loading cycles of different soils is further evaluated in Figure 4.12. The CSRs required to reach a value of r_u greater than 0.9 for a specific number of cycles, known as the cyclic resistance ratio (CRRs), are compared. There is no data for Model G70S30F00 because the maximum r_u of this model is 0.7. According to Figure 4.12, there is a small variation in CRRs for the other three soil models; the values range from 0.17 to 0.20. Based on the soil composition of these models, it appears that the amount of sand contributes more to the triggering of liquefaction. In other words, the models with more sand liquefied faster than the models with less sand, as observed for Models G40S48F12 and G50S50F00 in comparison with Model G50S38F12. However, when comparing the models with a similar amount of sand (G40S48F12 and G50S50F00), the fines content in Model G40S48F12 decreases the soil permeability resulting in an increase in excess pore pressure development.

Table 4.3 Summary of key parameters observed during liquefaction.

Soil layer	Depth (m)	G40S48F12						G50S38F12					
		σ'_v (kPa)	CSR[a]	γ_{sa}[b] (%)	$r_{u,max}$	N[c]	N_L[d]	σ'_v (kPa)	CSR[a]	γ_{sa}[b] (%)	$r_{u,max}$	N[c]	N_L[d]
Layer 1	0.95	10.72	0.17	1.23	1.40	36	3	10.55	0.20	1.21	1.20	39	19
Layer 2	2.86	32.26	0.18	1.49	1.02	14	5	31.77	0.19	1.60	0.96	37	40
Layer 3	4.76	53.69	0.19	1.53	0.98	11	8	52.88	0.19	1.84	0.95	39	39
Layer 4	6.67	75.23	0.20	1.74	0.73	36	-	74.09	0.21	1.86	0.67	40	-
Soil layer	Depth (m)	G50S50F00						G70S30F00					
		σ'_v (kPa)	CSR[a]	γ_{sa}[b] (%)	$r_{u,max}$	N[c]	N_L[d]	σ'_v (kPa)	CSR[a]	γ_{sa}[b] (%)	$r_{u,max}$	N[c]	N_L[d]
Layer 1	0.95	10.35	0.21	1.23	0.91	40	-	9.57	0.30	1.47	0.66	8	-
Layer 2	2.86	31.16	0.17	1.62	0.96	22	19	28.82	0.24	1.61	0.71	2	-
Layer 3	4.76	51.86	0.17	1.78	0.92	11	-	47.96	0.25	1.66	0.59	2	-
Layer 4	6.67	72.67	0.19	2.01	0.59	12	-	67.20	0.26	1.72	0.34	2	-

[a.] average from first 3 cycles, [b.] average from 40 cycles, [c.] at maximum r_u, and [d.] at r_u of 0.95

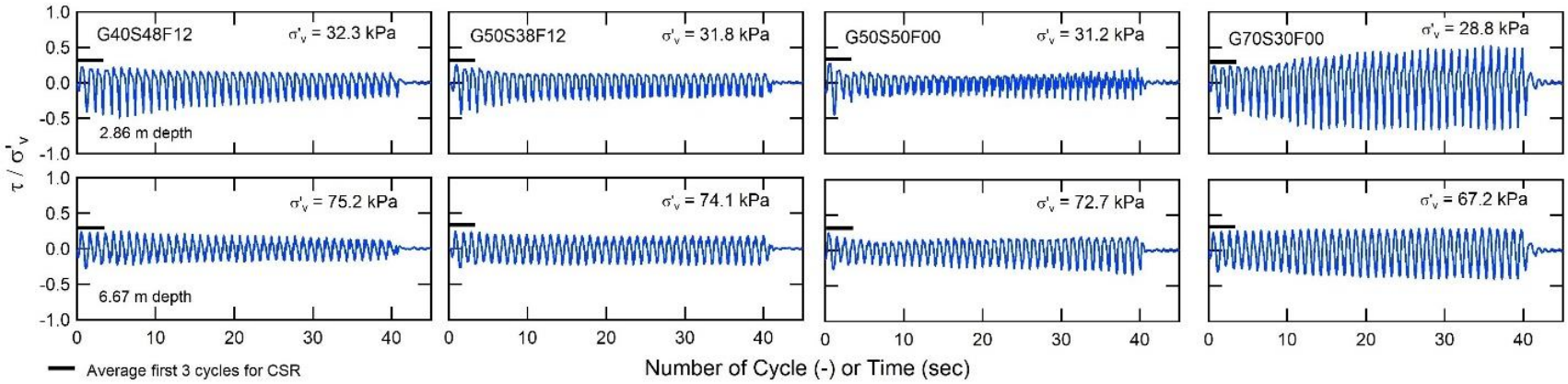

Figure 4.11 Cyclic stress ratio with the number of cycles.

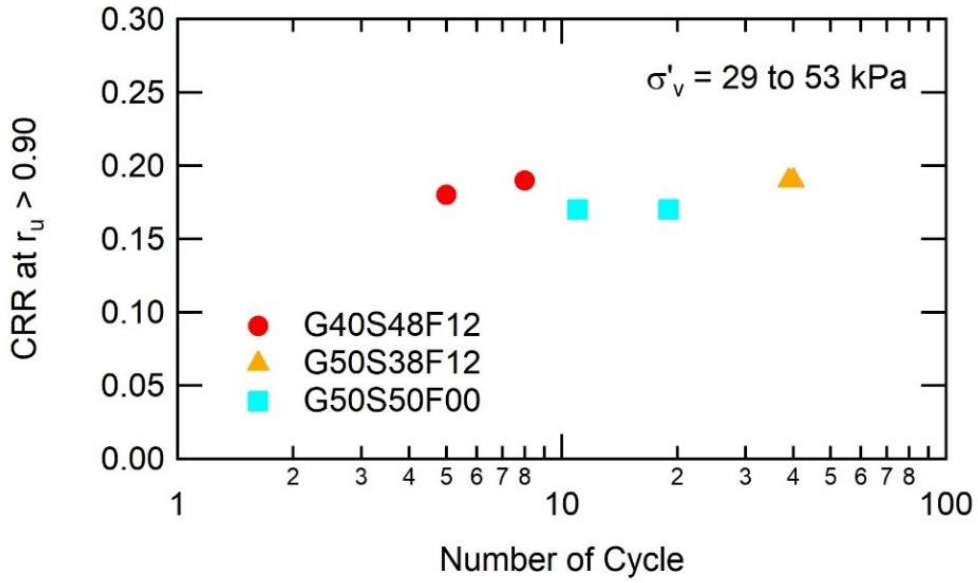

Figure 4.12 Cyclic resistance ratio of soils at $r_u > 0.90$.

4.4.1.5 Shear Stress-Strain Behavior

Cyclic shear strain was calculated using the acceleration time histories, which is a similar approach to calculating shear stress (Zeghal et al. 1995). The baseline adjustment process was performed to eliminate permanent displacement that occurred during shaking. Lateral displacement, which was measured using an LVDT that was located at the base of the laminar container, was used to verify the accuracy of the calculated displacement. Overall, the dynamic shear strain levels generated in all centrifuge model tests are very close and ranged from 1.2% to 2.0% for all depths as presented in Table 4.3. Shear stress-strain behaviors are presented in Figure 4.13 for Models G40S48F12 and G70S30F00. These models were selected for analysis because Model G40S48F12 represented a liquefied model, while Model G70S30F00 represented a non-liquefied model. Moreover, the stress-strain behaviors of Models G50S38F12 and G50S50F00 were similar to Model G40S48F12, while the behavior of Model G70S30F00 was different.

Figure 4.13 presents the degradation of the stress-strain loop from different number of cycles at different depths in the model. In both models, the shear modulus at the 1st cycle reduced to less than 1% of the maximum shear modulus (G_{max}) estimated from the shear wave velocity of the soil prior to shaking which is to be expected since the maximum shear strain is approximately 2%. The damping value was approximately 30% at the 1st cycle for both models. In Figure 4.13(a), the stress-strain loop of Model G40S48F12 degrades significantly as the number of cycles increases, and the banana-shaped stress-strain loop was observed. Dilative behavior, where the shear stress decreases in one direction and increases in the other direction, was observed when the number of cycles increased and is clearer at the shallow depths. The degradation of stress-strain loops resulted in a reduction

in shear modulus with the number of cycles. Damping fluctuated with the number cycles as a significant decrease in values (~1%) was observed during shaking then followed by an increase in values toward the end of shaking. The number of cycles associated with the lowest value of damping is not consistent for each soil layer as it could possibly be impacted by the amplitude of dilative spikes in acceleration time histories and the effective stress of the soil. Nevertheless, the accurate damping estimation is difficult especially when the stress-strain loop is highly distorted. Since the strain levels in these tests are high, and the damping behaviors at low to medium strains are not available, it is unclear if damping was reduced due to the dilative effect, as discussed by Elgamal et al. (2005). In Figure 4.13(b), the stress-strain loop of Model G70S30F00 also degraded but was relatively less than that of Model G40S48S12. Since this model did not liquefy, the banana-shaped stress-strain loop was not observed. However, the undrained dilatancy effects on shear stress-strain behavior was clearly observed. The distortion of the stress-strain loop also indicates a phase transformation of this specimen. As shown in Figure 4.13(b) for the top layer (effective stress of 9.6 kPa), the shear modulus also decreases with the number of cycles, but the damping increases significantly. For the other three layers, a reduction in shear modulus also occurred, however, the damping during shaking fluctuated, both decreasing and then increasing. This is similar to Model G40S48S12, but the lowest damping value of approximately 18% during the first 8 cycles of shaking was found for each layer which is higher than the lowest damping value (~1%) observed in Model G40S48S12. It is interesting to observe that for these layers, the damping value at the end of shaking is very similar to the initial value.

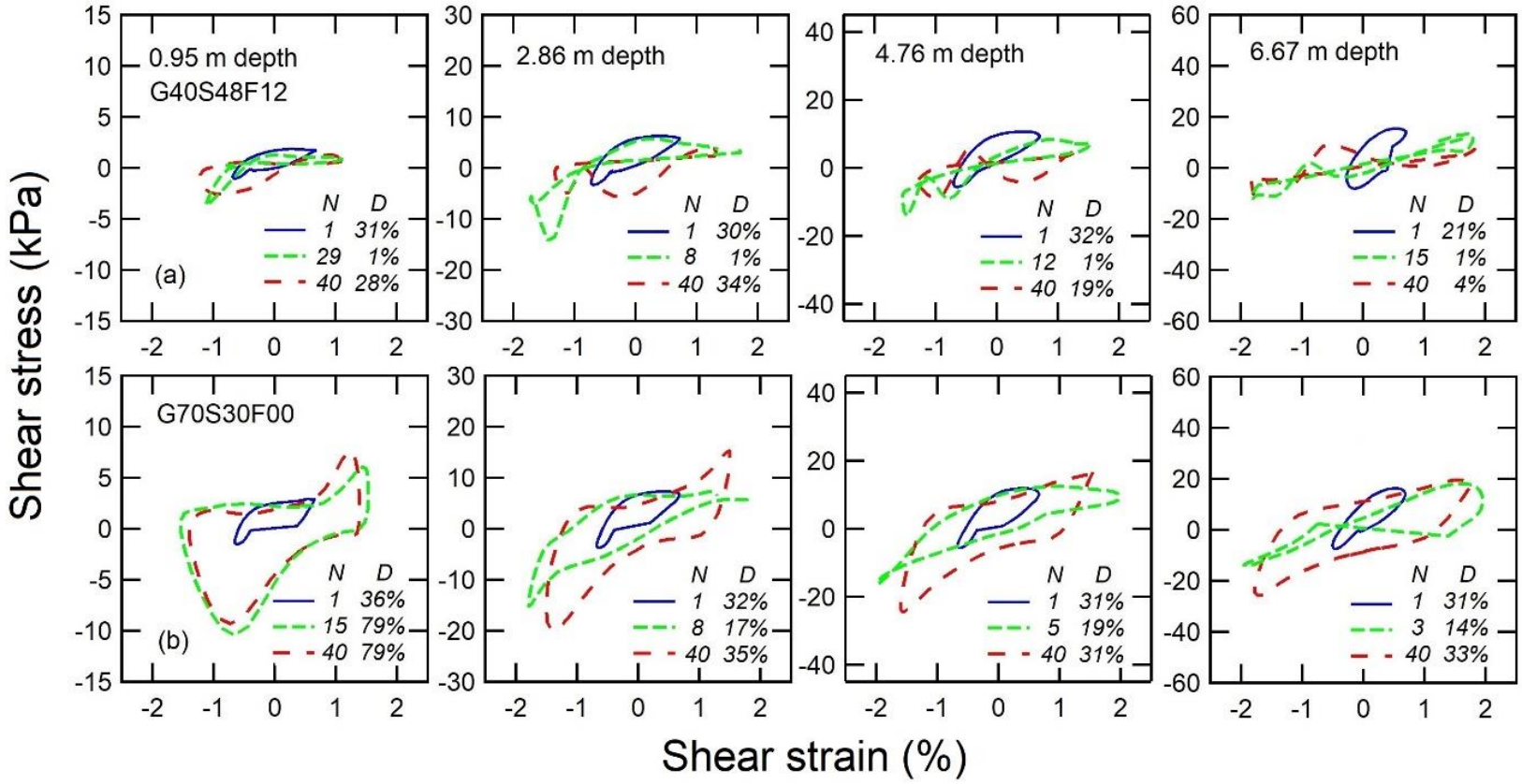

Figure 4.13 Selected shear stress-strain behaviors at different depths and number of cycles for model: (a) G40S48F12 and (b) G70S30F00.

4.4.1.6 Cumulative Lateral Displacement and Volumetric Strain

Cumulative lateral displacement along the profile of the laminar container that was observed after the completion of the test was used to calculate permanent shear strain, as shown in Figure 4.14(a). The largest displacement was found in Models G50S50F00 and G40S48F12, with the maximum displacement of nearly 1.5 m, corresponding to the shear strain of approximately 20% at the ground surface. Model G50S38F12 exhibits slightly less displacement than the previous two models. Model G70S30F00 shows the least displacement of approximately 0.5 m and shear strain of less than 10% at the ground surface, which is considered high even though no liquefaction occurred in this model. It must be noted that Model G70S30F00 has the lowest shear wave velocities and is relatively less dense than other models. Closer inspection of the composition suggests that with higher sand content, larger lateral deformation was observed. This finding may be due to liquified sand dominating the consequence of liquefaction. Additionally, the lateral displacements observed in this study are consistent with those reported by Antonaki et al. (2018), as the cumulative lateral displacements at the surface of mildly sloping waste rock material were between 0.3 and 2 m for the shaking amplitude of 0.25 g. Moreover, the incremental change in permanent shear strain for the level ground waste rock material tested in this study is approximately 0.25-0.5% per cycle, which is comparable to the values of 0.7-1.2% for gentle sloping, medium dense sand observed in centrifuge model tests by Elgamal et al. (1996).

Settlement records from the LVDT at the top-center of the model surface, as well as post-test investigation after the completion of the test, are presented in Figure 4.14(b). The most settlement was observed at the surface and estimated volumetric shear strains

due to shaking and post-shaking consolidation are presented in Figure 4.14(b). The D_r of all models after the test shown in Table 4.1 indicated that the density of soil changed from loose to medium dense state. The volumetric strain of Model G70S30F00 and G50S50F00 is approximately 5%, while the volumetric strain of Model G40S48F12 and G50S38F12 is approximately 8%. These values are higher than the typical values observed in sand but are consistent with the centrifuge modeling study of waste rock material by Antonaki et al. (2018). High volumetric strain observed in this study may be due to a combination of the very low D_r of soils and a very low effective stress near the surface of the models. The very low effective stress at the surface resulted in less particle interlocking. The impact of D_r and share wave velocity on volumetric strain was found for sands (Yoshimine et al. 2006 and Yi 2010) and gravelly soils (Hubler et al. 2017). However, due to the similarity in the shear wave velocity of these soils and no clear correlation between the D_r of soil prior to shaking, the observed volumetric strain in this study appears to be influenced by composition, specifically fines content. Post-test investigation shows that for the models with fines content (G40S48F12 and G50S38F12), the fine particles moved upward to the surface during liquefaction. Therefore, more fines were observed at the surface. As a result, more settlement occurred at the surface due to the movement of fines through the soil matrix. For Model G70S30F00, the settlement was observed to be higher than for Model G50S50F00 because the soil has higher void ratio as presented in Table 4.1.

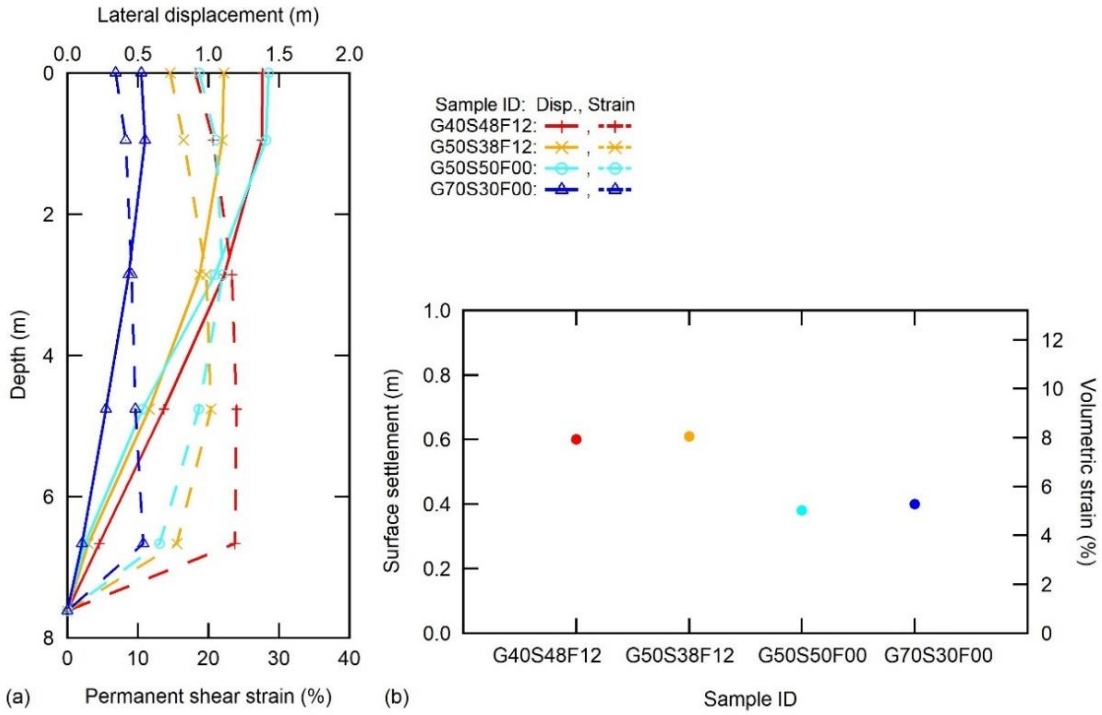

Figure 4.14 Post-test investigation for (a) lateral displacement and permanent shear strain along the soil depth, and (b) settlement and volumetric strain at ground surface.

4.4.2 Effect of Shaking Amplitude on Soil Mixtures

4.4.2.1 Acceleration and Pore Pressure Time Histories

When the base shaking began, the time histories of horizontal acceleration and excess pore water pressure were simultaneously recorded at multiple depths in the centrifuge model. The excess pore pressure, Δu, at each depth corresponding to an effective vertical stress, σ_v', was used to evaluate the time histories of the pore water pressure ratio, r_u ($r_u = \Delta u / \sigma_v'$). The results were plotted in Figures 4.15 and 4.16 for Models GF00 and GF12, respectively. The time histories of acceleration show positive and negative values as the model experienced cyclic shearing due to a uniform sinusoidal shaking motion. A symmetrical response in the acceleration was typically found in the soil that exhibited contractive behavior. Under cyclic shearing conditions, the soil began to lose stability

under the influence of particle interlocking and eventually exhibited inelastic soil behavior, resulting in an asymmetrical spike in the acceleration. As shown in Figures 4.15 and 4.16, the negative value of acceleration (or negative spike) was higher than the positive value due to dilative behavior, as discussed in previous physical modeling studies (e.g., Zeghal and Elgamal 1994, Balakrishnan and Kutter 1999, Elgama et al. 2005, Kutter et al. 2018, Antonaki et al. 2018, Manandhar et al. 2021). In addition, the negative spike could be due to the time delay for the soil particles to move backward after being pushed forward, resulting in a high impact force between soil particles. This behavior is likely related to the large downward spikes in the pore pressure ratio. As shown in the results for both materials and different shaking amplitudes, the large downward spike in the pore pressure ratio corresponds with the negative spike in the acceleration. While the spike in dilation was dominant and the excess pore pressure significantly built up, the positive values of acceleration degraded, particularly near the top half of both models, as a result of initial liquefaction. The degradation of acceleration led to the reduction in shear stress, as evidenced by the loss of strength and stiffness, which is discussed later in the paper. Full liquefaction may be considered whenever the excess pore pressure ratio (r_u) is high enough (e.g., r_u exceeds 0.95), as it is close to the zero effective stress condition and/or a significant reduction in the acceleration, as discussed in previous research (e.g., Ishihara 1985, Hryciw et al. 1991, Ishihara 1993, Zoraoaoet and Vucetic 1994, Elgamal et al. 1996, Zeghal et al. 1999, Wu et al. 2004, Manandhar et al. 2021, Ruttithivaphanich and Sasanakul 2022).

For the shaking amplitude of 0.19 g, dilative behavior was observed in Model GF00 at a deeper depth (about 2.86 m) compared to a depth of 0.95 m for Model GF12. For the base shaking amplitude of 0.27 and 0.40 g, dilative behavior was apparent from the surface

to a depth of 4.76 m in both models. The behavior was found within the first few cycles for Model GF12, but for Model GF00, the dilatancy was observed toward the end of the shaking event. For both models, the dilation spikes in acceleration are triggered when r_u approaches 0.6. Although the timing is different, the effects of fines content on the magnitude of the dilatancy behavior were not clear when comparing the behaviors for Model GF12 and Model GF00. In contrast, Gu et al. (2022) found that sand with a fines content of 10% exhibits more dilative behavior than clean sand. In this case, it could be possible that the gravel content may have more dominant effects on the soil's dilative behavior. For the low shaking amplitude of 0.19 g, no degradation of the acceleration was observed in either model, but the degradation of the acceleration was more clearly observed at the top of Model GF00 than that of Model GF12 for the higher shaking amplitudes (i.e., 0.27 and 0.40 g). The degradation corresponded to an increase in excess pore pressure. In addition, an increase in the amplitude of acceleration after the 20^{th} cycle was observed in Model GF00, which implies that the soil regained strength toward the end of the shaking. Loss and regain of shear strength and stiffness are discussed further in the later section of this paper.

The behaviors of r_u for both models shown in Figures 4.15 and 4.16 include a rapid increase of pore pressure within the first few cycles and, in some cases, a dissipation of pore pressure during shaking. The dissipation of excess pore pressure was clearly observed for the 0.19 g shaking amplitude for all model depths but as the shaking amplitude increases to 0.27 and 0.40 g, the excess pore pressure increased progressively toward the end of the shaking event, particularly at the top half of the models. Some dissipation of excess pore pressure was observed at the bottom half of Model GF00. Relatively higher and faster

dissipation of pore water pressure during the shaking was anticipated for Model GF00 based on the higher permeability of the soil. Based on the r_u values, soil liquefaction occurred in both models at various depths for all levels of shaking amplitude. The r_u value greater than 1 was found at the top soil layers in the shaking amplitudes of 0.27 and 0.40 g. This behavior has been observed and discussed in previous centrifuge modeling research and is associated with the temporary increase in the total vertical stress in the centrifuge models (Boulanger and Idriss 2004, Hughes and Madabhushi 2018, Kutter et al. 2020). For Model GF12, values of r_u higher than 0.95 were observed up to a depth of 0.95 m for the 0.19-g shaking amplitude and to a depth of 4.76 m for the 0.27-g and 0.40-g shaking amplitudes. For Model GF00, values of r_u higher than 0.95 were observed at similar depths for the shaking amplitudes of 0.19 and 0.40 g. However, for the shaking amplitude of 0.27 g, a lower value of r_u was observed near the surface (0.95 m) than at 2.86 m. Because of the high permeability, the soil at the surface was likely under a partially drained condition; hence, it was not possible to develop high excess pore pressure, and the r_u at the shallower depth is less than the r_u at the depths below due to the influence of this partially drainage. However, this observation was not apparent in the models that experienced shaking amplitudes of 0.19 and 0.40 g. The maximum values of r_u were much lower than 0.8 at the deeper depths in both models. Downward spikes in the excess pore pressure ratio were also observed and appeared to be more apparent in Model GF12 than in Model GF00 for all base shaking amplitudes. The magnitude of the downward spikes in the excess pore pressure ratio increased as the shaking amplitude decreased. A larger magnitude of downward spikes was observed at shallower depths where the effective stress was low. This observation is comparable to the dense sand behavior discussed by Manandhar et al.

(2021). Based on the overall observations of the acceleration and pore pressure time histories for both models, soil liquefaction occurred at only the top 0.95 m for the shaking amplitude of 0.19 g, while up to 4.76 m liquefied for the shaking amplitudes of 0.27 and 0.40 g.

4.4.2.2 Pore pressure development and dissipation

The rate of pore pressure development during shaking is presented in Figure 4.17 for both models. Due to the difference in permeability of approximately 1 order of magnitude, some difference in pore pressure development can be observed, particularly at lower shaking amplitudes and deeper depths. Pore pressure development in Model GF12 appears to be slightly slower than that of Model GF00. For the highest shaking amplitude of 0.40 g, the pore pressure built up nearly simultaneously for both models. For Model GF00, the dissipation of pore pressure was clearly observed at the bottom half of the model (deeper than 4 m) for all shaking amplitudes, while the same dissipation behavior was only observed in Model GF12 for the shaking amplitude of 0.19 g. Regardless of the rate of pore pressure development, the maximum pore water pressure for both models was relatively close for all shaking levels. As discussed in the previous section, the r_u value was observed to be lower than 0.8 at the deeper depths for both models at all shaking amplitudes. It is possible that there was an upward dissipation of pore pressure in the bottom soil layer, resulting in a reduction in excess pore pressure at the depths deeper than 5 m, as shown in Figure 4.17.

The rate of pore pressure dissipation after the end of shaking is presented in Figure 4.18 for both models. As expected, the pore pressure in Model GF12 required more time

to dissipate than Model GF00 due to its lower permeability, which is a consequence of the presence of fine particles. A similar observation was observed by Gu et al. (2022). Nevertheless, after 200 seconds, the dissipation of pore pressure toward the bottom half of both models is nearly 100% complete, while approximately 80% of the pore water pressure dissipation was completed at the top half of the models. In comparison between the two materials, the rates of pore pressure development and dissipation appear to behave in accordance with the permeability of the material. In other words, the development and dissipation were slower in Model GF12 than in Model GF00 because of its lower permeability. In comparison between the different shaking amplitudes, the higher shaking level caused a higher buildup of pore pressure, thus it took longer to dissipate.

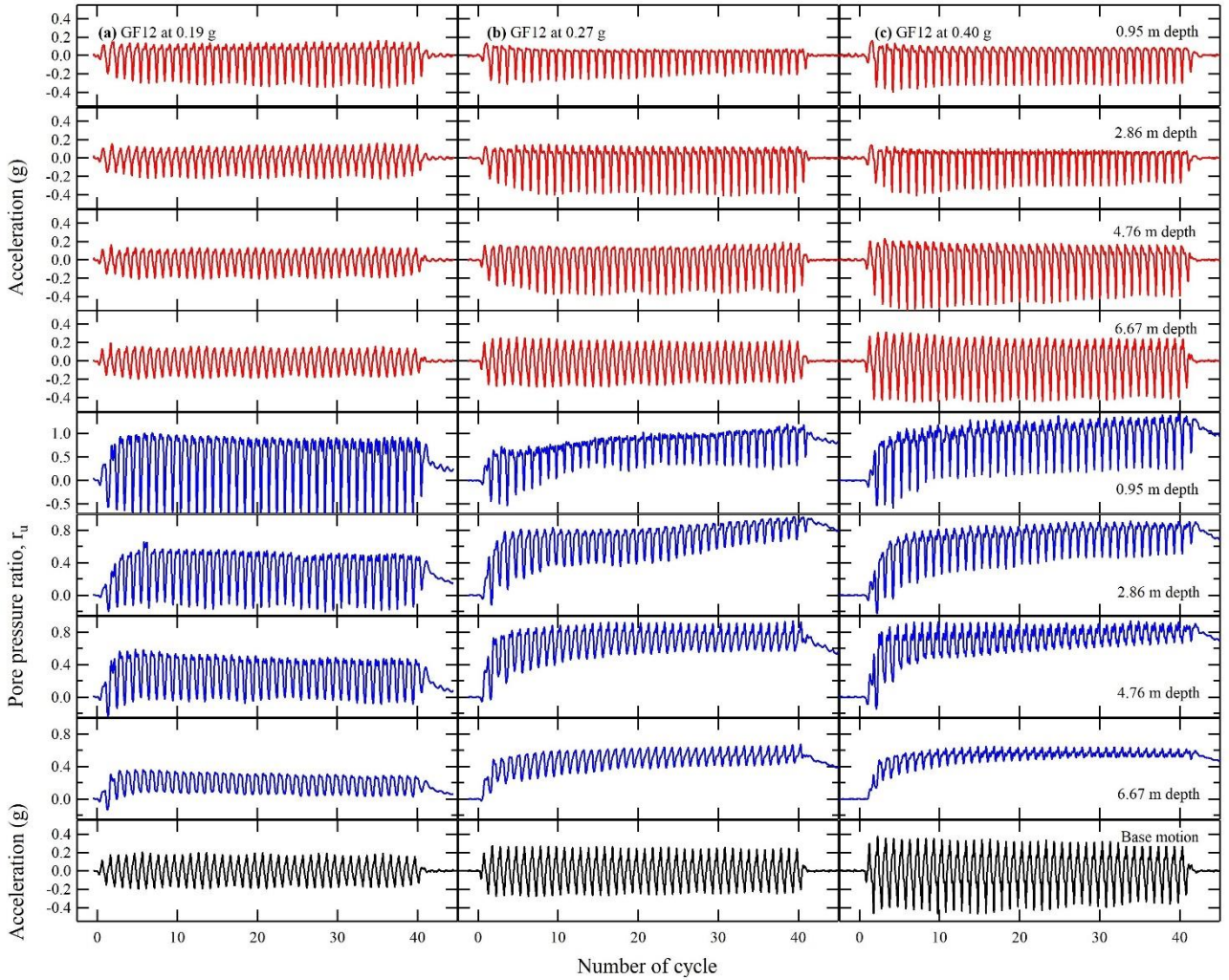

Figure 4.15 Acceleration time histories and pore pressure development for Model GF12 at base shaking acceleration of: (a) 0.19 g, (b) 0.27 g, and (c) 0.40 g.

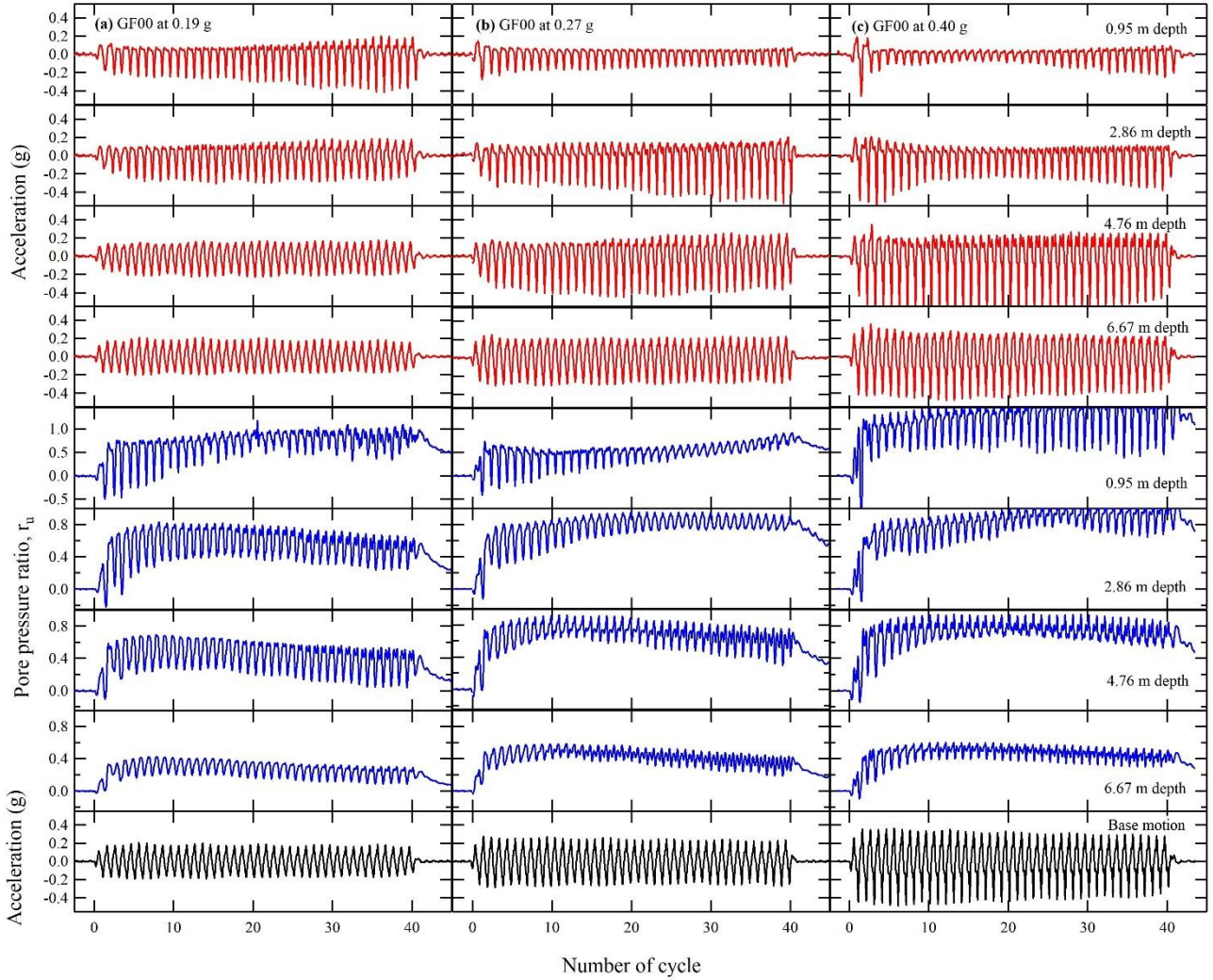

Figure 4.16 Acceleration time histories and pore pressure development for Model GF00 at base shaking acceleration of: (a) 0.19, (b) 0.27, and (c) 0.40 g.

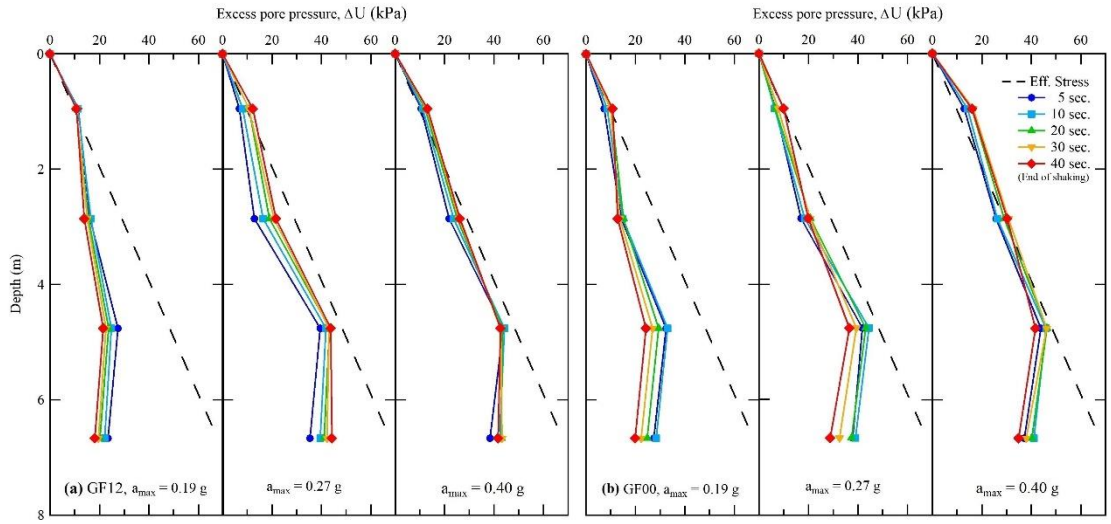

Figure 4.17 Pore pressure development along the depth during shaking.

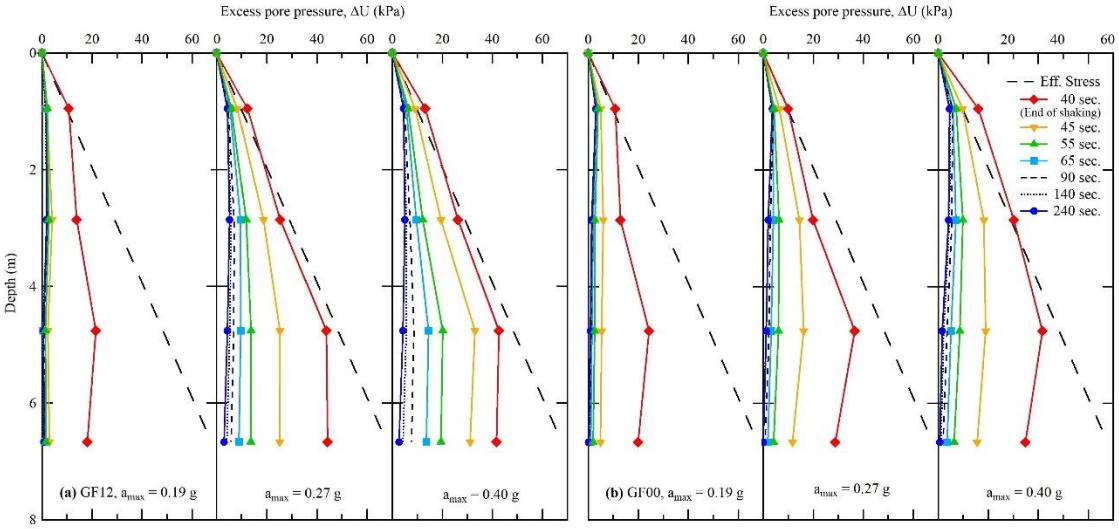

Figure 4.18 Pore pressure dissipation along the depth after end of shaking.

4.4.2.3 Cyclic Stress Ratio

Shear stresses and shear strains were calculated using the filtered acceleration time histories in accordance with Zeghal et al. (1995, 1999). The measured acceleration time histories were filtered using a 4th order Butterworth filter with a band-pass frequency between 0.1 and 7 Hz in prototype scale. The cyclic stress ratio (CSR), a normalization of

shear stress with effective vertical stress, was obtained at different depths in the model. Similar to the acceleration time histories, negative dilation spikes were observed, particularly at shallow depths, as high excess pore pressure buildup occurred during shaking. As a result, the representative CSR of the model was defined at the bottom of the model where the dilation spike was minimal. This assumption is based on the idealization of a 1-D shear beam condition subjected to dynamic loading used by Zeghal et al. (1999), Abdoun et al. (2020), Ni et al. (2020), and others. Figure 4.19 presents the CSR and shear strains obtained at the deepest model depth of 6.7 m for shaking amplitudes of 0.40 and 0.19 g. It is shown that the amplitude of cyclic shear strain increases as the shaking amplitude increases. When comparing results between Models GF12 and GF00, the shear strain amplitudes were close. For the high amplitude shaking of 0.40 g, a shift in shear strain behavior was observed in the first 10 seconds of the shaking event. The reason is unclear, but it could likely be influenced by the large displacement of the soil that occurred immediately at the beginning of the shaking event, although this behavior does not appear in the displacement time history at the base of the shaker.

The representative value of CSR was obtained by averaging CSR amplitudes of all cycles shown in Figure 4.19 for all shaking amplitudes. The corresponding number of cycles when $r_u \geq 0.85$ was selected based on the availability of data and plotted in Figure 4.20. This figure shows the variation in the cyclic resistance ratio (CRR at $r_u \geq 0.85$) with respect to the number of cycles for the range of effective stress below 53 kPa. Scattered data were observed for Model GF00, but it shows that the CRR has the potential to decrease as the number of cycles increases. For Model GF12, the trend is different, as it appears that a very insignificant change in CRR occurred with the number of cycles. It is noted that this

observation is limited to low effective stress conditions (about 53 kPa), and more data is needed for higher effective stress conditions. Based on Figure 4.20, the estimated $CRR_{M=7.5}$ (cyclic resistance ratio induced by 15 uniform cycles of shear stress) is approximately 0.22 for both models. These values are comparable to a $CRR_{M=7.5}$ of 0.20 for dense sand obtained from a series of cyclic triaxial tests at the effective confining stress of 100 kPa reported by Ni et al. (2020). However, Hubler et al. (2017) reported a $CRR_{M=7.5}$ of 0.12 for dense uniform gravels, which was obtained from a series of cyclic simple shear tests at an effective vertical stress of 100 kPa. The same study found no effect of relative density on the $CRR_{M=7.5}$ value.

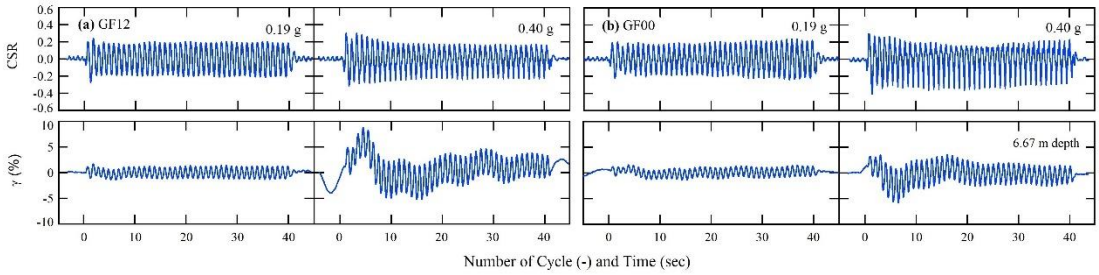

Figure 4.19 Normalized shear stress during shaking event for shaking amplitudes of 0.19 and 0.40 g.

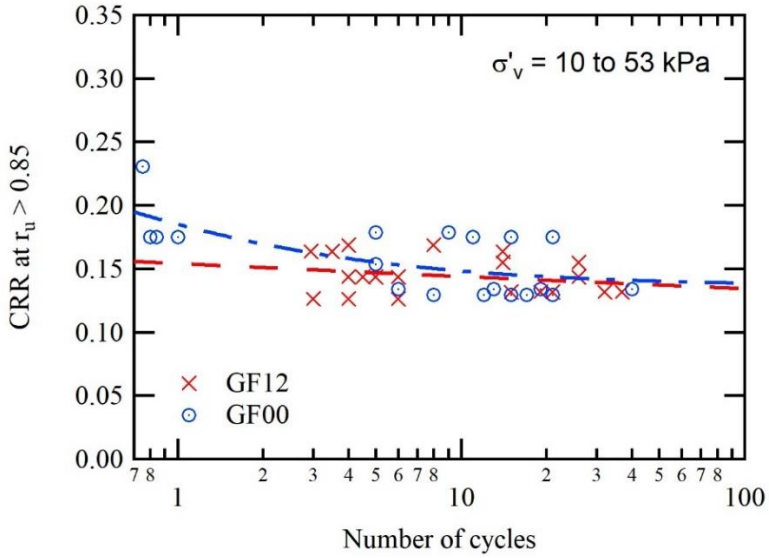

Figure 4.20 Variation of cyclic stress ratio with number of cycles.

4.4.2.4 Shear Stress-Strain Behavior at the First Cycle

The shear stress-strain loop at different depths for the first cycle was considered in this study, as presented in Figure 4.21. A distortion of the loops was apparent when the shaking amplitude was higher than 0.27 g. More distortion occurred at shallower depths, which was consistent with the dilation spikes observed in the acceleration time histories. Cyclic shear stress and strain were further assessed for dynamic soil properties, including the shear modulus (G) and damping (D), as presented in Table 4.4. The shear modulus increased as effective stress increases, and the shear modulus decreased as cyclic shear strain (γ) increased, as expected. Based on the maximum shear modulus (G_{max}), calculated from the V_s measured using the bender elements presented in Table 4.1, normalized shear modulus (G/G_{max}) values of less than 0.1 were observed in all layers of both models. The G/G_{max} values corresponded with cyclic shear strain amplitudes ranging from 0.4 to 1.7% for the first cycle of shaking. Zeghal et al. (1999) observed comparable G/G_{max} values for the same range of strains. For the same range of shear strains, damping (D) values of 20 to 30% were observed in all layers for both models, with the exception of 42% damping found at the bottom of Model GF12. Overall, Model GF12 has slightly higher damping than Model GF00 for higher shear strains (i.e., shaking amplitudes of 0.27 and 0.40 g)

4.4.2.5 Shear Modulus Reduction and Damping Curves

Variations in G/G_{max} and D values with γ obtained from the bottom half of the centrifuge models for all shaking levels and the entire shaking duration were plotted with the G/G_{max} and damping curves estimated from a series of resonant column tests on Sample GF00 performed at 3 different effective vertical stresses in Figure 4.22 as suggested by Sasanakul et al. (2022). Curve fitting parameters based on the modified hyperbolic function (Stokoe et al. 1995) are provided in the figure for a reference. As shown in Figure 4.22, the shear modulus reduced significantly at high shear strain levels (approximately 0.4 to 5%)

for all shaking levels, and the G/G_{max} values were slightly higher than the reference curve. When comparing G/G_{max} values between the GF12 and GF00, the values were close. It is noticeable that the G/G_{max} at Layer 4 of Model GF00 (effective stress of 73 kPa) was slightly higher than that of Layer 3 (effective stress of 52 kPa) for the same model. The damping data for both models were very scattered and did not match with the reference curve. The maximum damping values of 50 and 30% were found for Model GF12 and Model GF00, respectively. The progressive changes of shear modulus and damping with the number of cycles are discussed later in the paper.

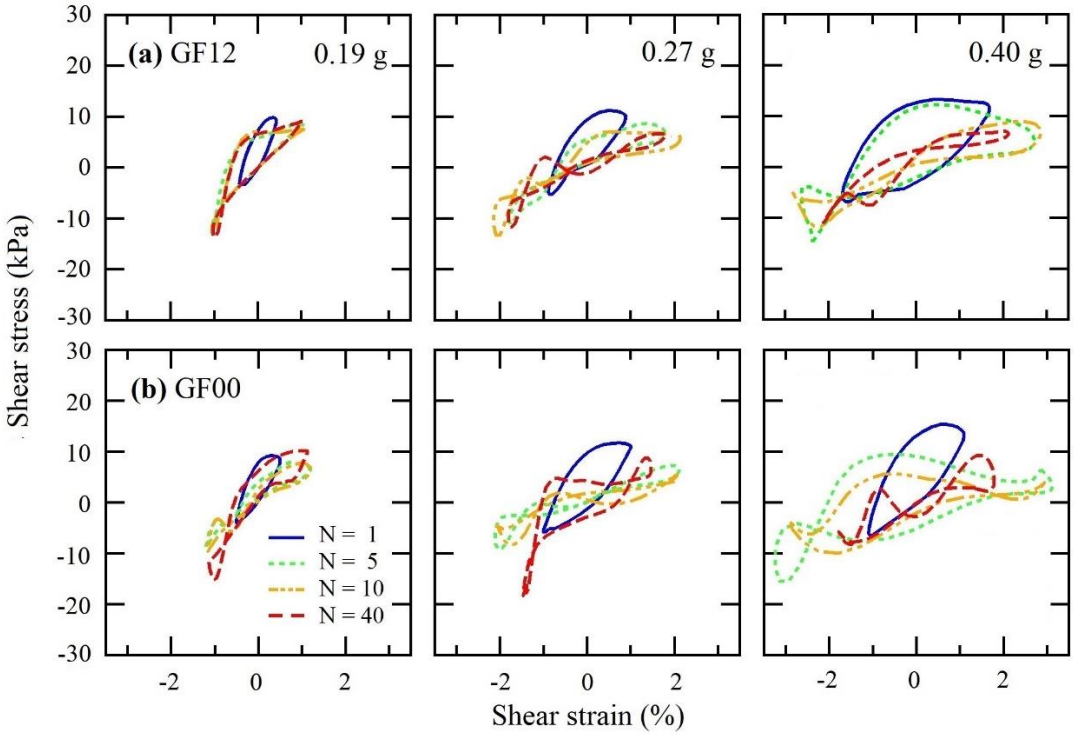

Figure 4.21 Shear stress-strain behavior at the first shaking cycle of Models: (a) GF12, and (b) GF00.

Table 4.4 Summary of dynamic soil properties at the first shaking cycle.

Sample ID	Shaking Amplitude			0.40 g				0.27 g				0.19 g			
	Layer#	Depth (m)	σ'_v (kPa)	G (kPa)	D (%)	γ (%)	r_u	G (kPa)	D (%)	γ (%)	r_u	G (kPa)	D (%)	γ (%)	r_u
GF12	Layer 1	0.95	10.6	162	30	1.18	0.63	194	28	0.81	0.47	431	28	0.37	0.34
	Layer 2	2.86	31.8	400	28	1.41	0.30	528	29	0.87	0.47	969	25	0.37	0.13
	Layer 3	4.76	52.9	473	36	1.69	0.53	817	30	0.89	0.50	1398	27	0.42	0.19
	Layer 4	6.67	74.1	633	42	1.71	0.30	1481	26	0.69	0.27	1315	25	0.59	0.09
GF00	Layer 1	0.95	10.4	199	26	1.06	1.00	262	23	0.78	0.41	330	27	0.41	0.15
	Layer 2	2.86	31.2	532	24	1.10	0.47	618	23	0.88	0.38	833	26	0.45	0.28
	Layer 3	4.76	51.9	823	31	1.09	0.42	805	25	1.00	0.48	1167	27	0.50	0.31
	Layer 4	6.67	72.7	1261	29	1.00	0.23	1210	29	0.89	0.26	2040	21	0.41	0.25

4.4.2.6 Effect of Shear Strain on Pore Pressure Development

To assess shear-induced pore pressure, plots between pore pressure ratios (r_u) and cyclic shear strain amplitudes at the bottom half of both models are presented in Figure 4.23. At each loading cycle, the maximum excess pore pressure (Δu) was obtained, and consequently, the corresponding r_u value was calculated for each stress-strain loop. A correlation between the r_u value and the shear strain level was established, as shown in Figure 4.23. It was observed that r_u initially increased with shear strain and reached its maximum value at a shear strain of approximately 2%. A decrease in r_u was observed at higher strain levels, which mostly occurred during the higher shaking amplitude tests. At the same strain level, the effect of effective vertical stress (σ'_v) on pore pressure

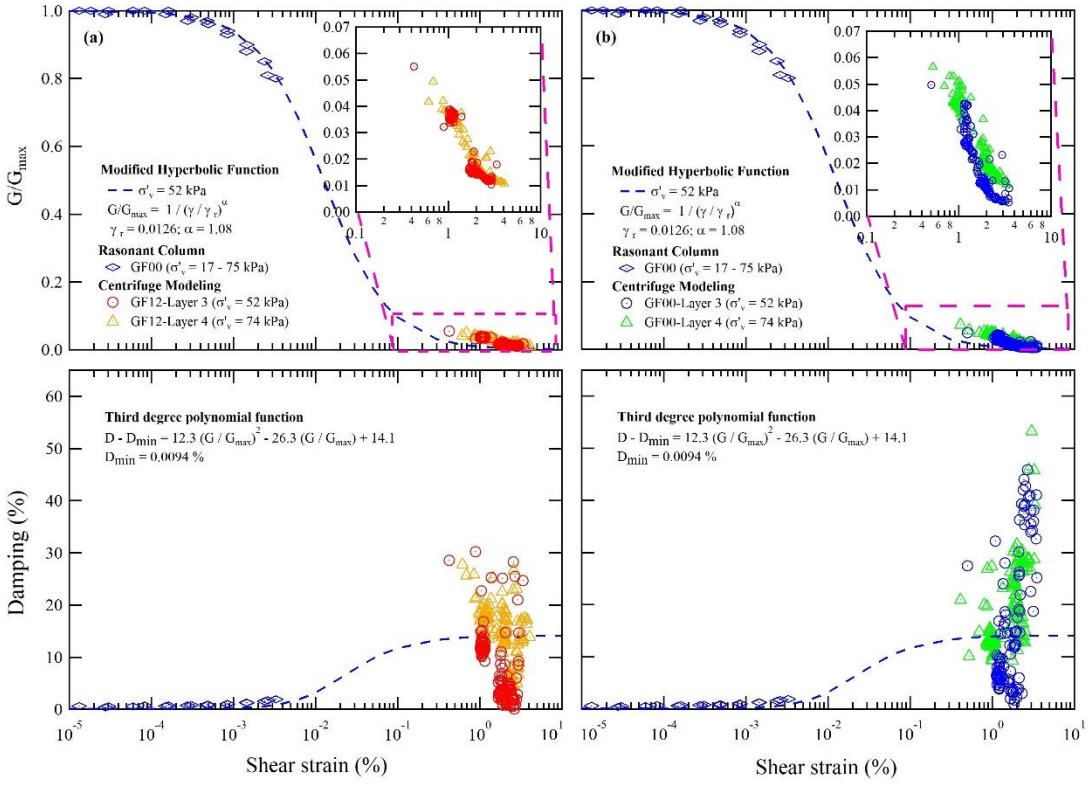

Figure 4.22 Shear modulus reduction and damping curves for Models: (a) GF12, and (b) GF00.

development was found, such that r_u was lower when σ'_v increased. It was noted that pore pressure development at low strains is unknown and requires more data. If a trend similar to the one reported in Dobry et al. (1985) was used to predict the threshold shear strain (γ_{th}), it is possible that the γ_{th} value for both models is in the range of 0.08-0.15%. This range is nearly one order of magnitude higher than sands. For instance, Dobry et al. (1985) observed a γ_{th} value of 0.01-0.02% for sands. Pore pressure development of gravelly soil tested in this study may be delayed due to its higher permeability, larger void space, and very loose condition. Interestingly, the estimated γ_{th} value corresponding to the G/G_{max} of approximately 0.55 (see Figure 4.22) is consistent with the observation by Hsu and Vucetic (2004) for both sand and clay samples. It should be noted that the pore pressure development in the centrifuge model is more complicated than the element tests because the impact of partial drainage may contribute to the observed behaviors at a certain strain level; however, the stress condition in centrifuge model tests is more representative to the field condition.

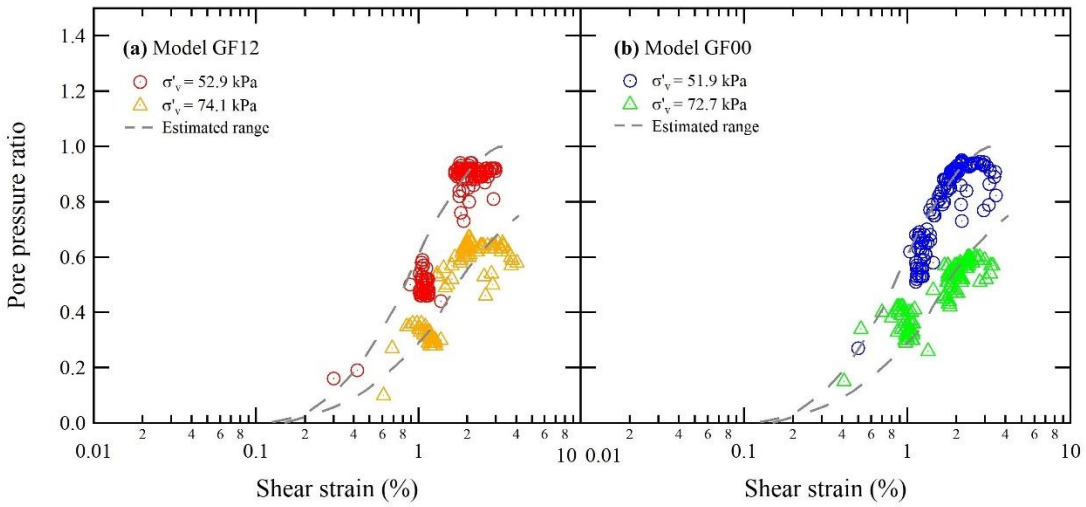

Figure 4.23 Excess pore pressure ratio with shear strain for Models: (a) GF12, and (b) GF00.

4.4.2.7 Cyclic Mobility of Shear Modulus, Damping, and Pore Pressure Ratio

Figure 4.24 presents a plot of modulus reduction, damping, and pore pressure ratio with the number of cycles for the soil model with a mean effective vertical stress of 53 kPa. The shear stress-strain loops at the representative number of cycles are shown in Figure 4.25. The shear modulus significantly decreases at the beginning of the shaking event and reaches a minimum value within less than 10 cycles for both models, regardless of shaking amplitudes. The shear modulus reversely increases after the 20th cycle for Model GF00 due to de-liquefaction behaviors, as discussed by Kutter and Wilson (1999), Wei et al. (2010), Manandhar et al. (2021), and others. Nevertheless, a slight increase in shear modulus for Model GF12 was also observed. At higher shaking amplitudes, the lower shear modulus was comparatively observed. In comparison with the shear modulus behavior, the damping decreased more gradually with an increasing number of cycles. Model GF00 exhibits an increase in damping toward the end of shaking for the amplitudes of 0.19 and 0.27 g. For the 0.40-g shaking amplitude, erratic damping behavior of Model GF00 was observed, starting with brief decreases during the first few cycles, then significantly increasing to reach a peak at the 15th cycle, followed by significant decreases toward the end of shaking. The behavior was inconsistent with the other shaking amplitudes, which is possibly due to the impact of full liquefaction from the soil layers above. However, the impact of full liquefaction was not observed in the shear modulus behavior.

The correlation between shear modulus and damping with the development of r_u was evident in both models, except for the erratic damping behavior for the 0.40-g shaking amplitude mentioned above. An increase in r_u in the first few cycles corresponds with a decrease in shear modulus, which implies that the soil experienced a sudden loss of strength

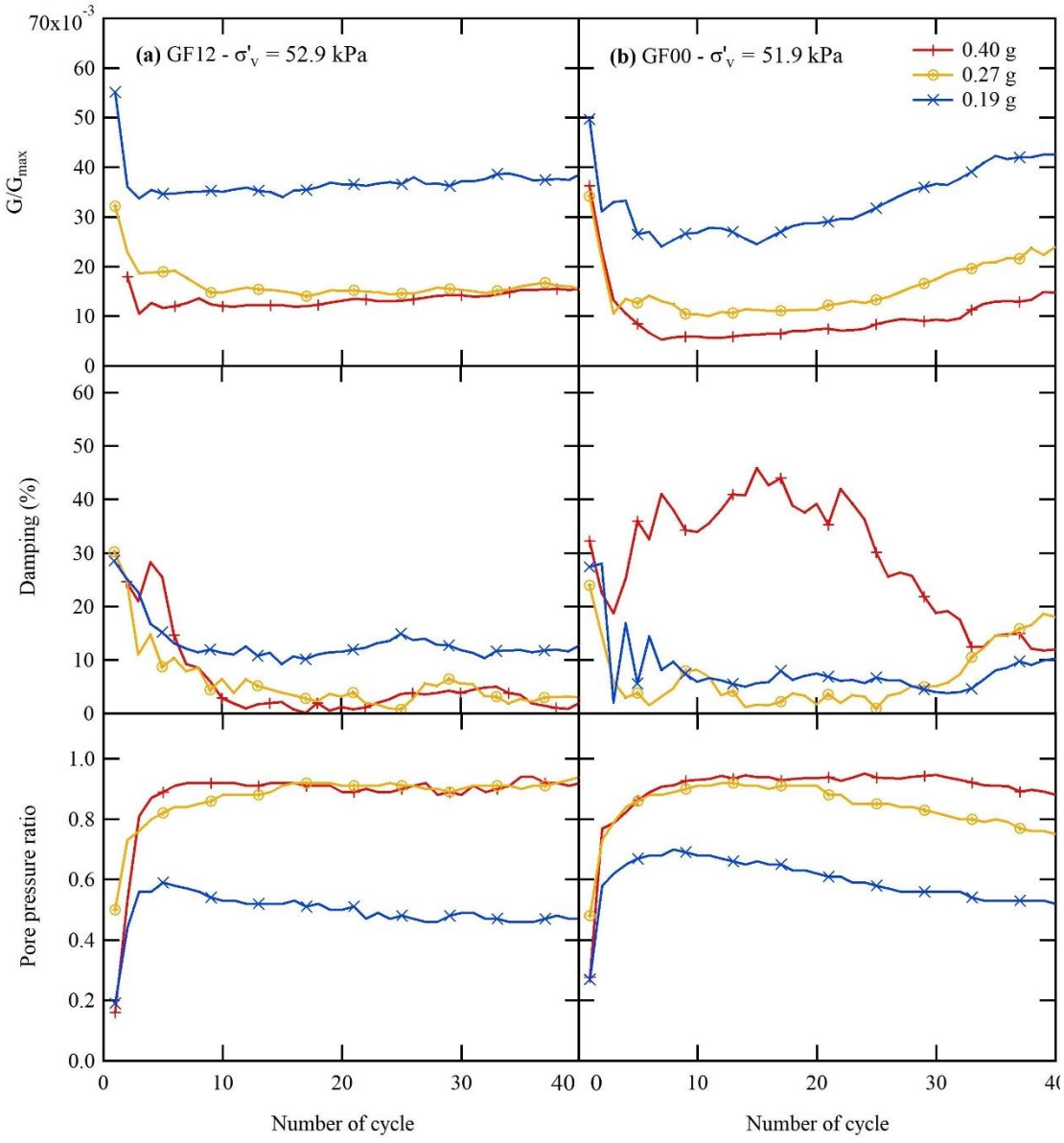

Figure 4.24 Cyclic mobility of shear modulus, damping, and excess pore pressure ratio for Models: (a) GF12, and (b) GF00.

and stiffness due to the rapid development of pore water pressure. At the same time, the gradual decrease in damping may coincide with the regaining of stiffness, which often appears in half of the cycle, as shown in Figure 4.25, while the shaking continues due to the dilative behavior. According to Brennan et al. (2005), a significant reduction in the damping of saturated sands was observed once r_u was higher than 0.6. The dissipation of

pore water pressure resulting in the decreased r_u in Model GF00 after the 10th cycle correlates with the increase in shear modulus as the soil de-liquefied. The regaining of shear modulus during shaking is typically found in the medium-dense to dense sand behavior (e.g., Kutter and Wilson 1999, Manandhar et al. 2021, Gu et al. 2022).

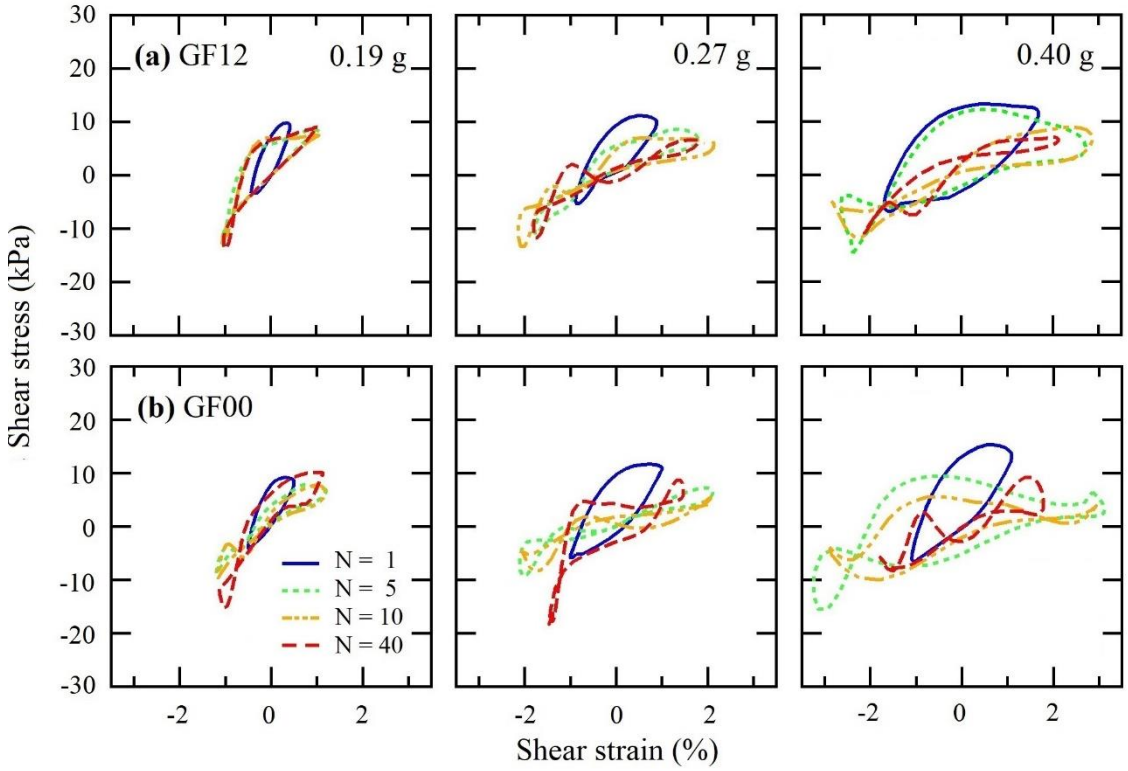

Figure 4.25 Shear stress-strain behavior with number of shaking cycles.

4.4.2.8 Lateral Displacement

For most of the tests, there were a limited number of LVDTs installed along the side of the centrifuge laminar container. Some of them reached their travel limit during testing. Consequently, the determination of lateral displacment relied mainly on the post-test investigation upon the completion of the test. However, it is noted that the available LVDT records were also used to verify the manual measurement when possible. It was found that the permanent lateral displacement mainly occurred due to the shaking, and the

largest magnitude was observed near the top of the model, particularly when the soil liquefied. Figure 4.26 presents the accumulated lateral displacement along the profile of the laminar container for all of the tests. Higher lateral displacement was observed for Model GF00 than for Model GF12, which coincided with the relatively higher shear strains generated in Model GF00, particularly for the shaking ampltidue of 0.19 and 0.27 g, as shown in Table 4.4. The displacement increases as the shaking ampltiude increases from 0.19 to 0.27 g for both models. However, when the shaking amplitude increased from 0.27 to 0.40 g, the lateral displacement did not change for Model GF12, while a decrease in displacement was observed for Model GF00. The decrease in displacement may be related to the densification of the soil during shaking. More details are provided in the following section.

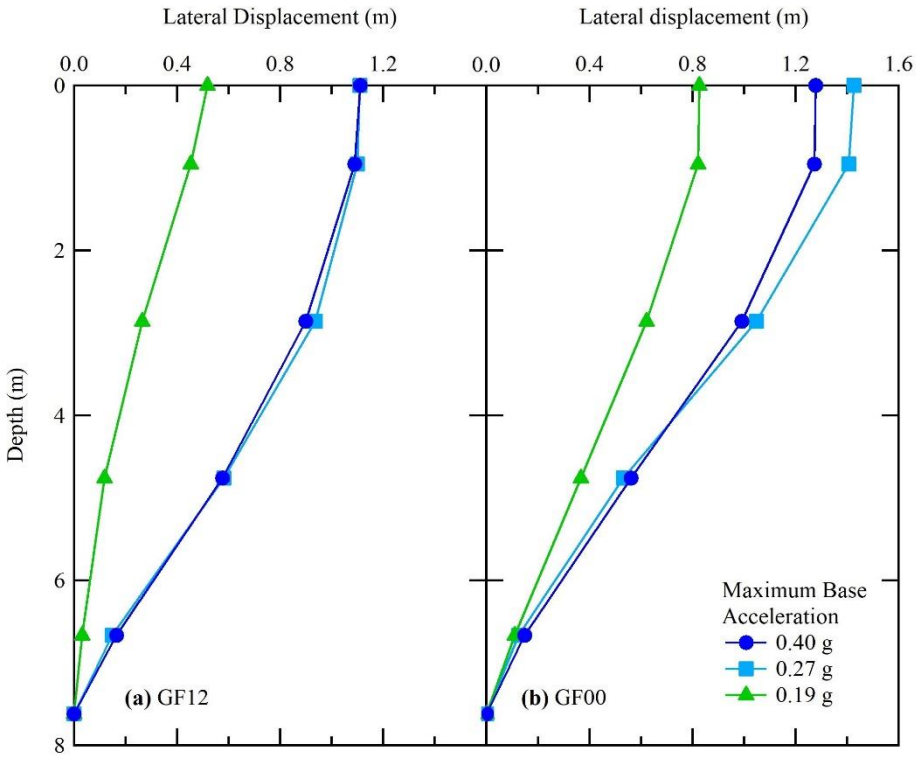

Figure 4.26 Lateral displacement due to shaking (prototype scale) for Models: (a) GF12, and (b) GF00.

4.4.2.9 Settlement and Particle Rearrangements during Shaking and Post-shaking consolidation

Table 4.5 presents a summary of surface settlement measured from consolidation prior to shaking and settlement measured after the completion of the test (i.e., shaking and post-shaking consolidation). Similar to lateral displacement, the settlement of the model was mainly determined during the post-test investigation and cross-checked with the LVDT records during the test. The surface settlement was used to calculate the average relative density (D_r) of the model. As mentioned previously, the D_r of Model GF12 and GF00 were close (D_r ~ 15-16%) prior to shaking. The settlement measurement after the test was approximately 0.3 m (prototype) for Model GF00, regardless of the shaking amplitudes. Therefore, the final D_r was approximately the same at 39-41%. For Model GF12, the settlement varied with the shaking amplitudes. The final D_r was 21, 49, and 31% for shaking amplitudes of 0.19, 0.27, and 0.40 g, respectively. It is interesting to observe that the highest relative density was found at the shaking amplitude of 0.27 g, possibly because the densification of the soil was optimum at this level of shaking, while the 0.40-g shaking was high enough to loosen the soil. This observation also emphasizes the influence of fines content.

The particle rearrangement was investigated by performing post-test grain size distribution analysis for four separate layers of soil in the model. Among all the tests, Model GF12, which was subjected to the high amplitude of 0.40 g, exhibited the most distinctive behavior. The grain size distribution curve of the surface layer consists of approximately 6% more fines content than the initial condition, as shown in Figure 4.27(a). As expected, the fine particles required less effort to move upward against gravity, and

when the shaking amplitude was high enough, more fine particles moved to the surface. These particles likely suspend during liquefaction and redeposit at the surface due to its light weight (as shown in the Figure 4.28); hence, lower settlement was observed for the 0.40-g test than the 0.27-g test. The very bottom layer of this model also consisted of more sand than other layers, which implies that while the fine particles move upward, the sand particles move downward to fill the void space between the gravel particles. For the same model subjected to lower shaking amplitudes, similar behavior was observed, although less fines content accumulated near the surface. The post-test investigation shows a difference in the void ratio between the top and the bottom of the model, in which the top was looser than the bottom.

The typical results for Model GF00 are shown in Figure 4.27(b). Model GF00 was composed of sand and gravel, and the shaking levels generated in this study were not high enough to cause the sand to migrate to the surface. Gravel and sand are both densified during shaking, but due to the interlocking of gravel particles, more sand is able to move downward by gravity after shaking. As shown in Figure 4.27(b), more sand particles accumulated at deeper depths to fill the void space between gravel particles, similar to the behavior of Model GF12. Although the gravel and sand particles were densified due to shaking, the difference between the shaking amplitude of 0.27 and 0.40 g was not large enough to increase soil densification, due to the impact of particle interlocking. For all the tests, the amount of gravel increased (5-10%) near the top half of the model, while the amount of sand increased (5-10%) toward the bottom of the model. The change in the amount of sand and gravel between all four layers was within ±10%, which interestingly may result in different soil classifications. For instance, the top half of the model is

classified as poorly graded gravel (GP), and the bottom half is classified as poorly graded sand (SP). During the post-test investigation for all testing amplitudes, the void ratios varied between soil layers, decreasing to 0.37 at the bottom soil layer and increasing to 0.69 at the top soil layer. Based on surface settlement, the overall volumetric strain for Model GF12 was approximately 1 to 6%, while Model GF00 was approximately 4%. These values were consistent with the volumetric strain of a waste rock material mixed with tailings studied by Antonaki et al. (2018).

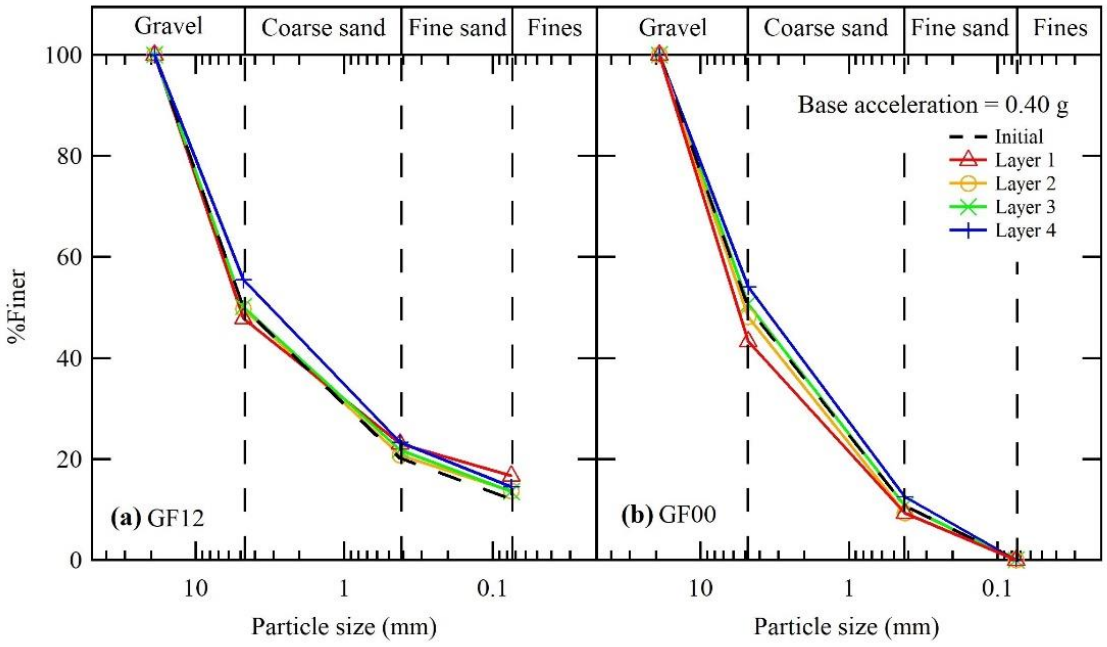

Figure 4.27 Grain size distribution of each layer after shaking and re-consolidation for Models: (a) GF12, and (b) GF00.

Table 4.5 Summary of surface settlement after the end of testing.

Sample ID	Shaking Amplitude (g)	Surface Settlement (m)	Relative Density (%)
GF12	0.40	0.21	31.4
	0.27	0.44	49.1
	0.19	0.08	20.8
GF00	0.40	0.28	39.0
	0.27	0.31	41.1
	0.19	0.28	39.0

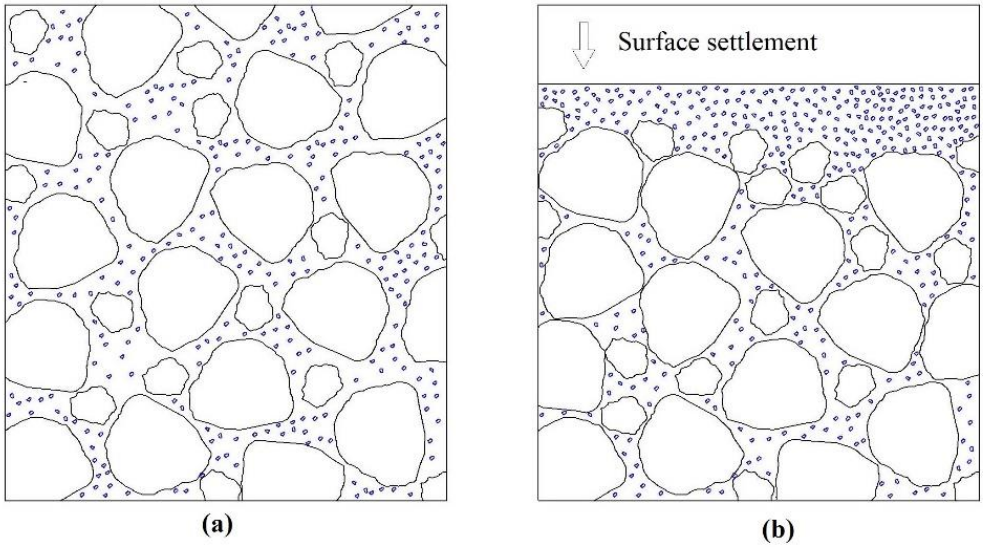

Figure 4.28 Schematic of particle rearrangement (not to scale) (a) before and (b) after shaking event.

4.5 Conclusion

The conclusions regarding the effect of soil composition and the effect of the model's shaking amplitude on soil mixtures are presented in Sections 4.5.1 and 4.5.2, respectively, based on the data presented previously in Section 4.4.

4.5.1 Effect of Soil Composition

The results are based on four soil compositions in the loose condition: G40S48F12, G50S38F12, G50S50F00, and G70S30F00 samples. Each centrifuge model was subjected to a 0.27-g sinusoidal base shaking amplitude. Several key conclusions from the experiments are summarized as follows:

1) The normalized shear wave velocity (V_{s1}) of waste rock material composed of gravel content ranging from 40 to 70% at relative density (D_r) of 13 to 21% is approximately 117 and 128 m/s. No clear trend was observed between D_r and shear wave velocity because the range of D_r was small for these samples, and there was an influence of soil composition.

2) The base shaking acceleration of 0.27 g liquefied waste rock material with a mixture of 40/48/12, 50/38/12, and 50/50/00 percent gravel/sand/fines up to 5.7 m. The mixture of 40/48/12 required the least number of cycles to liquefy. The same shaking level did not liquefy waste rock material with a mixture of 70/30 percent gravel/sand. The cyclic stress ratio (CSR) that was observed in the bottom soil layer with effective stress of 70 kPa for all models was in the range of 0.19 to 0.26 and the corresponding dynamic shear strains were within the range of 1.2 to 2.0% regardless of the level of pore pressure development.

3) Negative spikes that appeared in the acceleration time histories can represent the dilative behavior of the sample. All models experienced significant dilation spikes, particularly when they liquefied or developed high excess pore pressure. Waste rock material with a mixture of 50/50 percent gravel/sand was borderline between

sand and gravel, but this specimen appeared to exhibit behavior similar to other gravelly soils tested in this study based on dilative behaviors that were observed in the acceleration time histories.

4) For the models with no fines content, the pore pressure dissipation during shaking was more significant at the deeper soil depths, resulting in the regaining of stiffness. After the shaking event, pore pressure dissipated rapidly for all models and the rate of dissipation was dependent on soil permeability.

5) Dilative behaviors caused unsymmetrical stress-strain loops. The behavior was more pronounced at shallow depths where the effective stress was relatively low. When the excess pore pressure was high, the shear modulus significantly decreased at larger shear strains, as observed by the banana-shaped stress-strain loop, which was similar to sand behaviors.

6) Less degradation of the stiffness was observed in non-liquefied soil layer, and some reduction of damping was also observed at the beginning of the shaking. However, overall, the damping value appeared to be nearly constant with the number of cycles.

7) The permanent shear strain at the ground surface is less than 10% in the non-liquefaction model and up to 20% in the liquefied model. The larger permanent shear strain was observed in the model with higher sand content.

8) Volumetric strain due to shaking and post-shaking consolidation was observed to be higher in the models with fines content than the models without fines content.

Since the shear wave velocity of these specimens was very close, the difference in volumetric strain is likely influenced by soil composition and void ratio.

Findings from this study show that mine waste rock material decomposition may increase liquefaction potential as sand and fines content increase, while shear wave velocity remains the same.

4.5.2 Effect of the Model's Shaking Amplitude on Soil Mixtures

The results are based on two soils composed of 50% gravel content, and the effects of 12% fines content were evaluated. In addition, the samples were tested in a loose condition with three shaking amplitudes: 0.20, 0.27, 0.40 g. The following are key conclusions:

1) Dilation spikes in the acceleration time histories occurred when r_u approached 0.6, and no impact of fines content on dilatancy was found in both models.

2) Fine particles helped prevent significant loss of shear strength during soil liquefaction, while the model without fine particles regained shear strength during the shaking event because of the dissipation of pore pressure.

3) Both models exhibit a comparable rate of pore pressure development along the model depth, while the model with fine particles required more time to dissipate the excess pore pressure. Upward dissipation of pore water pressure likely reduced the rate of pore pressure development in the bottom soil layer particularly when the models were under moderate to high amplitude shaking.

4) When the shaking amplitude increased, the double amplitude shear strain increased, as anticipated. However, fine particles had no effect on dynamic shear strain.

5) A larger variation of CRR with number of cycles was observed in the model without fines. However, the $CRR_{M=7.5}$ value of 0.22 was observed for both models for the effective vertical stress up to 53 kPa.

6) Normalized shear modulus values of less than 0.1 were observed in all layers of both models for all shaking events. Damping values observed for both models were very scattered, and the model with fines had higher damping than that of the model without fines.

7) As the number of shaking cycles increased, shear stress decreased as a result of increased pore pressure, which led to a decrease in shear modulus and damping at high strains.

8) The densification of the model with fines was optimal at the 0.27-g shaking, whereas the 0.40-g shaking was high enough to loosen the soil. The model with no fines had little to no change in relative density throughout a wide range of shaking amplitudes.

9) During shaking, while the fine particles moved upward, the sand particles moved downward to fill the void space between the gravel particles. This phenomenon was less pronounced at lower shaking amplitudes. The percentage of sand and gravel changed by less than ±10% throughout the entire model.

CHAPTER 5

SUMMARY, CONCLUSIONS, AND FUTURE WORK

5.1 Summary

Understanding the response of gravelly soil under earthquake conditions requires an understanding of the mechanism of soil liquefaction and dynamic soil behaviors. These mechanisms were intensively studied in this research using advanced laboratory testing and physical modeling in the centrifuge. The advanced laboratory testing includes cyclic triaxial (CTX), isotopically consolidated drained (CID) triaxial, and resonant column (RC) tests to evaluate both cyclic and post-cyclic behaviors of the waste rock materials. The waste rock materials were then utilized to create reconstituted gravelly soil models for centrifuge modeling test.

The first part of this research focused on the evaluation of the cyclic responses of mine waste materials, which contained gravel, sand, and fine particles. Undisturbed samples were collected using a six-inch diameter Shelby tube to provide a 6:1 dimension ratio (specimen size to maximum particle size). The experiments were conducted on 100-mm diameter specimens using CTX, CID triaxial, and RC tests. The cyclic responses at high-strain levels and their liquefaction susceptibility were obtained. The shear modulus reduction and damping curves at high-strain levels were also developed and analyzed with the excess pore pressure ratio to characterize the impact of pore pressure development. In

addition, strength parameters prior to cyclic through post-cyclic loading tests were evaluated and compared to those of typical sands and pure gravels from the literature. Furthermore, the matrix soil structures of composite soils, containing gravel, sand, and fines, were analyzed based on the concept of phase relationship.

The second part of this research focused on an evaluation of liquefaction behavior on loose gravelly soil mixtures using centrifuge modeling testing. These specimens were called G40S48F12, G50S38F12, G50S50F00, and G70S30F00. Letter G, S, and F represent gravel, sand, and fines, respectively, and the numbers represent the corresponding % by weight. Each soil specimen was prepared in a centrifuge laminar container to test under 50-g gravitational acceleration in the centrifuge. At 50 g, a level ground soil profile of 7.6 m was replicated. Upon full consolidation, shaking was performed using the designed 1-directional shaking motion of a 1-Hz harmonic sinusoidal motion for 40 cycles. Shaking tests with amplitude 0.40, 0.27, and 0.19 g (in prototype scale) were performed on G50S38F12 and G50S50F00 but only a 0.27-g shaking test was performed on G40S48F12 and G70S30F00. The effect of soil compositions was evaluated at 0.27-g shaking amplitude on all soil samples, and the effect of shaking amplitude was evaluated on G50S38F12 and G50S50F00. During shaking, the data obtained from the centrifuge modeling, including acceleration and pore pressure, were utilized to calculate shear stress, shear strain, and pore pressure ratio to analyze soil behaviors along the depth of the soil profile under shaking conditions. In addition, the cyclic stress ratio (CSR) was calculated and plotted with number of cycles to cause liquefaction (N_L) to evaluate liquefaction resistance of each soil model. Furthermore, the post-test investigation was performed

immediately after the test to investigate the permanence shear strain, volumetric strain, and particle rearrangement due to the shaking.

5.2 Conclusions

This research study was divided into two topics. The first topic was on the cyclic response of undisturbed and reconstituted gravelly soil under triaxial testing condition and the second topic was on the centrifuge modeling of liquefaction behavior of gravelly soils. The overall conclusions for each topic are listed below:

5.2.1 TOPIC 1: Cyclic response of undisturbed and reconstituted gravelly soil under triaxial testing condition

- The V_s-based liquefaction susceptibility chart developed for clean sands does not apply to the gravelly soils tested in this study, as the gravelly soils are liquefiable at $V_{s,1}$ within 260-400 m/s.

- The cyclic resistance ratio (CRR) of gravelly soils in this study is comparable to that of pure sands; however, the gravelly soils have a significantly higher CRR than pure gravels.

- The ultimate friction angle of the reconstituted gravelly soils (ϕ'_{ult}) is 51.5 degrees, while the phase transform friction angle (ϕ'_{pt}) is around 41.6 degrees under cyclic loading. The effective friction angle (ϕ') in the post-cyclic loading was found to be approximately 32.5 degrees at the axial strains between 5 and 20% which is a significant reduction compared to the ϕ'_{pt} and ϕ'_{ult}.

- The composite soils, containing gravel, sand, and fines, having the matrix structure described as Gravel-Fines Matrix, which represents a mixture having gravel floating in between fine particles, are non-liquefiable. The soils having matrix structures described as Gravel-Sand Matrix, which represents a mixture having gravel floating in between sand particles, are liquefiable. The structure described as Interlocked Gravel Matrix, which represents a mixture having gravel in contact with each other, may also be susceptible to liquefaction, but the loading amplitude and the relative density of the sample should also be considered.

5.2.2 TOPIC 2: Centrifuge modeling of liquefaction behavior of gravelly soils

- The normalized shear wave velocity ($V_{s,1}$) of waste rock materials comprised of 40 to 70 percent gravel at relative density (D_r) of 13-21% ranges between 117 and 128 m/s. There was no obvious correlation between D_r and $V_{s,1}$.

- The base shaking acceleration of 0.27 g liquefied all models of waste rock materials in this study up to 5.7 m, with the exception of the model with a mixture of 70/30 percent gravel/sand. The mixture of 40/48/12 percent gravel/sand/fines required the least number of cycles to liquefy.

- The model without fines exhibited a greater variation in the range of CRR with number of cycles. For an effective vertical stress up to 53 kPa, the $CRR_{M=7.5}$ value of 0.22 was observed for both models with 50/38/12 and 50/50/00 percent gravel/sand/fines.

- The dilative behavior of the sample can be represented by negative spikes that appeared in the acceleration time histories. All models experienced significant

dilation spikes, particularly when they liquefied or developed high excess pore pressure.

- The rate of pore pressure development along the model depth is comparable for models with and without fine particles, but the model with fine particles required more time to dissipate the excess pore pressure, and the fines aided in preventing a significant loss of shear strength during soil liquefaction. For models containing no fines, the pore pressure dissipation during shaking was faster at deeper soil depths, resulting in the regaining of shear strength. There was no noticeable impact of overburden stress on the rate of pore pressure dissipation.

- Dilation spikes were observed in the acceleration time histories when r_u approached 0.6, but there was no effect on fines content on dilatancy in these models. The behavior was more pronounced at shallow depths where the effective stress was relatively low.

- For cyclic mobility, shear stress decreased as the number of shaking cycles increased, due to an increase in pore pressure, which resulted in a reduction in shear modulus and damping at high strains. In all layer, normalized shear modulus values of less than 0.1 were observed, while a reduction in damping was also observed at the beginning of the shaking. The overall damping values appeared to be rather scattered, with the model containing fines exhibiting greater damping than the model without fines.

- The permanent shear strain at the ground surface is less than 10% in the non-liquefaction model and up to 20% in the liquefied model. The model without fines

exhibited a greater permanent shear strain than the model with fines, and the model with a higher sand content exhibited higher permanent shear strain.

- The models with fines material exhibited greater volumetric strain, due to shaking and post-shaking consolidation, than the models without fines. The optimal densification of the model with fines occurred at 0.27 g, whereas 0.40 g was high enough to loosen the soil.

- During shaking, while fine particles moved upward, sand particles moved downward to fill the void space between the gravel particles. This phenomenon was less pronounced at lower shaking amplitudes.

5.3 Recommendations for Future Work

The following recommendations were made to further investigate the dynamic and liquefaction behavior of gravelly soil mixtures.

1. The behavior of waste rock materials with percentage of gravel-sand-fines that classify as at borderline between sand and gravel should be investigated because those materials appeared to exhibit behavior similar to other gravelly soils.

2. More gravelly soil mixtures with structures described as gravel floating in fines and gravel interlocking structures should be further evaluated with cyclic triaxial testing.

3. The field shear wave velocity (V_s) of the gravelly soils should be determined and compared to the laboratory V_s to develop liquefaction susceptibility charts for gravelly soil mixtures.

4. A set of cyclic loading tests should be conducted on gravelly soil mixtures under drained conditions to evaluate the volume change.

5. The small-strain dynamic behaviors of gravelly soil mixtures should be examined to establish a database for site response analysis.

6. For centrifuge modeling, the dynamic response and liquefaction behavior of the gravelly soil mixtures should be evaluated at lower shaking amplitudes.

7. To assess liquefaction susceptibility of gravelly soil mixtures, the effects of relative density (D_r) and other index properties on liquefaction behaviors should be investigated.

REFERENCES

Abbaszadeh, S., Nguyen, T. D., & Wu, Y. (2018). "Optimal trading under non-negativity constraints using approximate dynamic programming." *Journal of the Operational Research Society*, *69*(9), 1406-1422.

Abdoun, T., Gonzalez, M. A., Thevanayagam, S., Dobry, R., Elgamal, A., Zeghal, M., ... & El Shamy, U. (2013). "Centrifuge and large-scale modeling of seismic pore pressures in sands: Cyclic strain interpretation." *Journal of geotechnical and geoenvironmental engineering*, *139*(8), 1215-1234.

Abdoun, T., NI, M., Dobry, R., Zehtab, K., Marr, A., & El-Sekelly, W. (2020). "Pore pressure and K_σ evaluation at high overburden pressure under field drainage conditions. II: additional interpretation." *J. Geotech. Geoenviron. Eng.* 146(9), 04020089.

Adamidis, O., & Madabhushi, G. S. P. (2015). "Use of viscous pore fluids in dynamic centrifuge modelling." *International Journal of Physical Modelling in Geotechnics*, 15(3), 141–149.

Afacan, K. B., Brandenberg, S. J., & Stewart, J. P. (2014). "Centrifuge modeling studies of site response in soft clay over wide strain range." *Journal of Geotechnical and Geoenvironmental Engineering*, *140*(2), 04013003.

Alhani, I. J., Noor, M. J. M., & Albadri, W. M. (2018). "Membrane penetration effects on shear strength and volume change of soil during triaxial test." In *AIP Conference Proceedings* (Vol. 2020, No. 1, p. 020008). AIP Publishing LLC.

Andrianopoulos, K. I., Papadimitriou, A. G., & Bouckovalas, G. D. (2010). "Bounding surface plasticity model for the seismic liquefaction analysis of geostructures." *Soil Dynamics and Earthquake Engineering*, *30*(10), 895-911.

Andrus, R. D. (1994). "In situ characterization of gravelly soils that liquefied in the 1983 Borah Peak earthquake." *Doctoral dissertation, The University of Texas at Austin.*

Andrus, R. D., & Stokoe, K. H. (2000). "Liquefaction resistance of soils from shear-wave velocity." *Journal of geotechnical and geoenvironmental engineering*, *126*(11), 1015-1026.

Andrus, R. D., & Stokoe, K. H. (1997). "Liquefaction resistance based on shear wave velocity." In Proc., NCEER Workshop on Evaluation of Liquefaction Resistance

of Soils, National Center for Earthquake Engineering Research, 89–128. Buffalo, NY: State Univ. of New York

Antonaki, N., Abdoun, T., & Sasanakul, I. (2017). "Consolidation and dynamic response of a layered mine tailings deposit in centrifuge tests." *Geotechnical Testing Journal*, *40*(5), 746-761.

Antonaki, N., Abdoun, T., & Sasanakul, I. (2018). "Centrifuge Tests on Comixing of Mine Tailings and Waste Rock." *Journal of Geotechnical and Geoenvironmental Engineering*, 144(1), 04017099.

Athanasopoulos-Zekkos, A., Lynch, J., Zekkos, D., Gkrizi, A., Admassu, K., Benhamida, B., Spino Rich & Mikolajczyk, M. (2020). "Asset Management for Retaining Walls." *Michigan Department of Transportation*

Balakrishnan, A., & Kutter, B. L. (1999). "Settlement, sliding, and liquefaction remediation of layered soil." *J. Geotech. Geoenviron. Eng.* 125(11), 968-978.

Baldi, G., & Nova, R. (1984). "Membrane penetration effects in triaxial testing." *Journal of Geotechnical engineering*, *110*(3), 403-420.

Barden, L. (1963). "Stresses and displacements in a cross-anisotropic soil." *Geotechnique*, *13*(3), 198-210.

Basham, M. R., & Athanasopoulos-Zekkos, A. (2020). "Effect of Static Shear Stress on Cyclic Resistance of a Uniform Gravel." In *Geo-Congress 2020: Geotechnical Earthquake Engineering and Special Topics* (pp. 105-113). Reston, VA: American Society of Civil Engineers.

Baziar, M. H., & Dobry, R. (1995). "Residual strength and large-deformation potential of loose silty sands." *Journal of geotechnical engineering*, 121(12), 896-906.

Blight, G. E. (2009). "Geotechnical Engineering for Mine Waste Storage Facilities." *CRC Press*.

Bolton Seed, H., Tokimatsu, K., Harder, L. F., & Chung, R. M. (1985). "Influence of SPT procedures in soil liquefaction resistance evaluations." *Journal of geotechnical engineering*, *111*(12), 1425-1445.

Bolton Seed, H., Tokimatsu, K., Harder, L. F., & Chung, R. M. (1985). "Influence of SPT procedures in soil liquefaction resistance evaluations." *Journal of geotechnical engineering*, *111*(12), 1425-1445.Seed H.B., Arango I., Chan C.K. (1975). "Evaluation of soil liquefaction potential for level ground during earthquakes." *A summary report. United States.*

Boulanger R. W., & Idriss I. M. (2004). "Evaluating the potential for liquefaction or cyclic failure of silts and clays." *Davis, California: Center for Geotechnical Modeling.*

Boulanger, R. W., & Idriss, I. M. (2015). "Magnitude scaling factors in liquefaction triggering procedures." *Soil Dynamics and Earthquake Engineering*, *79*, 296-303.

Brennan, A. J., Thusyanthan, N. I., & Madabhushi, S. P. (2005). "Evaluation of Shear Modulus and Damping in Dynamic Centrifuge Tests." *Journal of Geotechnical and Geoenvironmental Engineering*, 131(12), 1488–1497.

BrunoBussièreB. Bussière. (2004) "Hydrogeotechnical properties of hard rock tailings from metal mines and emerging geoenvironmental disposal approaches." *Canadian Geotechnical Journal*. 44(9): 1019-1052.

Cao, Z., T. L. Youd, & X. Yuan. (2011) "Gravelly soils that liquefied during 2008 Wenchuan, China earthquake, Ms= 8.0." *Soil Dyn. Earthquake Eng.* 31(8), 1132-1143.

Carey T., Gavras A., Kutter B., Haigh S.K., Madabhushi S.P.G., Okamura M., Kim D.S., Ueda K., Hung W.Y., Zhou Y.G., Liu K., Chen Y.M., Zeghal M., Abdoun T., Escoffier S., & Manzari M. (2018). "A new shared miniature cone penetrometer for centrifuge testing." In *Physical Modelling in Geotechnics,* 293-298.

Carey, T. J., Stone, N., Bonab, M. H., & Kutter, B. L. (2020). "LEAP-UCD-2017 centrifuge test at University of California, Davis." In *Model Tests and Numerical Simulations of Liquefaction and Lateral Spreading* (pp. 255-276). Springer, Cham.

Cargill, K. W., & Ko, H. Y. (1983). "Centrifugal modeling of transient water flow." *Journal of Geotechnical Engineering*, *109*(4), 536-555.

Castro, G. (1975). "Liquefaction and cyclic mobility of saturated sands." *Journal of the geotechnical engineering division*, *101*(6), 551-569.

Chang, W. J., & Hong, M. L. (2008). "Effects of clay content on liquefaction characteristics of gap-graded clayey sands." *Soils and foundations*, *48*(1), 101-114.

Chang, W. J., & Phantachang, T. (2016). "Effects of gravel content on shear resistance of gravelly soils." *Engineering Geology*, *207*, 78-90.

Charles, J. A., & Watts, K. S. (1980). "The influence of confining pressure on the shear strength of compacted rockfill." *Geotechnique*, *30*(4), 353-367.

Chian, S. C., & Madabhushi, S. P. G. (2010). "Influence of fluid viscosity on the response of buried structures in earthquakes." In *7th international conference of physical modelling in geotechnics* (pp. 111-115).

Chou, J. C., Kutter, B. L., Travasarou, T., & Chacko, J. M. (2011). "Centrifuge modeling of seismically induced uplift for the BART transbay tube." *Journal of Geotechnical and Geoenvironmental Engineering*, *137*(8), 754-765.

Corriveau, J., Barrot, D., Mandayam, S., & Sukumaran, B. (2005). "3-D Shape descriptors for geomaterial aggregates using multiple projective representations." In *Site Characterization and Modeling* (pp. 1-9).

Coulter, H. W., & Migliaccio, R. R. (1966). "Effects of the earthquake of March 27, 1964, at Valdez, Alaska." *U.S.Geological Survey, Professional Paper 542-C*, 1966,36

Cubrinovski, M. (2013). “Liquefaction-Induced Damage in The 2010-2011 Christchurch (New Zealand) Earthquakes.” *International Conf. on Case Histories in Geotechnical Eng.* 1.

Cubrinovski, M., & Ishihara, K. (2000). “Flow potential of sandy soils with different grain compositions.” *Soils and Foundations*, 40(4), 103-119.

De Alba, P. A., Chan, C. K., & Seed, H. B. (1976). “Sand liquefaction in large-scale simple shear tests.” *Journal of the Geotechnical Engineering Division*, *102*(9), 909-927.

Dewoolkar, M. M., Ko, H. Y., Stadler, A. T., & Astaneh, S. M. F. (1999). “A Substitute Pore Fluid for Seismic Centrifuge Modeling.” *Geotechnical Testing Journal*, 22(3), 196–210.

Do, T. N., Ou, C. Y., & Chen, R. P. (2016). “A study of failure mechanisms of deep excavations in soft clay using the finite element method.” *Computers and Geotechnics, 73*, 153-163.

Dobry, R., Abdoun, T., Stokoe II, K. H., Moss, R. E. S., Hatton, M., & El Ganainy, H. (2015). “Liquefaction potential of recent fills versus natural sands located in high-seismicity regions using shear-wave velocity.” *Journal of Geotechnical and Geoenvironmental Engineering*, *141*(3), 04014112-1.

Dow (2002) “Methocel Cellulose Ethers: Technical Handbook.” *The Dow Chemical Company, Staines, UK*

Elgamal A, Yang Z, Lai T, Kutter BL, & Wilson DW. (2005) “Dynamic response of saturated dense sand in laminated centrifuge container.” *J Geotech Geoenviron Eng.,* 131(5): 598-609

Elgamal, A., Zeghal, M., Taboada, V., & Dobry, R. (1996). “Analysis of site liquefaction and lateral spreading using centrifuge testing records.” *Soils and Foundations, 36*(2), 111-121.

Ellis, E. A., Soga, K., Bransby, M. F., & Sato, M. (1998). ‘‘Effect of pore fluid viscosity on the cyclic behavior of sands.’’ *Proc., Int. Conf. Centrifuge 98*, 217–222.

Evans, M. D., & Harder, L. F. (1993). "Liquefaction Potential of Gravelly Soils in Dams." *In Geotechnical Practice in Dam Rehabilitation, ASCE,* 467-481.

Evans, M. D., & S. Zhou. (1995). “Liquefaction behavior of sand-gravel composites.” *J. Geotech. Eng.* 121(3), 287–298.

Evans, M. D., & Seed, H. B. (1987). “Undrained cyclic triaxial testing of gravels: the effect of membrane compliance.” *College of Engineering, University of California*.

Evans, M. D., Bolton Seed, H., & Seed, R. B. (1992). “Membrane compliance and liquefaction of sluiced gravel specimens.” *Journal of Geotechnical Engineering, 118*(6), 856-872.

Finn, W. L., Pickering, D. J., & Bransby, P. L. (1971). "Sand liquefaction in triaxial and simple shear tests." *Journal of the soil mechanics and foundations division*, *97*(4), 639-659.

Gajić, G., Djurdjević, L., Kostić, O., Jarić, S., Mitrović, M., & Pavlović, P. (2018). "Ecological potential of plants for phytoremediation and ecorestoration of fly ash deposits and mine wastes." *Frontiers in Environmental Science*, *6*, 124.

Garnier, J., Gaudin, C., Springman, S. M., Culligan, P. J., Goodings, D., Konig, D., ... & Thorel, L. (2007). "Catalogue of scaling laws and similitude questions in geotechnical centrifuge modelling." *International Journal of Physical Modelling in Geotechnics*, 7(3), 01-23.

Geremew, A. M., & Yanful, E. K. (2013). "Dynamic properties and influence of clay mineralogy types on the cyclic strength of mine tailings." *International Journal of Geomechanics*, *13*(4), 441-453.

Gerrard, C. M., Davis, E. H., & Wardle, L. J. (1972). "Estimation of the settlements of cross-anisotropic deposits using isotropic theory" *Geomech J*. 62:1–10

Ghalesari, A. T., & Rasouli, H. (2014). "Effect of gravel layer on the behavior of piled raft foundations." In *Advances in Soil Dynamics and Foundation Engineering* (pp. 373-382).

Gu, X., D. Wu, K. Zuo, & A. Tessari. (2022). "Centrifuge Shake Table Tests on the Liquefaction Resistance of Sand with Clayey Fines." *J. Geotech. Geoenviron. Eng.* 148(2), 04021180.

Guoxing, C., W. Qi, S. Tian, Z. Kai, Z. Enquan, X. Lingyu, & Z. Yanguo. (2021). "Cyclic behaviors of saturated sand-gravel mixtures under undrained cyclic triaxial loading." *J. Earthquake Eng.* 25(4), 756-789.

Haeri, H., Sarfarazi, V., Shemirani, A. B., & Zhu, Z. (2018). "Direct shear testing of brittle material samples with non-persistent cracks." *Geomechanics and Engineering*, *15*(4), 927-935.

Haeri, S. M., & Shakeri, M. R. (2010). "Effect of membrane compliance on cyclic resistance of gravelly sand." *Geotech. Test. J*, *33*(5), 1-10.

Haeri, S. M., & Shakeri, M. R. (2010). "Effects of membrane compliance on pore water pressure generation in gravelly sands under cyclic loading." *Geotechnical Testing Journal*, *33*(5), 375-384.

Harder Jr, L. F., & Boulanger, R. (1997). "Application of K and K correction factors." In *Proceeding of the NCEER workshop on evaluation of liquefaction resistance of soils* (pp. 167-90).

Harder Jr, L. F., & J. P. Stewart. (1996) "Failure of Tapo Canyon tailings dam." *Journal of Performance of Constructed Facilities* 10(3), 109-114.

Hatje, V., Pedreira, R. M., de Rezende, C. E., Schettini, C. A. F., de Souza, G. C., Marin, D. C., & Hackspacher, P. C. (2017). "The environmental impacts of one of the largest tailing dam failures worldwide." *Scientific reports*, *7*(1), 1-13.

Holtz W. G. (1961). "Discussion of General Report on Earth Dams, Slopes and Excavations." *In Fifth International Conference of Soil Mechanics and Foundation Engineering, Paris, Vol. 3,* 343.

Holtz, W. G., & Gibbs, H. J. (1956). "Triaxial shear tests on pervious gravelly soils." *Journal of the Soil Mechanics and Foundations Division*, *82*(1), 867-1.

Holtz, W. G., & W. Ellis. (1961). "Triaxial shear characteristics of clayey gravel soils." *Proc. 5th Int. Conf. Soil Mech. Found. Eng., Paris* 1, 143-149.

Hryciw, R. D., S. E. Shewbridge, K. M. Rollins, M. McHood, & M. Homolka. (1991). "Soil Amplification at Treasure Island During the Loma Prieta Earthquake." *International Conferences on Recent Advances in Geotechnical Earthquake Engineering and Soil Dynamics* 15.

Hsu, C. C., & M. Vucetic. (2004). "Volumetric threshold shear strain for cyclic settlement." *J. Geotech. Geoenviron. Eng.* 130(1), 58-70.

Hubler J.F. (2017). "Laboratory and in-situ assessment of liquefaction of gravelly soils." *Ph.D.dissertation, AnnArbor: University of Michigan.*

Hubler, J. F., Athanasopoulos-Zekkos, A., & Zekkos, D. (2018). "Monotonic and cyclic simple shear response of gravel-sand mixtures." *Soil Dynamics and Earthquake Engineering*, *115*, 291-304.

Hubler, J. F., Athanasopoulos-Zekkos, A., and Zekkos, D. (2017). "Pore Pressure Generation of Pea Gravel , Sand , and Gravel-Sand Mixtures in Constant Volume Simple Shear." *The 3rd International Conference on Performance Based Design in Earthquake Engineering (PBD-III), Vancouver, Canada*.

Hubler, J., Athanasopoulos-Zekkos, A., Ohm, H.-S., and Hryciw, R. (2014). "Effect of Particle Morphology on the Monotonic Response of Gravel-Sized Soils through Large-Scale Simple Shear Testing.", *Geo-Congress 2014: Geo-characterization and Modeling for Sustainability*, 683–692.

Hughes, F. E., & Madabhushi, S. P. G. (2018). "The importance of vertical accelerations In liquefied soils." In *Physical Modelling in Geotechnics*, 967-973.

Hwang, S. K. (1997). "Investigation of the Dynamic Properties of Natural Soils." *Ph. D. Dissertation, The University of Texas at Austin*

Idriss, I. M., & Boulanger, R. W. (2006) "Semi-empirical procedures for evaluating liquefaction potential during earthquakes." *Soil dynamics and earthquake engineering*, *26*(2-4), 115-130.

Ishihara, K. (1985). “Stability of natural deposits during earthquakes,” *Proceedings of the 11th international conference on soil mechanics and foundation engineering, San Francisco, CA* 321–376.

Ishihara, K. (1993). “Liquefaction and Flow Failure During Earthquakes.” *Geotechnique*, 43(3), 351–451.

James, M., Aubertin, M., Wijewickreme, D., & Wilson, G. W. (2011). “A laboratory investigation of the dynamic properties of tailings.” *Canadian Geotechnical Journal*, *48*(11), 1587-1600.

Joseph, P. G., Einstein, H. H., & Whitman, R. V. (1988). “A literature review of geotechnical centrifuge modeling with particular emphasis on rock mechanics.”

Kagawa, T., Sato, M., Minowa, C., Abe, A., & Tazoh, T. (2004). “Centrifuge simulations of large-scale shaking table tests: case studies.” *Journal of Geotechnical and Geoenvironmental Engineering*, *130*(7), 663-672.

Kimura, T. (1993). “Lecture Presented at US Japanworkshop on Liquefaction.” *Napa, CA.*

Ko H.Y. (1988). “Summary of the state-of-the-art in centrifuge model testing.” *Centrifuge in Soil Mechanics,* 11–28.

Ko, H. Y. (1994) “Modeling Seismic Problems in Centrifuges.” *Centrifuge 94, Leung, Lee and Tan (eds.), Balkema, Rotterdam,* pp. 3-12.

Kokusho, T., Hara, T., & Hiraoka, R. (2004). “Undrained shear strength of granular soils with different particle gradations.” *Journal of Geotechnical and Geoenvironmental Engineering*, *130*(6), 621-629.

Kokusho, T., Tanaka, Y., Kawai, T., Kudo, K., Suzuki, K., Tohda, S., & Abe, S. (1995). “Case study of rock debris avalanche gravel liquefied during 1993 Hokkaido-Nansei-Oki earthquake.” *Soils and Foundations*, *35*(3), 83-95.

Kramer, S. L. (1996). “Geotechnical earthquake engineering.” *Prentice Hall, Englewood Cliffs, N. J.*, 653.

Kramer, S. L., Sideras, S. S., & Greenfield, M. W. (2016). “The timing of liquefaction and its utility in liquefaction hazard evaluation.” *Soil Dynamics and Earthquake Engineering*, *91*, 133-146.

Kristina Thygesen (2017) “A mining operation, illustrating a typical process in an open pit mine, from excavation to waste disposal.” *Mine Tailings Storage: Safety Is No Accident.*

Kumar, S. S., Murali Krishna, A., & Dey, A. (2020). “Assessment of dynamic response of cohesionless soil using strain-controlled and stress-controlled cyclic triaxial tests.” *Geotechnical and Geological Engineering*, *38*(2), 1431-1450.

Kutter B. L., Carey T. J., Stone N., Zheng B. L., Gavras A., Manzari M. T., ... & Liu K. (2020). "LEAP-UCD-2017 comparison of centrifuge test results." *In Model Tests and Numerical Simulations of Liquefaction and Lateral Spreading, Springer, Cham*, 69-103.

Kutter, B. L. (1991). "Performance and instrumentation of the large centrifuge at Davis." In *Centrifuge* (Vol. 91, pp. 19-26).

Kutter, B. L. (1992). "Dynamic centrifuge modeling of geotechnical structures." *Transportation research record*, (1336).

Kutter, B. L. (1995). "Recent advances in centrifuge modeling of seismic shaking." *Proceedings 3rd Int. Conf. on Recent Advances in Geotechnical Earthquake Engineering and Soil Dynamics, Vol. II, Missouri Univ. of Science and Technology, Rolla, MO*, 927–941.

Kutter, B. L., & D. W. Wilson. (1999). "De-liquefaction shock waves." In *Proc., 7th US–Japan Workshop on Earthquake Resistant Design of Lifeline Facilities and Countermeasures Against Soil Liquefaction.* Tech. Rep. MCEER-99-0019, edited by T. D. O'Rourke, J. P. Bardet, and M. Hamada, 295–310. Buffalo, NY: State Univ. of New York.

Kutter, B. L., Carey, T. J., Hashimoto, T., Zeghal, M., Abdoun, T., Kokkali, P., ... & Manzari, M. T. (2018). "LEAP-GWU-2015 experiment specifications, results, and comparisons." *Soil Dynamics and Earthquake Engineering*, *113*, 616-628.

Kutter, B. L., Carey, T. J., Stone, N., Bonab, M. H., Manzari, M. T., Zeghal, M., ... & Zhou, Y. G. (2020). "LEAP-UCD-2017 V. 1.01 Model Specifications." In *Model Tests and Numerical Simulations of Liquefaction and Lateral Spreading* (pp. 3-29*). Springer, Cham.*

Kutter, B.L., T. J. Carey, N. Stone, B. L. Zheng, A. Gavras, M. T. Manzari, and K. Liu. (2020). "LEAP-UCD-2017 comparison of centrifuge test results." In: *Model tests and numerical simulations of liquefaction and lateral spreading*. *Springer, Cham*., 69–103.

Kutter, B. L., T. J. Carey, T. Hashimoto, M. Zeghal, T. Abdoun, P. Kokkali, ... & M. T. Manzari. (2018). "LEAP-GWU-2015 experiment specifications, results, and comparisons." *Soil Dyn. Earthquake Eng.* 113, 616-628.

Lade, P. V., & Hernandez, S. B. (1977). "Membrane penetration effects in undrained tests." *Journal of the geotechnical engineering division*, *103*(2), 109-125.

Lee, C., Truong, Q. H., Lee, W., & Lee, J. S. (2010). "Characteristics of rubber-sand particle mixtures according to size ratio." *Journal of materials in civil engineering*, *22*(4), 323-331.

Lewis, M. R., Arango, I., & Stokoe II, K. H. (2013). "Liquefaction resistance of gravelly soils." *In: Proceedings 7th international conference on case histories in geotechnical engineering, Chicago*

Li, S. J., Feng, X. T., Wang, C. Y., & Hudson, J. A. (2013). "ISRM suggested method for rock fractures observations using a borehole digital optical televiewer." *Rock mechanics and rock engineering*, *46*(3), 635-644.

Lin, L. C., & Benson, C. H. (2000). "Effect of wet-dry cycling on swelling and hydraulic conductivity of GCLs." *Journal of Geotechnical and Geoenvironmental Engineering*, *126*(1), 40-49.

Love, A.E.H. (1892). "Mathematical Theory of Elasticity." *Cambridge University*, 643.

Lyu, Z., Chai, J., Xu, Z., Qin, Y., & Cao, J. (2019). "A comprehensive review on reasons for tailings dam failures based on case history." *Advances in Civil Engineering*, *2019*.

Manandhar, S., Kim, S. N., Ha, J. G., Ko, K. W., Lee, M. G., and Kim, D. S. (2021). "Liquefaction Evaluation Using Frequency Characteristics of Acceleration Records in KAIST Centrifuge Tests for LEAP." *Soil Dynamics and Earthquake Engineering*, Elsevier Ltd, 140(December 2019), 106332.

Martin, G. R., Seed, H. B., & Finn, W. L. (1978). "Effects of system compliance on liquefaction tests." *Journal of the geotechnical engineering division*, *104*(4), 463-479.

Menq, F. Y. (2003). "Dynamic properties of sandy and gravelly soils." *The University of Texas at Austin.*

Muszynski, M. R., & S. J. Vitton. (2012). "Particle shape estimates of uniform sands: visual and automated methods comparison." *J. Mater. Civ. Eng.* 24(2), 194-206.

Newland, P. L., and Allely, B. H. (1957). "Volume changes in drained triaxial tests on granular materials." *Geotechnique, London, UK*, 7, 17-34.

Ni, M., T. Abdoun, R. Dobry, K. Zehtab, A. Marr, & W. El-Sekelly. (2020). "Pore pressure and K_σ evaluation at high overburden pressure under field drainage conditions. I: Centrifuge experiments." *J. Geotech. Geoenviron. Eng.* 146(9), 04020088.

Nicholson, P. G., Seed, R. B., & Anwar, H. A. (1993). "Elimination of membrane compliance in undrained triaxial testing. I. Measurement and evaluation." *Canadian Geotechnical Journal*, *30*(5), 727-738.

Okamura, M., & Soga, Y. (2006). "Effects of pore fluid compressibility on liquefaction resistance of partially saturated sand." *Soils and Foundations*, *46*(5), 695-700.

Okamura, M., Nelson, F., and Watanabe, S. (2019). "Pre-Shaking Effects on Volumetric Strain and Cyclic Strength of Sand and Comparison to Unsaturated Soils." *Soil Dynamics and Earthquake Engineering*, Elsevier Ltd, 124, 307–316.

Park, T. K., & Silver, M. L. (1975). "Dynamic triaxial and simple shear behavior of sand." *Journal of the Geotechnical Engineering Division*, *101*(6), 513-529.

Pitilakis, K., Gazepis, C., & Anastasiadis, A. (2004). “Design response spectra and soil classification for seismic code provisions.” *In World Conference on Earthquake Engineering, Vancouver.*

Porcino, D., Caridi, G., & Ghionna, V. N. (2008). “Undrained monotonic and cyclic simple shear behavior of carbonate sand.” *Geotechnique,* 58(8), 635–644.

Psarropoulos, P. N., & Tsompanakis, Y. (2008). “Stability of tailings dams under static and seismic loading.” *Canadian Geotechnical Journal*, *45*(5), 663-675.

Pyke R. (1979). "Nonlinear soil models for irregular cyclic loadings." J. *Geotech.Engrg. Div., ASCE,* 105(6), 715-726.

Pyke, R. (1978). “Some effects of test configuration on measured soil properties under cyclic loading.” *Geotechnical Testing Journal, 1*(3), 125-133.

Ramana, K. V., & Raju, V. S. (1982). “Membrane penetration in triaxial tests.” *Journal of the Geotechnical Engineering Division, 108*(2), 305-310.

Rashidan M., Ishihara K., Kokusho T., Kanatani M, & Okamoto T. (1995). “Undrained Shearing Behavior of Very Loose Gravelly Soils.” *Static and Dynamic, Properties of Gravelly Soils (GSP 56), ASCE, New York/NY*, 77-91.

Rico M., Benito G., & Diez-Herrero A. (2008). “Floods from tailings dam failures.” *Journal of hazardous materials* 154(1-3), 79-87.

Rinehart R., Brusak A., & Potter. N. (2016). “Liquefaction triggering assessment of gravelly soils: State-of-the-Art Review.” *Washington, DC: US Bureau of Reclamation. Rep.* ST-2016-0712-01.

Ruttithivaphanich P., & I. Sasanakul. (2022). “Liquefaction Evaluation of a Gravel-Sand Mixture Using Centrifuge Tests.” *In Geo-Congress 2022* 288-296.

Ruttithivaphanich, P., & Sasanakul, I. (2019). “Frequency Effects on Low-Strain Shear Modulus and Damping for Natural Clays and Silts.” In *Geo-Congress 2019: Geotechnical Materials, Modeling, and Testing* (pp. 590-598). Reston, VA: American Society of Civil Engineers.

Santamarina, J. C., & Goodings, D. J. (1989). “Centrifuge modeling: A study of similarity.” *Geotechnical Testing Journal*, *12*(2), 163-166.

Sasanakul, I, P. Ruttithivaphanich, & S. Dejphumee. (2022). “Dynamic Characterization of Mine Waste Rock in Centrifuge Testing.” *In 10th International Conference on Physical Modelling in Geotechnics, KAIST, Daejeon, Korea*

Seed, H. B. (1983). “Special lecture: Evaluation of the dynamic characteristics of sands by in-situ testing techniques.” *Revue française de géotechnique,* (23), 91-99.

Seed, H. B., & Lee, K. L. (1966). “Liquefaction of saturated sands during cyclic loading.” *Journal of the Soil Mechanics and Foundations Division, 92*(6), 105-134.

Seed, H. B., & Peacock, W. H. (1971). "Test procedures for measuring soil liquefaction characteristics." *Journal of the Soil Mechanics and Foundations Division*, *97*(8), 1099-1119.

Seed, H. B., Wong, R. T., Idriss, I. M., & Tokimatsu, K. (1986). "Moduli and Damping Factors for Dynamic Analyses of Cohesionless Soils." *Journal of Geotechnical Engineering,* 112(11), 1016-1032.

Seed, R. B., & Harder, L. F. (1990). "SPT-based analysis of cyclic pore pressure generation and undrained residual strength." *Proc. H. B. Seed Memorial Symp., BiTech Publishing, Vancouver, British Columbia, Canada,* 2, 351-376

Seyed Ghafouri, S. M. H. (2018). "Effect of Initial Static Shear Stress on Undrained Cyclic Resistance of Well Graded, Medium Dense Gravelly Soils by Cyclic Triaxial Tests." *MSc Thesis*.

Sivathayalan, S. (1994). "Static, cyclic and post liquefaction simple shear response of sands." Ph.D. thesis, Univ. of British Columbia, Vancouver, BC, Canada, 154.

Sivathayalan, S. (2000). "Fabric, initial state and stress path effects on liquefaction susceptibility of sands." *Doctoral dissertation, University of British Columbia.*

Sivathayalan, S., & Yazdi, A. M. (2014). "Influence of strain history on postliquefaction deformation characteristics of sands." *Journal of Geotechnical and Geoenvironmental Engineering*, *140*(3), 04013019.

Stewart, D. P., Chen, Y. R., & Kutter, B. L. (1998). "Experience with the use of methylcellulose as a viscous pore fluid in centrifuge models." *Geotechnical Testing Journal*, *21*(4), 365-369.

Stokoe K.H., Rix G.J., & Nazarian S. (1989) "In situ seismic testing with surface waves." *In International Conference on Soil Mechanics and Foundation Engineering,* 12th, 1989, Rio de Janiero, Brazil. Vol. 1.

Stokoe, K. H., Darendeli, M. B., Andrus, R. D., & Brown, L. T. (1999, December). "Dynamic soil properties: laboratory, field and correlation studies." In *Proceednings of the 2nd international conference on earthquake geotechnical engineering,* 811-845.

Stokoe, K. H., Hwang, S. K., Lee, J. K., & Andrus, R. D. (1995). "Effects of various parameters on the stiffness and damping of soils at small to medium strains." *Proceedings of the International Symposium,* 12-14.

Stokoe, K. H., Roesset J. M., Bierschwale J. G., & Aouad. M. (1988). "Liquefaction potential of sands from shear wave velocity." *In Proceedings, 9th World Conference on Earthquake* (13), 213-218.

Sun, Y. J., Zhang, D., Shi, B., Tong, H. J., Wei, G. Q., & Wang, X. (2014). "Distributed acquisition, characterization and process analysis of multi-field information in slopes." *Engineering geology*, *182*, 49-62.

Sybico Jr., J. A. (1992). Post-liquefaction settlement of sands, MSc Thesis, Univ. of Calif., Davis, Calif.

Taylor RN (2003) "Geotechnical centrifuge technology." *Blackie Academic, London*

Taylor, R. N. (Ed.) (2018). "Geotechnical centrifuge technology." *CRC Press.*

Teymur, B., & Madabhushi, S. G. (2002). Shear stress-strain analysis of sand in ESB model container by harmonic wavelet analysis. In *Physical modelling in geotechnics: ICPMG'02* (pp. 201-206).

Thygesen, K. S. (2017). "Calculating excitons, plasmons, and quasiparticles in 2D materials and van der Waals heterostructures." *2D Materials, 4*(2), 022004.

Tobita T, Ashino T, Ren J, & Iai S. (2018) "Kyoto University LEAP-GWU-2015 tests and the importance of curving the ground surface in centrifuge modelling." *Soil Dynam Earthq Eng*., 11, 650–62.

Tokimatsu, K. (1990). "System compliance correction from pore pressure response in undrained cyclic triaxial tests." *Soils and Foundations, 30*(2), 14-22.

Towhata, I., Pradel, D. E., & Ishihara, K. (1988). "Plasticity Approach to Sand Behaviour under Principal Stress Axes Rotation." In *Studies in Applied Mechanics* (Vol. 20, pp. 191-200). Elsevier.

Vaid, Y. P., & Sivathayalan, S. (1996). "Static and cyclic liquefaction potential of Fraser Delta sand in simple shear and triaxial tests." *Canadian Geotechnical Journal, 33*(2), 281-289.

Vallejo, L.E., & Mawby, R., (2000). "Porosity influence on the shear strength of granular material–clay mixtures." Engineering Geology 58, 125 – 136

Vucetic, M., & Dobry, R. (1988). "Degradation of marine clays under cyclic loading." *Journal of Geotechnical Engineering, 114*(2), 133-149.

Wei, Y. C., Lee C. J., Hung W. Y., & Chen. H. T. (2010). "Application of Hilbert-Huang transform to characterize soil liquefaction and quay wall seismic responses modeled in centrifuge shaking-table tests." *Soil Dyn. Earthquake Eng.* 30 (7), 614–629.

Wickland, B. E., Wilson, G. W., Wijewickreme, D., & Klein, B. (2006). "Design and evaluation of mixtures of mine waste rock and tailings." *Canadian Geotechnical Journal, 43*(9), 928-945.

Wu J., Kammerer A.M., Riemer M.F., Seed R.B., & Pestana, J.M. (2004). "Laboratory study of liquefaction triggering criteria." In *13th World conference on earthquake engineering, Vancouver, BC, Canada, Paper* (No. 2580).

Wu, J. T. (2018). "A generic design protocol for geosynthetic reinforced soil foundation." *Transportation Infrastructure Geotechnology, 5*(4), 303-317.

Xu, D. S., Liu, H. B., Rui, R., & Gao, Y. (2019). "Cyclic and postcyclic simple shear behavior of binary sand-gravel mixtures with various gravel contents." *Soil Dynamics and Earthquake Engineering, 123*, 230-241.

Yamamuro, J. A., & Covert, K. M. (2001). "Monotonic and cyclic liquefaction of very loose sands with high silt content." *Journal of geotechnical and geoenvironmental engineering*, *127*(4), 314-324.

Yan, L., & K. Lum. (2003). "Liquefaction assessment of gravely soils for dam safety evaluation." *In ICOLD Congress, Montreal.*

Yang, Z. X., & Pan, K. (2017). "Flow deformation and cyclic resistance of saturated loose sand considering initial static shear effect." *Soil Dynamics and Earthquake Engineering*, 92, 68-78.

Yasuda, N., & Matsumoto, N. (1994). "Comparisons of deformation characteristics of rockfill materials using monotonic and cyclic loading laboratory tests and in situ tests." *Canadian geotechnical journal*, *31*(2), 162-174.

Ye, G. L., Lin, N., Bao, X. H., Gu, L., & Yadav, S. K. (2018). "Effect of Quaternary transgression and regression on the engineering properties of Shanghai soft clays." *Engineering Geology*, *239*, 321-329.

Yi F. (2010). "Procedure to evaluate seismic settlement in dry sand based on shear wave velocity." *The 9th US national and 10th Canadian Conference on Earthquake Engineering (9US/10CCEE), Toronto, Canada.*

Yoshimine M., Nishizaki H., Amano K., & Hosono Y. (2006). "Flow deformation of liquefied sand under constant shear load and its application to analysis of flow slide of infinite slope." *Soil Dynamics and Earthquake Engineering*, 26(2-4), 253-264.

Youd, T.L., Idriss, I.M., Andrus, Ronald D., Arango, Ignacio, Castro, Gonzalo, Christian, John T., Dobry, Ricardo, Liam Finn, W.D., Harder, Leslie F., Hynes Jr, Mary Ellen, Ishihara, Kenji, Koester, Joseph P., Liao, Sam S.C., Marcuson III, William F., Martin, Geoffrey R., Mitchell, James K., Moriwaki, Yoshiharu, Power, Maurice S., Robertson, Peter K., Seed, Raymond B., Stokoe II, & Kenneth H., (2001). "Liquefaction resistance of soils summary report from 1996 NCEER and 1998 NCEER/NSF workshops on Evaluation of Liquefaction Resistance of Soil." *Journal of Geotechnical and Geoenvironmental Engineering*, ASCE 127, 817–833.

Zeghal, M., & Elgamal, A. W. (1994). "Analysis of Site Liquefaction Using Earthquake Records." *Journal of Geotechnical Engineering*, 120(6), 996–1017.

Zeghal, M., Elgamal A. W., Tang H. T., & Stepp. J. C. (1995). "Lotung downhole array. II: Evaluation of soil nonlinear properties." *J. Geotech. Eng.* 121 (4), 363–378.

Zeghal, M., Elgamal, A. W., & Parra, E. (1996). "Identification and modeling of earthquake ground response—II. Site liquefaction." *Soil Dynamics and Earthquake Engineering*, *15*(8), 523-547.

Zeghal, M., Elgamal, A. W., Zeng, X., & Arulmoli, K. (1999). "Mechanism of Liquefaction Response in Sand-Silt Dynamic Centrifuge Tests." *Soil Dynamics and Earthquake Engineering*, 18(1), 71–85.

Zekkos, D., Manousakis, J., Greenwood, W., & Lynch, J. (2016). "Immediate uav-enabled infrastructure reconnaissance following recent natural disasters: case histories from greece." In *International conference on natural hazards and infrastructure*.

Zhang, J., Andrus, R. D., & Juang, C. H. (2005). "Normalized shear modulus and material damping ratio relationships." *Journal of Geotechnical and Geoenvironmental Engineering, 131*(4), 453-464.

Zhou, Y. G., Sun, Z. B., & Chen, Y. M. (2018). "Zhejiang University benchmark centrifuge test for LEAP-GWU-2015 and liquefaction responses of a sloping ground." *Soil Dynamics and Earthquake Engineering, 113*, 698-713.

Zorapapel, G. B. T., & Vucetic, M. (1994). "The effects of seismic pore water pressure on ground surface motion." *Earthquake Spectra, 10*(2), 403-438.